8-1-1989

Basic Studies of III-V High Efficiency Cell Components

M. S. Lundstrom
Purdue University

M. R. Melloch
Purdue University

R. F. Pierret
Purdue University

M. S. Carpenter
Purdue University

Basic Studies of III-V High Efficiency Cell Components

M.S. Lundstrom, M.R. Melloch,
R.F. Pierret, M.S. Carpenter,
H.L. Chuang, A. Keshavarzi,
M.E. Klausmeier-Brown, G.B.Lush,
T.B. Stellwag

TR-EE 89-39
August 1989

School of Electrical Engineering
Purdue University
West Lafayette, Indiana 47907

BASIC STUDIES

of

III-V HIGH EFFICIENCY CELL COMPONENTS

M.S. Lundstrom, M.R. Melloch, R.F. Pierret,

M.S. Carpenter, H.L. Chuang, A. Keshavarzi,

M.E. Klausmeier-Brown, G.B. Lush, and T.B. Stellwag

School of Electrical Engineering
Technical Report TR-EE 89-39
Purdue University
West Lafayette, Indiana 47907

Annual Progress Report: 8/15/88 - 8/14/89
Subcontract: XL-5-05018-1

NOTICE

PREFACE

This project's objective is to improve our fundamental understanding of the generation, recombination, and transport of carriers within III-V homo- and heterostructures. The research consists of fabricating and characterizing solar cell "building blocks" such as junctions and heterojunctions as well as basic measurements of material parameters. A significant effort is also being directed at characterizing loss mechanisms in high-quality, III-V solar cells fabricated in industrial research laboratories throughout the United States. The project's goal is to use our understanding of the device physics of high-efficiency cell components to maximize cell efficiency. A related goal is the demonstration of new cell structures fabricated by molecular beam epitaxy (MBE). The development of measurement techniques and characterization methodologies is also a project objective. We expect that the insight into III-V device physics occurring during the course of this work will help to identify paths towards higher efficiency III-V cells.

This report describes our progress during the fourth year of the project. The past year's efforts centered on completing studies of heavy doping effects in p^+-GaAs and assessing the importance of similar effects in n^+-GaAs, and at continuing research on characterizing, controlling, and passivating perimeter recombination currents. We also initiated work to identify the dominant loss mechanisms in $Al_{0.2}Ga_{0.8}As$ solar cells and brought on-line a new MBE growth facility and demonstrated the high-quality of the films by fabricating, with assistance from Spire Corporation, 23.8% 1-sun solar cells.

Our work has benefited greatly from interactions with industrial researchers. We owe special thanks to Steve Tobin, Stan Vernon, and their colleagues at Spire Corporation for providing $Al_{0.2}Ga_{0.8}As$ films and cells for our basic studies and for fabricating high-efficiency cells from our MBE-grown films. The work described in this report was supported by the Solar Energy Research Institute. Cecile Lebouef and John Benner of SERI have provided the long term guidance and encouragement that has made this work possible. Our research also benefited by collaborations with two graduate student researchers not supported by SERI. H.L Chuang was supported by the Indiana Corporation for Science and and Technology and M.E. Klausmeier-Brown by a fellowship from the Eastman Kodak Company.

SUMMARY

Project Overview

Motivation

The efficiencies of both single and multiple junction III-V solar cells continue to increase rapidly, and, although much of the progress now occurring is due to improving material quality, it is becoming increasingly important to carefully examine the internal device physics of solar cells so that cell designs can be tailored to the material constraints. The need for a sound understanding of internal device physics is clearly illustrated by Stanford University's research on point contact silicon cells in which a new design approach, specifically tailored to the dominant loss mechanisms in crystalline silicon cells, led to a marked increase in cell efficiency. Although there is no assurance that the point contact design would similarly benefit III-V cells, the example does illustrate the benefits of careful cell design guided by detailed knowledge of device physics. Our research consists of basic studies directed at expanding the device physics knowledge base for III-V solar cells and of applying this evolving knowledge in order to explore new approaches for enhancing solar cell efficiency. While these basic studies are contributing to the steady progress of III-V cell efficiencies, they may at the same time lead to innovative new approaches for achieving substantial efficiency gains.

Project Objectives

Our research is *device-directed*; it begins by characterizing state-of-the-art, high-efficiency solar cells and quantifying their internal loss mechanisms. One project objective, therefore, is the development of characterization techniques and methodologies for identifying and analyzing specific loss mechanisms in modern, crystalline solar cells. Based on the cell characterization results, specific research objectives are then prioritized. During previous years, we focused on crystalline GaAs cells; this year's work marks a transition from GaAs to $Al_xGa_{1-x}As$. The ternary, $Al_xGa_{1-x}As$, was selected not because we are convinced that it is the optimum photovoltaic material but, rather, because it serves as a good model III-V semiconductor in which to explore the inter-relationships of material quality, device physics, and device design. At the $x = 0$ compositional point, the material is GaAs, which is becoming a very well-understood, well-characterized semiconductor. As the Al mole fraction increases, the material properties, device physics, and design issues, change profoundly. Basic studies on this material system should provide device characterization, analysis, and design approaches that are applicable to all crystalline III-V solar cells.

The general objectives of the project can be broadly stated as

- To examine the device physics of minority carrier injection, transport, and recombination in III-V solar cells
- To identify and quantify loss mechanisms in state-of-the-art, high-efficiency, III-V, crystalline solar cells
- To develop new techniques and approaches for characterizing solar cells and for measuring basic parameters
- To explore new approaches for enhancing III-V solar cell efficiency

For the past year, our specific project objectives have been:

- Heavy doping studies in p^+ and n^+ GaAs
- Studies of surface and perimeter recombination
- Loss analysis of MOCVD- and MBE-grown $Al_{0.2}Ga_{0.8}As$ solar cells
- Turn-on and characterization of a Varian GEN II MBE system and demonstration of photovoltaic quality GaAs.

The heavy doping work continued our group's previous work on examining the band structure modifications associated with heavy impurity doping and at examining the implications of such effects on solar cell performance. Our group's previous work has also established the importance of perimeter recombination currents — even in quite large ($\simeq 2\,cm \times 2\,cm$) cells. The surface and perimeter recombination studies consist of developing techniques for characterizing perimeter recombination, studies to relate perimeter recombination to the conditions of the GaAs surface, and exploration of techniques for passivating the surface and perimeter by chemical treatments. The loss analysis of $Al_{0.2}Ga_{0.8}As$ cells is directed at establishing the dominant loss mechanisms in this material in order to prioritize future research. Since our research makes use of MBE-grown films, it is also important to relate these studies to the more widely-used MOCVD-grown films. Finally, because an important objective of ours is to explore new approaches, it was necessary to establish an improved MBE growth facility and to establish the films it produced were of photovoltaic quality.

Relation to DOE Mission

One component of the national photovoltaic program is directed at developing concentrator photovoltaic systems based on high-efficiency, crystalline solar cells. It is generally felt that efficiencies must exceed 35% in the long term if this approach is to become economically viable. The III-V semiconductors are particularly interesting for such applications. GaAs, for example is a relatively mature photovoltaic material that seems certain to produce solar cells exceeding 30% efficiency. Various III-V heterostructure combinations make possible multiple junction solar cells with the potential for achieving conversion efficiencies well above 35%. Although the number of III-V semiconductors under investigation is quite large, our work, which focuses on the technologically important GaAs/AlGaAs system, should be broadly applicable. By centering our work on a relatively mature (in comparison with other III-V's, that is) material system, we ensure that we are dealing with basic physical effects central to III-V cell design — not with the difficult to control material quality issues that arise with immature technologies. Since the various III-V semiconductors have much in common, the basic findings of our work should provide useful guidelines for III-V crystalline research in general.

Relation to Other DOE-Funded Research

Because many of the design issues for III-V cells are similar, this research is broadly applicable to much DOE-funded III-V cell research. At the same time, however, we've developed some specific relationships with other DOE-funded programs. We've been fortunate to collaborate with researchers at Spire Corporation on GaAs, and more recently on AlGaAs, solar cells. This collaboration has included work on heteroface recombination, heavy doping effects, perimeter recombination, and on heterojunction back surface fields. The work has served to ensure that our efforts were directed at issues of general concern and not on issues specific to our MBE-grown material. It has at the same time provided useful basic information that assisted Spire's continuing success in increasing GaAs cell efficiencies and has resulted in a number of joint publications.

A more recent relationship has developed with Dr. Richard Arhenkiel and his laboratory at SERI. This work centers on using Dr. Ahrenkiel's time-of-flight (TOF) measurement to characterize minority carrier mobilities in GaAs. Because the electron mobility in GaAs is so high, the electrical response is rapid. The microwave techniques we're employing to package our solar cell test structures, should significantly extend the range of the TOF measurement. There has also been a relatively recent appreciation of the role of so-called photon recycling effects in these measurements. A detailed computer simulation of the coupled, minority carrier - photon diffusion process will enable us to quantitatively assess the effects of photon recycling on the TOF measurement for the first time.

Project History

Initial work on this project, which began in 1985, was directed at the general objectives as stated above. The first year's efforts were largely directed at establishing an MBE film growth facility and on developing procedures for electrically characterizing solar cells and test structures. Our first MBE growth facility employed a first-generation Perkin-Elmer machine, but films are now grown with a Varian GEN II system.

Beginning at the second year, our efforts have centered on conducting basic studies. The second year's efforts were directed at identifying loss mechanisms in high-quality GaAs cells supplied by Spire Corporation. This work identifyed a need for improving the heteroface recombination velocity. (Subsequent work by Spire researchers has produced high-quality interfaces with correspondingly high ($\simeq$ 100%) internal quantum efficiencies.) During the second year, we also conducted an experiment, using our own MBE-grown films, which established the importance of heavy doping effects on GaAs solar cells, and we also demonstrated that a heterojunction back-surface-field could, apparently by gettering impurities, provide benefits quite distinct from their minority carrier confining properties. Heterojunction back-surface-fields have subsequently become a standard feature in the Spire cell design. Finally, application of current DLTS for characterizing large area solar cells was also demonstrated during the second year of the project.

The third year's work centered on detailed characterization of electron injection in p^+-GaAs using MOCVD-grown films supplied by Spire Corporation. Though limited to doping densities below 10^{19} cm^{-3}, the work demonstrated for the first time that heavy doping effects have important consequences for GaAs solar cells. The role of perimeter recombination on solar cell performance was also addressed during the third year, and a new chemical treatment for passivating surfaces was devised and demonstrated.

The fourth year's work extends, and in some cases completes, work initiated in earlier years and initiates new research directed at $Al_xGa_{1-x}As$. The fourth year's activities are the subject of this report and are surveyed below.

Scientific and Technical Activities: 1988 - 1989

During the past year, our activities have focused on: 1) completing work on heavy doping effects in p^+-GaAs, 2) assessing the importance of analogous effects in n^+-GaAs, 3) continuing efforts to characterize and control perimeter recombination, 4) work to understand and further develop chemical passivation treatments, 5) conducting a baseline study of loss mechanisms in $Al_{0.2}Ga_{0.8}As$ solar cells, and 6) bringing on-line a new MBE growth facility. Work on these tasks is described in this report and in the reprints appended to it. Key results include: 1) extension of bandgap narrowing measurements in p^+-GaAs to one order of magnitude higher in doping, 2) demonstration that effective bandgap shrinkage is not an important factor in n^+-GaAs, 3) observation of an orientation-dependence to perimeter recombination, 4) demonstration that

losses in both MOCVD- and MBE-grown $Al_{0.2}Ga_{0.8}As$ appear to be dominated by similar defects, and 5) successful turn-on and operation of a new MBE growth facility and the subsequent demonstration of GaAs solar cells with 23.8% conversion efficiency under 1-sun, AM1.5 global operating conditions.

Overview of the Report

Many of last year's research activities are described in the various chapters of this report; others are described in the reprints included in the Appendix. The report begins with two chapters describing recent work on bandgap narrowing in p^+-GaAs. An experimental technique, based on using a homojunction bipolar transistor, was developed to measure the product, $n_{ie}^2 D_n$ in very heavily doped GaAs. The experimental technique is described in **Chapter 1**, and the results are presented and discussed in **Chapter 2**. (Papers based on Chapters 1 and 2 have been submitted for publication.) Although our understanding of the electronic properties of heavily doped GaAs is far from complete, it now seems sufficient for solar cell design. Our future work in this area will focus on basic physical mechanisms and on the implications for AlGaAs/GaAs bipolar transistors. This work will continue to benefit the solar cell community but will be supported by the National Science Foundation.

Gallium arsenide films now being grown in our Varian GEN II MBE are quite comparable in quality to high-quality, MOCVD-grown GaAs. In **Chapter 3**, we describe our experimental work, conducted in collaboration with Spire Corporation, to compare high-quality MOCVD- and MBE-grown films for photovoltaic applications. A paper based on the results in Chapter 3 has been written and submitted for publication.

Chapter 4 describes our first work to examine loss mechanisms in $Al_{0.2}Ga_{0.8}As$ solar cells; it compares an MOCVD-grown film with an MBE film targeted to be identical. The work is motivated by the possible use of AlGaAs for top cell applications in multi-junction cells and because AlGaAs will serve as a model semiconductor for future basic studies of III-V cells. This chapter is a written version of a poster presented at the 9th Photovoltaic Advanced Research and Development Review Meeting in Golden in May of 1989. A shorter version of Chapter 4, without some of the figures and the discussion on oval defects, has been submitted to *Solar Cells*.

Some of the variations in III-V solar cell performance that occur as cells age is a result of the aging perimeters and their associated recombination losses. Previous work by our group has demonstrated that perimeter recombination has a significant influence on the one-sun performance of GaAs cells and that it is often the dominant effect in small area diodes utilized for diagnostics. In **Chapter 5**, we describe a recent experiment in which a strong orientation dependence to perimeter recombination was noted. Perimeter recombination is especially important for relatively small area test devices commonly used for diagnostics or for solar cell development. The strong variation in results that occurs as the orientation varies, must be accounted for in order to properly interpret experiments.

The oxides that form on bare GaAs surfaces produce large surface state densities that often dominate the electrical performance of devices. Recent work by our group and others has demonstrated that sulfide chemical treatments can reduce recombination losses in solar cells, increase the gain of bipolar transistors, and modify the barrier height of metal-GaAs contacts. It is therefore, of great technical importance to determine the exact nature of the sulfide-treated GaAs surface. **Chapter 6** presents a detailed XPS study of ammonium sulfide treated GaAs surfaces and demonstrates that the treatment removes surface oxides and leaves behind less than one monolayer of sulfer which inhibits further oxidation. This chapter is a written version of a poster presented at the 16th Conference on Physics and Chemistry of Semiconductor Interfaces and has

been accepted in paper form for publication in the *Journal of Vacuum Science and Technology B*.

The report also contains two appendices. **Appendix 1** contains a list of several papers that were published during 1988-1989, and **Appendix 2** is a complete list of the publications that have resulted during the course of the project.

Conclusions

When we began these basic studies three years ago, we viewed GaAs as a poorly characterized semiconductor when compared with Si. We now understand much more about the fundamental device physics of GaAs and the importance of various loss mechanisms in state-of-the-art cells. With this knowledge, it should now be possible to critically assess, with a high degree of confidence, the potential for innovative GaAs-based solar cell designs. The general features of these results should also apply to other III-V semiconductors. For example conversations with C. Gordia and A. Rohatgi indicate effective bandgap shrinkage effects similar to those we observed in p^+-GaAs appear to be degrading the performance of InP solar cells. The work described in this report marks a transition in two different respects. First, our emphasis is shifting to $Al_xGa_{1-x}As$, which should serve as a model for the material parameter and device physics issues faced by III-V cells in general. Second, with our new MBE growth facility and the high-quality films now being produced, we plan to place more emphasis on the demonstration of innovative concepts for enhancing the efficiency of III-V solar cells.

TABLE OF CONTENTS

CHAPTER 1

HEAVY DOPING EFFECTS IN p^+GaAs: Experimental Technique

1.1 INTRODUCTION

Changes in the energy band structure associated with heavy impurity doping profoundly influence both the gain of Si bipolar transistors and the efficiency of Si solar cells [1]. Optical properties of GaAs are also strongly affected by heavy doping [2], but the effects on the electrical operation of devices have only recently been addressed. In a previous paper we presented an analysis of electron injection currents in p^+-n GaAs diodes, and found heavy doping effects in p^+-GaAs much like to those observed in p^+-Si [3]. Those diode-based measurements were the first attempt to explore the implications of heavy doping for the electrical performance of GaAs devices, but the need to separate the electron and hole injection components of the diode current limited the technique to p-type doping $\leq 10^{19}$ cm^{-3}. In this chapter we report new results concerning heavy doping effects in p^+-GaAs based on measurements of the collector current versus base-emitter voltage (I_C–V_{BE}) characteristics of n-p^+-n GaAs homojunction transistors. Such transistor-based measurements yield a natural separation of electron and hole currents, so electron injection currents can be characterized in p^+-GaAs doped much greater than 10^{19} cm^{-3}.

In heavily doped Si and GaAs, carrier-carrier and carrier-dopant interactions reduce the bandgap, and distort the densities-of-states by introducing band tails [4,5]. Detailed calculations [5] have shown that this perturbation of the band structure causes the $n_o p_o$ product in heavily doped p-type GaAs to be greater than its value in lightly doped material. For p-type dopant concentrations in the range 10^{18} to 10^{19} cm^{-3}, diode-based measurements confirm that $n_o p_o > n_{io}^2$, and that the $n_o p_o$ product increases with doping [3]. For electrical devices with heavily doped p-layers (e.g. bipolar transistors) the most important effect of energy band structure distortion is this strong enhancement of the $n_o p_o$ product. In heavily doped p-type GaAs,

$$n_{ie}^2 \equiv n_o p_o > n_{io}^2 . \tag{1.1}$$

where n_{ie} is the effective intrinsic carrier concentration and n_{io} is the value of the $n_o p_o$ product in lightly doped material.

We have previously reported measurements of electron injection currents in p^+-n GaAs diodes. Those diodes were designed with the unpassivated p-layer thickness W_p much less than the electron diffusion length, so that the electron component of current (J_n) was much greater than the hole component [6]. Under such conditions, the current component associated with electron injection into the p-layer is given by

$$J_n = q \frac{(n_{ie}^2 D_n)}{N_A W_p} (e^{qV/k_B T} - 1). \tag{1.2}$$

Using a generalization of (1.2), it was possible to extract the quantity $(n_{ie}^2 D_n)$ without knowledge of the surface recombination velocity by varying the thickness of the p-layer, W_p, by etching. (Unfortunately, it is not possible to separate n_{ie}^2 from the minority carrier diffusion coefficient, D_n, using steady-state current measurements.) Figure 1.1 shows a comparison of the measured $(n_{ie}^2 D_n)$ values with the curve expected assuming that heavy doping does not perturb the band structure. The solid curve was constructed assuming parabolic bands, and the reduction of the $n_o p_o$ product at high dopant densities due to majority carrier degeneracy was accounted for [7]; minority carrier mobilities predicted by Walukiewicz et al. for uncompensated material were assumed [8], with mobility related to diffusion coefficient by $k_B T \mu_n = q D_n$. The difference in the measured $(n_{ie}^2 D_n)$ values and those computed assuming unperturbed energy bands is an order of magnitude at 10^{19} cm^{-3}.

In order to reduce the sheet resistance in the base layer of AlGaAs/GaAs N-p$^+$-n HBTs, recent work has emphasized very heavy base doping, $\geq 10^{20}$ cm^{-3} [9]. A diode-based technique [6] is inadequate for measuring $(n_{ie}^2 D_n)$ at such high p-type doping levels because the electron and hole current components become similar in magnitude. In contrast, transistor-based current measurements allow a natural separation of hole and electron components.

1.2 EXPERIMENT

The collector current versus base-emitter voltage (I_C–V_{BE}) characteristic of a bipolar transistor is described by an equation similar to (1.2), which may be expressed for moderate values of V_{BE} as [10]

$$\ln I_C = \ln \left[\frac{q A_E (n_{ie}^2 D_n)}{N_A W_B} \right] + \frac{q V_{BE}}{k_B T}, \tag{1.3}$$

where A_E is the emitter area and W_B is the base thickness. Note that both (1.2) and (1.3) assume a flat p-type dopant profile. The quantity $(n_{ie}^2 D_n)$ is determined from the intercept of the linear portion of a plot of $\ln I_C$ versus V_{BE}; the device temperature can also be found very accurately from the slope of the line [1]. To ensure the validity of (1.3), we require that the base thickness be negligible compared to a minority carrier diffusion length:

$$L_n^2 = D_n \tau_n >> W_B^2, \tag{1.4}$$

where L_n is the electron diffusion length and τ_n is the electron lifetime.

Homojunction transistors, consisting only of GaAs layers, were chosen for this experiment in lieu of the more common AlGaAs/GaAs HBT configuration. Improper grading of the aluminum

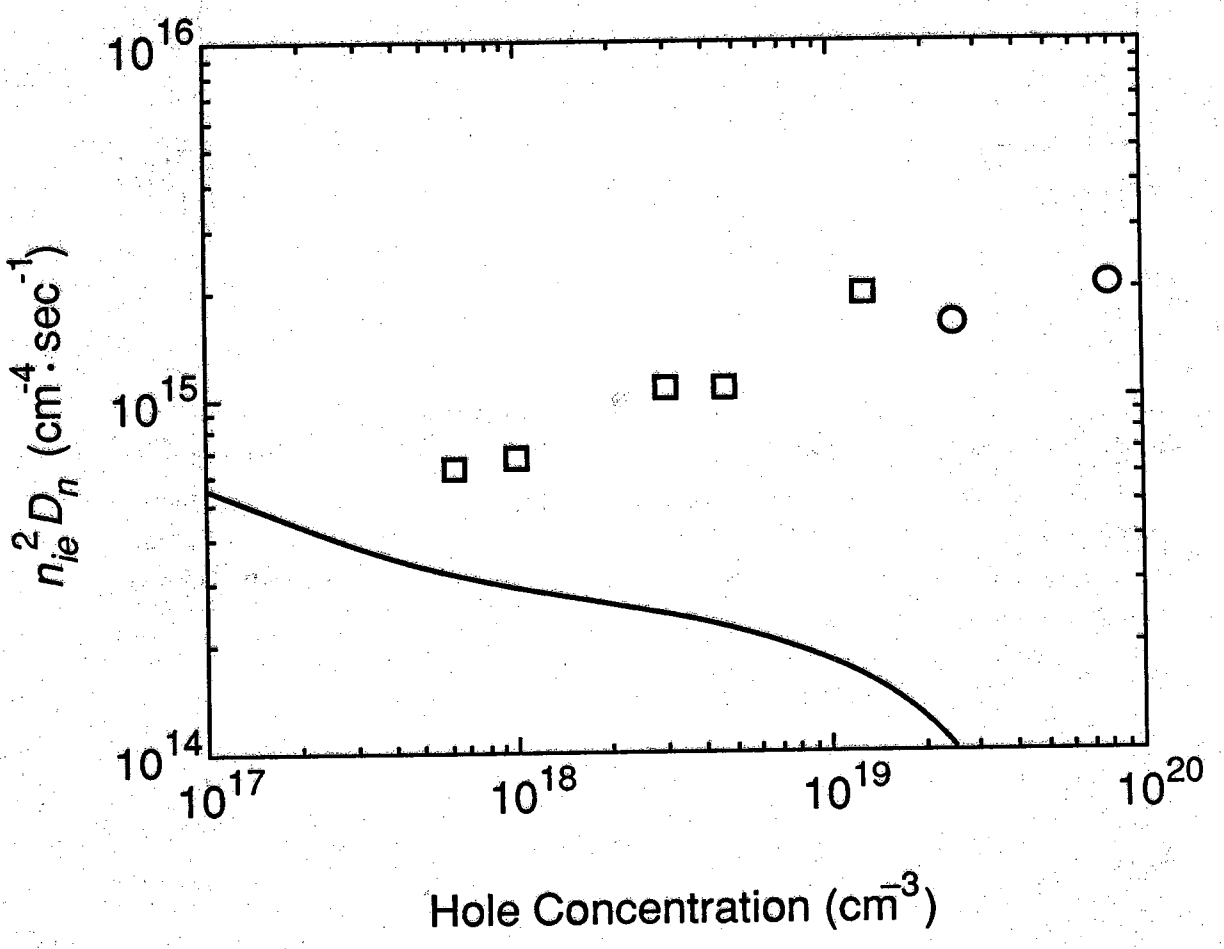

Fig. 1.1 The quantity ($n_{ie}^2 D_n$) versus carrier concentration in p-type GaAs at T = 300 K. The squares represent values measured using Zn-doped, MOCVD-grown diodes; the measurements employing Be-doped, MBE-grown homojunction bipolar transistor are represented by the circles.

composition in the emitter of an HBT, or misalignment of the compositional and doping junctions could result in a conduction band energy barrier at the emitter-base junction, which would invalidate (1.3). However, the (I_C–V_{BE}) characteristics of homojunction bipolar transistors should always be well-described by (1.3).

The epitaxial films required for this study were grown in a Varian GEN-II molecular beam epitaxy (MBE) system on n^+-GaAs substrates. The substrates were mounted in In, and were rotated at 5 rpm during the growth. The growth rate was 1 μm/hr at a substrate temperature of 600°C (the oxide desorption temperature was 580°C.) The As_4 to Ga beam equivalent pressure was 20, as determined by an ion gauge placed in the substrate growth position. Film thickness was monitored by counting oscillations in the reflection high-energy electron diffraction (RHEED) pattern at the beginning of film growth. The n-type dopant was Si, and the p-type dopant was Be. The slope of a plot of carrier concentration in the p-type material versus Be oven temperature was found to be consistent with the vapor pressure curve of Be in the concentration range 2×10^{18} to 8×10^{19} cm^{-3}, implying the absence of significant precipitation of Be even at the highest doping level [11, 12].

Standard optical lithography and wet-etching techniques were employed in device fabrication. The emitter contacts were Ge:Au:Ni/Ti/Au, alloyed at 320°C for 60 seconds; the base contacts were non-alloyed Ti/Au. Indium was used to mount the substrates in the MBE system during growth, and proved to be an effective means of contacting the collector layer (through the substrate). The mask set used included transistors of widely varying dimension, test patterns for measuring sheet resistance of the emitter and base layers, and structures for determining hole mobility and concentration in the base by Hall effect.

The dopant concentrations were probed by secondary ion mass spectroscopy (SIMS) at Charles Evans and Associates using 8 keV O_2^+ ion bombardment and positive sputtered ion mass spectrometry. A semi-insulating GaAs wafer, implanted at 150 keV with a 1×10^{15} cm^{-2} dose of Be, served as a calibration standard for the SIMS analysis of Be concentration. Concentration of Si was also monitored in the SIMS analysis. Carrier concentration in the emitter layer was checked by electrochemical capacitance-voltage profiling (ECV) at Solecon Laboratories.

1.3 RESULTS and DISCUSSION

Results for two similar transistor films, with targeted base layer Be concentrations of 8×10^{19} cm^{-3} and 3×10^{19} cm^{-3}, will be presented here. The targeted film parameters are listed in Table 1.1. We first discuss results for the film with the more heavily doped base (8×10^{19} cm^{-3}). The resistivity of the base layer material was found to be 1.4×10^{-3} Ω–cm, as measured both by using the Hall bar pattern, and by a transmission line technique. The hole mobility and concentration were found by Hall effect measurements to be 76 cm^2–V^{-1}–sec^{-1} and 6×10^{19} cm^{-3},

Table 1.1 Layer composition of the MBE-grown, homojunction bipolar transistor films.

Layer Composition	**Function**	**Thickness (nm)**	**Dopant Concentration (cm^{-3})**
n^+-GaAs	Contact Layer	100	$\geq 3\times10^{18}$
n-GaAs	Emitter	100	5×10^{17}
p^+–GaAs	**Base**	**100**	**3×10^{19} 8×10^{19}**
n-GaAs	Collector	$\cong$ 300	2×10^{17}
n^+-GaAs	Sub-Collector	1000	$\geq 10^{18}$
n^+-GaAs	Substrate	···	$\geq 10^{18}$

respectively, assuming a Hall r-factor of unity (several authors have pointed out that the Hall r-factor may be much different than unity in p-type GaAs [13, 14].) Figure 1.2(a) shows the result of SIMS profiling of the film. The accuracy of the SIMS analysis of Be concentration was estimated to be ±20%, with a detection limit of $\approx 5\times10^{15}$ cm^{-3}. The spatial coordinate was calibrated using the Si profile; spatial resolution was limited by beam mixing to ≈ 15 nm. The Be profile is quite sharp, and broadly peaked at about 8×10^{19} cm^{-3}. However, some diffusion of Be is evident on the substrate side of the base.

For the case of a non-uniform base doping profile, (1.3) may expressed as [15]

$$\ln I_C = \ln\left[qA_e\left[\int \frac{N_A(x)}{n_{ie}^2(x)D_n(x)}\,dx\right]^{-1}\right] + \frac{qV_{BE}}{k_BT}, \tag{1.5}$$

where integration is over the quasi-neutral base. If we let $\overline{(n_{ie}^2 D_n)}$ represent the average value of $(n_{ie}^2 D_n)$ in the base, then (1.5) becomes

$$\ln I_C = \ln\left[\frac{qA_E\,\overline{(n_{ie}^2 D_n)}}{Q_B}\right] + \frac{qV_{BE}}{k_BT}, \tag{1.6}$$

where Q_B is the number of holes in the base per unit area. It is difficult to determine the precise quasi-neutral base width from the SIMS profile shown in Fig. 1.2(a) because of beam mixing during SIMS analysis, which limits the spatial resolution to ≈ 15 nm, and because of actual Be diffusion during film growth. To estimate the quasi-neutral base width, W_B, we first integrated the Be concentration, as measured by SIMS, from 100 nm to 400 nm distance from the film's surface (the nominal position of the base layer was 200 to 300 nm.) The result of this integration as a function of position is shown in Fig. 1.3. The curve is normalized such that its maximum value represents 100% of the integrated Be concentration. A straight line was then fit to the values of the curve shown in Fig. 1.3 which lie between 10 and 90%. The intersection of that line with the values zero and unity define the position of the quasi-neutral base, which was found to extend from 194 nm to 302 nm, indicating a value of W_B = 108 nm (which is very close to the targeted value of 100 nm; note that the quasi-neutral base width is only negligibly narrowed by depletion). By again integrating the Be concentration, this time from 194 nm to 302 nm, we found $Q_B = 8.5\times10^{14}$ cm^{-2}, which is very near the targeted value of 8.0×10^{14} cm^{-2}. This method of calculating the base width was chosen because it assures that nearly all the charge will be represented in the quantity Q_B.

The average doping in the base was defined to be $\overline{N_A} \equiv Q_B/W_B$. Its value was found to be 7.9×10^{19} cm^{-3}, nearly equal to the targeted doping. A numerical average of the values of Be concentration defined by the 10 to 90% points of the curve in Fig. 1.3 also yielded an estimate of 7.9×10^{19} cm^{-3} for the average base doping.

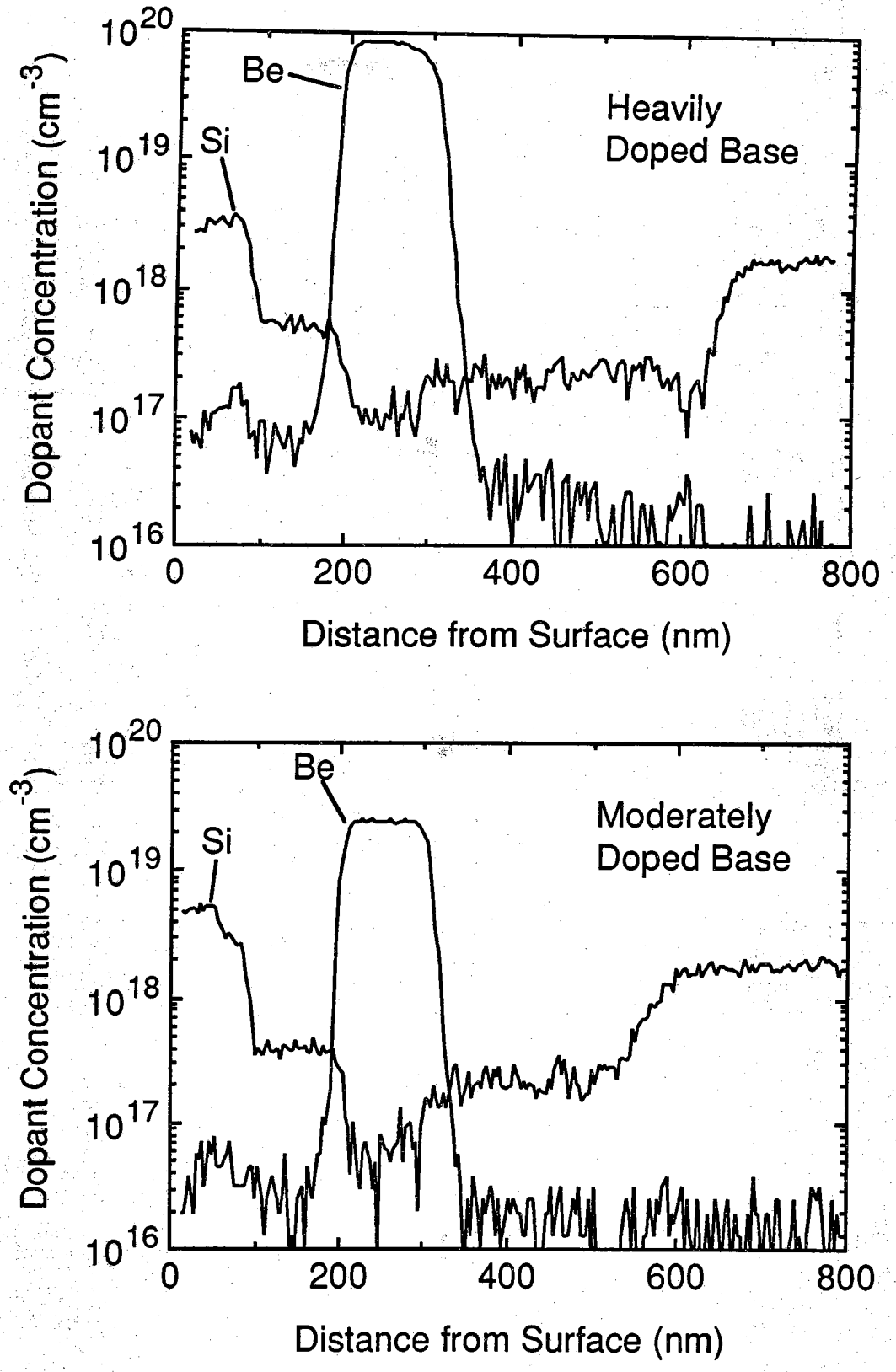

Fig. 1.2 Profile of dopant concentration in the homojunction bipolar transistor films as a function of distance from the surface, as measured by secondary ion mass spectroscopy (SIMS): (a) heavily doped base layer; (b) moderately doped base layer.

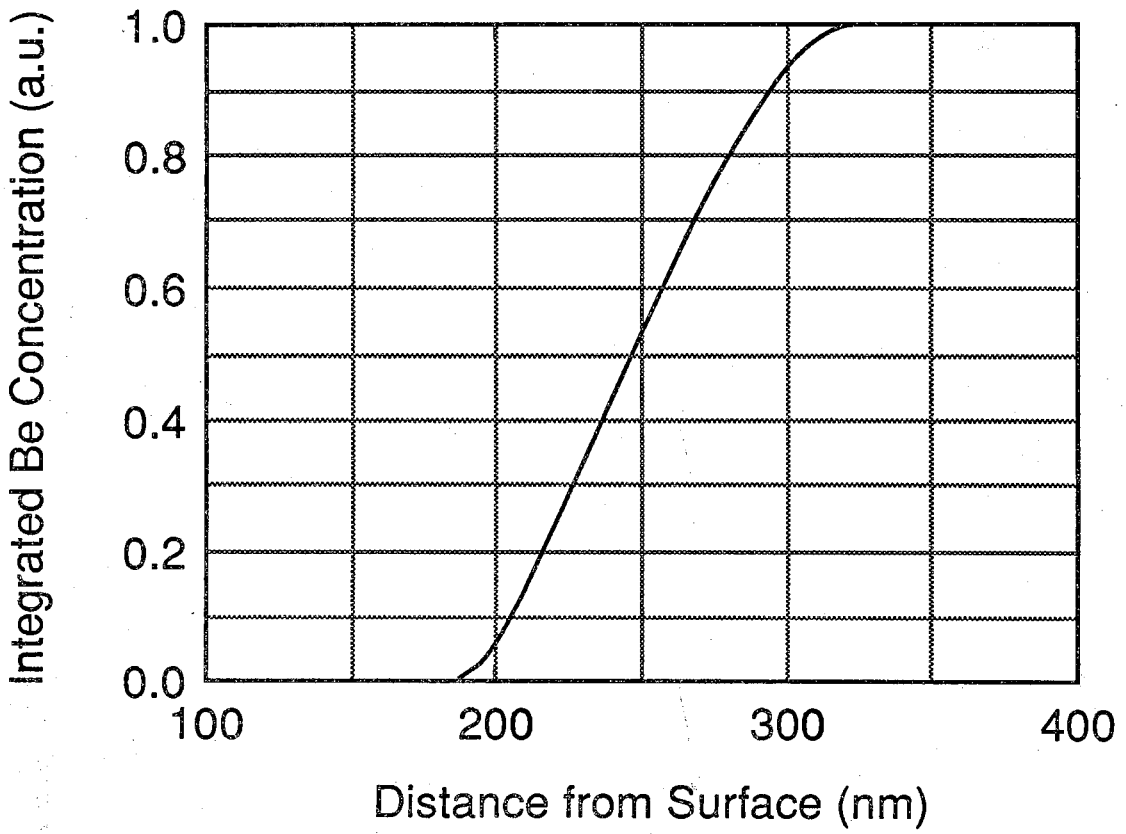

Fig. 1.3 Integral of the Be concentration from 100 to 400 nm distance from the surface of the transistor film with the heavily doped base layer, as measured by SIMS analysis; the curve is normalized such that its maximum value represents 100% of the integrated Be concentration.

The validity of assumption (1.4) may be tested by extrapolating the available data for minority electron diffusion coefficient [16] and lifetime [17]. At a hole concentration of 7.9×10^{19} cm^{-3}, reasonable estimates are $D_n = 20\ cm^2\cdot sec^{-1}$ and τ_n = 0.1 nsec, which yields $L_n \cong 400$ nm. Lievin et al. reported $L_n \approx 250$ nm at a hole concentration of about 10^{20} cm^{-3} [12]. For a base thickness W_B = 108 nm, (1.4) should be well-satisfied. We find that a diffusion length less than 125 nm would be required to reduce the measured collector current by 10% relative to the ideal expression given by (1.3).

I_C-V_{BE} data were compiled for 21 transistors with heavily doped base layers, with emitter dimensions varying from 24 μm × 24 μm to 160 μm × 560 μm. No dependence of collector current density on emitter size was observed. (However, it was necessary to use the fabricated, rather than as-drawn, emitter dimensions in calculating $(n_{ie}^2 D_n)$ from the I_C-V_{BE} characteristic, because of a slight spreading of ≅ 0.5 μm in each direction of the photoresist used to define the emitter mesa.) Data for a 160 μm × 160 μm transistor are displayed in Fig. 1.4. The data comprising the curve labelled "inverted" were measured by reversing the role of the emitter and collector layers. Both curves roll off at higher voltages due to series resistance effects. Note the reciprocal behavior displayed by the linear portion of the curves.

The slope and intercept of the linear part of the I_C-V_{BE} data shown in Fig. 1.4 were determined by least squares fitting. Using (1.6), with $Q_B = 8.5\times10^{14}$ cm^{-2}, we found $\overline{(n_{ie}^2 D_n)} = 2.09\times10^{15}$ $cm^{-4}\cdot sec^{-1}$ and T = 299.4 K. Room temperature, as measured by a thermocouple in the probe station chuck, was also 299.4 K. In order to compare values of $(n_{ie}^2 D_n)$ measured at slightly different temperatures, we can scale the results to T = 300 K [18], using the known temperature dependence of n_{io} [19]. Nine I_C-V_{BE} data sets which were well-described by (1.3) over several orders of magnitude of current were selected for fitting; an average value of $\overline{(n_{ie}^2 D_n)} = 2.08\times10^{15}$ $cm^{-4}\cdot sec^{-1}$ (σ = 1.9%) at T = 300 K was extracted. This value is displayed along with the previously-measured diode data [3] in Fig. 1.1 as an open circle.

Figure 1.2(b) shows the SIMS profile of the second film, with the more moderately doped base layer. The Be profile is ideal, within the resolution of the SIMS technique, having very steep sides and a flat peak $\overline{N_A} = 2.4\times10^{19}$ cm^{-3}. The base width and base charge were W_B = 103 nm and $Q_B = 2.4\times10^{14}$ cm^{-2}, respectively, resulting in an average base doping of $\overline{N_A} = 2.4\times10^{19}$ cm^{-3}. Because of the lack of Be diffusion in this film, the base charge could also have been calculated from the product of the average doping and the targeted base width, so the value of $(n_{ie}^2 D_n)$ is not an average quantity in this case. The resistivity of the base layer material was 2.9×10^{-3} Ω–cm, and the hole mobility and concentration from Hall effect measurements were 88 $cm^2-V^{-1}-sec^{-1}$ and 2.4×10^{19} cm^{-3}, respectively. I_C-V_{BE} data were measured for 17 transistors at temperatures ranging from 297.7 to 298.0 K. Fitting the data to (1.3) and scaling the results to T = 300 K yielded $(n_{ie}^2 D_n) = 1.51\times10^{15}$ $cm^{-4}\cdot sec^{-1}$ (σ = 3.9%).

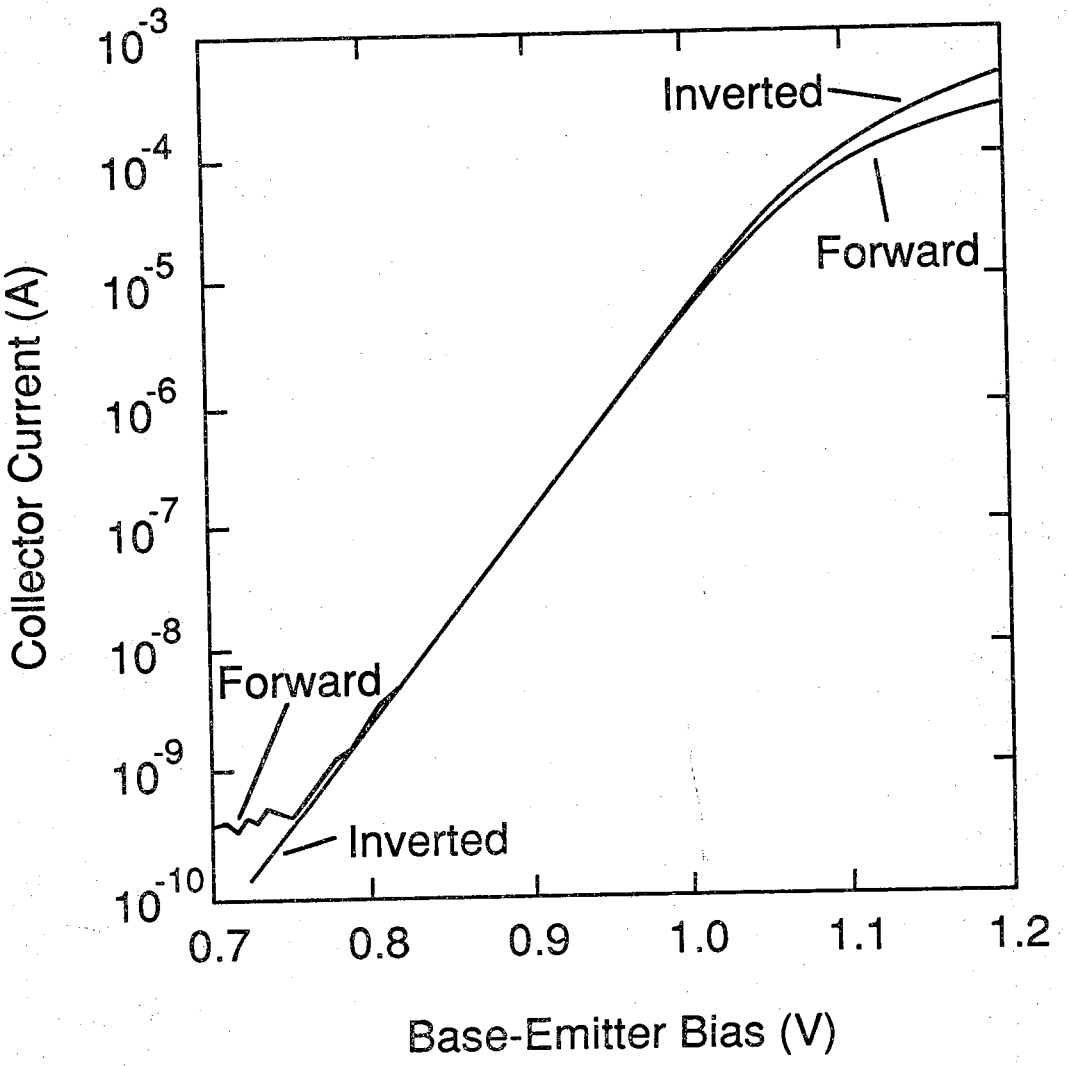

Fig. 1.4 Collector current as a function of base-emitter voltage for a homojunction bipolar transistor with emitter dimensions 160 μm × 160 μm, measured for both normal and inverted operation at a temperature of 299.4 K.

The values of $(n_{ie}^2 D_n)$ measured using the two transistor films discussed here are much larger than those that would be expected assuming a band structure unperturbed by heavy doping. (Note that the solid curve shown in Fig. 1.1, which was calculated assuming an unperturbed band structure as described in the introductory section of this paper, continues to fall off sharply above 3×10^{19} cm^{-3} due to majority carrier degeneracy.) We attribute the large measured values of the collector current to perturbations of the band structure associated with heavy doping, which increase n_{ie}^2. This result is in qualitative agreement with the theoretical work of Bennett and Lowney, who used a detailed many-body approach to calculate the $n_o p_o$ product in p^+-GaAs as a function of acceptor concentration [5]. However, a direct comparison of their results with the experimental data presented in this paper is difficult, because the minority carrier diffusion coefficient D_n has not (to our knowledge) been measured for hole concentrations above 4×10^{18} cm^{-3}.

4. CONCLUSIONS

We have demonstrated a transistor-based technique for measuring electron injection currents in p^+-GaAs doped greater than 10^{19} cm^{-3}. Use of a homojunction bipolar transistor allows a straight-forward interpretation of the measured currents relative to the use of heterojunction bipolar transistors (HBTs) because (1) it facilitates separation of electron and hole current components, and (2) because it assures ideal emitter-base junction behavior. We interpret the large injection currents measured as evidence for significant effective bandgap shrinkage effects. As was found to be the case for Si, these effects must be taken into account for accurate analysis and design of GaAs-based bipolar transistors and solar cells [1,10,18].

Future experimental work should include additional measurements of $(n_{ie}^2 D_n)$ at hole concentrations in the range 10^{18} to 10^{20} cm^{-3}, as well as measurements of the minority carrier mobility for acceptor concentrations from mid-10^{18} to 10^{20} cm^{-3}. Such heavy p-type doping is now commonly employed in the GaAs base of HBTs, where the base transit time is influenced by the minority electron mobility. In addition, knowledge of the minority carrier mobility at high acceptor concentrations would allow the $n_o p_o$ product to be deduced from $(n_{ie}^2 D_n)$ data, and could also shed light on fundamental scattering processes in heavily doped GaAs.

CHAPTER 1 REFERENCES

[1] J. W. Slottboom and H. C. de Graaff, *Solid-State Electron. 19*, 857 (1976).

[2] H. C. Casey, Jr. and F. Stern, *J. Appl. Phys. 47*, 631 (1976).

[3] M. E. Klausmeier-Brown, M. S. Lundstrom, M. R. Melloch and S. P. Tobin, Appl. *Phys. Lett. 52*, 2255 (1988).

[4] E. O. Kane, *Solid-State Electron. 28*, 3 (1985).

[5] H. S. Bennett and J. R. Lowney, *J. Appl. Phys. 62*, 521 (1987).

[6] M. E. Klausmeier-Brown, C. S. Kyono, P. D. DeMoulin, S. P. Tobin, M. S. Lundstrom and M. R. Melloch, *IEEE Trans. Electron Devices ED-35*, 1159 (1988).

[7] F. A. Lindholm and J. G. Fossum, *Electron Device Lett. EDL-2*, 230 (1981).

[8] W. Walukiewicz, J. Lagowski, L. Jastrzebski and H. C. Gatos, *J. Appl. Phys. 50*, 5040 (1979).

[9] M.-C. Chang, P. M. Asbeck, K. C. Wang, G. J. Sullivan, N.-H. Sheng, J. A. Higgins and D. L. Miller, *Electron Device Lett. EDL-8*, 303 (1987).

[10] M. E. Klausmeier-Brown, M. S. Lundstrom, and M. R. Melloch, to appear in *IEEE Trans. Electron Devices* (1989).

[11] R. A. Hamm, M. B. Panish, R. N. Nottenburg, Y. K. Chen and D. A. Humphrey, *Appl. Phys. Lett. 54*, 2586 (1989).

[12] J. L. Lievin, C. Dubon-Chevallier, F. Alexandre, G. Leroux, J. Dangla and D. Ankri, *IEEE. Electron Device Lett. EDL-7*, 129 (1986).

[13] J. D. Wiley, in *Semiconductors and Semimetals, Vol. 10*, ed. by R. K. Willardson and A. C. Beer (Academic Press, New York, 1975) p. 91.

[14] D. C. Look, *Electrical Characterization of GaAs Materials and Devices* (John Wiley & Sons, New York, 1989) p. 59.

[15] A. H. Marshak and C. M. Van Vliet, *Proc. IEEE 72*, 148 (1984).

[16] H. Ito and T. Ishibashi, *J. Appl. Phys. 65*, 5197 (1989).

[17] R. K. Ahrenkiel, in *Current Topics in Photovoltaics, Vol. 3*, ed. by T. J. Coutts and J. D. Meakin (Academic Press Ltd., London, 1988) p. 51.

[18] J. A. del Alamo and R. M. Swanson, *Solid-State Electron. 30*, 1127 (1987).

[19] J. S. Blakemore, *J. Appl. Phys. 53*, R123 (1982).

CHAPTER 2

HEAVY DOPING EFFECTS IN p^+ GaAs: Results

2.1 INTRODUCTION

Measurements of the collector current versus base-emitter voltage characteristics of n-p-n Si bipolar transistors showed a strong enhancement of the electron current injected into p^+-Si [1]. Those enhanced electron injection currents have been attributed to doping-induced perturbations of the band structure which increase the $n_o p_o$ product [2]. Such heavy doping effects must be treated for accurate design and modeling of Si bipolar transistors and solar cells [1, 3]. While heavy p-type doping has been known to affect optical transitions in GaAs [4], its effect on the electrical performance of GaAs devices has only recently been explored. In a previous paper we characterized electron injection currents in p^+-n GaAs diodes with p-layers doped from mid-10^{17} to 10^{19} cm^{-3} [5]. Those results showed heavy doping effects in p^+-GaAs analogous to those observed in p^+-Si, but the technique used was limited to dopings $\leq 10^{19}$ cm^{-3}. In Chapter 1 we presented a new technique for measuring heavy doping effects in p-GaAs based on characterization of the collector saturation current of n-p^+-n GaAs homojunction bipolar transistors. This new transistor based technique has allowed us to extend the doping range where we have measured the effects of acceptor doping of GaAs to 8×10^{19} cm^{-3}. The results show significant heavy doping effects up to 8×10^{19} cm^{-3} and are consistent with the diode measurements below 10^{19} cm^{-3}. These heavy doping effects must be treated to accurately model GaAs bipolar devices.

Consider an n-p-n homojunction bipolar transistor (BJT) having a spatially uniform base doping profile. When the emitter-base junction is forward-biased and the base-collector junction short-circuited or reverse-biased, the collector current density versus base-emitter voltage characteristic is described by

$$J_c = \frac{q(n_o D_n)}{W_B} \exp\left[\frac{qV_{BE}}{kT} - 1\right] \tag{2.1}$$

where n_o is the equilibrium electron concentration in the p-type base, D_n is the diffusion coefficient of the minority-carrier electrons, and W_B is the width of the quasi-neutral portion of the base. A quantity called the effective intrinsic carrier concentration n_{ie} may be introduced to relate n_o to the ionized dopant density N_A, such that $n_o \equiv \frac{n_{ie}^2}{N_A}$. Measurements in heavily doped Si have shown that n_{ie} considerably exceeds n_{io}, the intrinsic carrier concentration in lightly doped Si. For the purpose of device modeling , the measured relationship between n_{ie} and n_{io} may be described by defining a non-physical effective bandgap shrinkage parameter [3, 6].

Homojunction bipolar transistors were chosen for this work instead of the more common heterojunction bipolar transistors (HBTs); misalignment of the doping and compositional junctions due to dopant diffusion, or improper grading of the emitter aluminum composition in an HBT could result in a conduction band energy barrier at the emitter-base junction which would invalidate (2.1). The technique used in this work to quantify electron injection currents as a function of p-layer hole concentration was pioneered by Slotboom and de Graaff [1], and was described in detail in Chapter 1 for GaAs BJTs and also in reference [7]. Such transistor measurements facilitate the separation of hole and electron current components. In this chapter the results are reported in terms of the quantity most directly obtained from the measurement of collector current versus base-emitter voltage, the product ($n_o D_n$).

2.2 EXPERIMENTAL RESULTS

The targeted layer thicknesses and dopings of the films used in these experiments are described in Table 2.1. The films were all grown in a Varian GEN-II molecular beam epitaxy (MBE) system on n^+-GaAs substrates at a substrate temperature of 600°C (the oxide desorption temperature was 580°C). The growth rate was 1 μm/hr; film thickness was monitored by counting oscillations in the reflection high-energy diffraction (RHEED) pattern during non-critical portions of the growth. The p- and n-type dopants were Be and Si, respectively. Standard optical lithography and wet etching procedures were employed in device fabrication. Seven films were studied, with targeted base layer Be concentrations of 2×10^{18} to 8×10^{19} cm^{-3}. The slope of a plot of carrier concentration in the p-type material as a function of Be oven temperature was consistent with the vapor pressure curve of Be in this doping range, implying the absence of significant precipitation of Be even at the highest doping level. Further details of film growth and device fabrication have been described elsewhere [7].

Dopant and carrier concentrations in the p-type base layer of each film were characterized in several ways. Secondary ion mass spectroscopy (SIMS) was used to probe the Be profile. Use of a Be-implanted calibration standard resulted in an absolute accuracy of ±20 %. Si concentration was also monitored during the SIMS analysis, and the Si profile was used to calibrate the spatial coordinate; beam mixing limited spatial resolution to 150 Å. The base layer hole concentrations were also probed by Hall effect. The average Be concentration found in the base layer of each film by SIMS is listed in the first column of Table 2.2; also displayed in Table 2.2 are the base layer hole concentration and mobility found by Hall effect measurements (assuming a Hall r-factor of unity). Although the hole concentration values derived from Hall effect measurements are as much as 30% lower than the Be concentration values given by SIMS, we believe that the p-type material is essentially uncompensated. Several authors have pointed out that the Hall r-factor may be quite different than unity in p-type GaAs, leading to uncertainty concerning the reliability of hole concentration values derived from Hall effect measurements [8, 9]. Since the incorporation of Be in the films was ideal [7], we equate the base layer hole concentration p_o with the average base layer Be concentration in each film.

TABLE 2.1 Targeted layer thicknesses and dopings of the MBE-grown homojunction bipolar transistor films used in this study.

Layer Composition	Function	Thickness (Å)	Dopant Concentration (cm^{-3})
n^+-GaAs	Contact Layer	1000 to 2000	$\geq 2\times10^{18}$
n-GaAs	Emitter	1000	5×10^{17}
p^+-GaAs	**Base**	**1000 to 3000**	**2×10^{18} to 8×10^{19}**
n-GaAs	Collector	2000 to 3000	2×10^{17}
n^+-GaAs	Sub-Collector	10,000	$\geq 10^{18}$
n^+-GaAs	Substrate	...	$\geq 10^{18}$

TABLE 2.2 Summary of the measurements made using homojunction bipolar transistors.

Be Concentration from SIMS (cm^{-3})	Targeted Base Width (Å)	Hole Concentration from Hall Effect (cm^{-3})	Hole Mobility from Hall effect ($cm^2\ V^{-1}\ s^{-1}$)	Measurement Temperature (K)	(n_oD_n) at 300 K ($10^{-5}\ cm^{-1}\ s^{-1}$)
2.0×10^{18}	3000	1.4×10^{18}	178	297.4	51.5
6.5×10^{18}	2000	4.6×10^{18}	134	299.2	23.1
1.5×10^{19}	1000	1.0×10^{19}	104	298.1	10.5
2.4×10^{19}	1000	2.4×10^{19}	88	297.9	6.30
3.2×10^{19}	1000	2.6×10^{19}	86	298.7	4.94
5.3×10^{19}	1000	4.1×10^{19}	82	298.3	3.60
7.9×10^{19}	1000	6.0×10^{19}	76	299.4	2.63

The SIMS profiles of Be in the all but two of the films were ideal, within the resolution of the analysis, exhibiting very steep sides and flat peaks. The Be profile was slightly non-uniform in each of the two most heavily doped films, displaying broad flat peaks over most of the base width, but showing evidence of some diffusion of Be on the substrate side of the base [7]. The base width and average base doping for those two films was estimated by a careful spatial integration of the Be profile, and the reported value of $(n_o D_n)$ necessarily represents an average quantity as described in Ref. [7].

The collector current density was measured as a function of emitter-base voltage, with the base and collector shorted, for a number of transistors on each film. The J_c–V_{BE} data were well-described by (2.1) in all cases, except at low biases where leakage currents were important, and at high biases where series resistance was important. The quantity $(n_o D_n)$ was determined from the intercept of the linear portion of a plot of ln J_c versus V_{BE}; the device temperature could also be found from the slope of the plot. The temperature measured by a thermocouple agreed with the temperature found from fitting the ln J_c versus V_{BE} plot to within 0.2 K for all devices.

Equation (2.1) is valid only so long as recombination in the base is not significant. This constraint is most severe for the film with the most heavily doped base layer (7.9×10^{19} cm^{-3}). For this film we estimate that an electron diffusion length less than 1250 Å would be required to reduce the measured collector current by 10%, whereas Lievin et al. reported a diffusion length of approximately 2500 Å at a hole concentration of about 10^{20} cm^{-3} [10], so it seems likely that (2.1) is valid even in this case.

Results of the extraction of $(n_o D_n)$ from the measured J_c–V_{BE} data are listed in the last column of Table 2.2. The actual measurement temperature is also listed in Table 2.2. Following del Alamo [3], we have scaled all $(n_o D_n)$ products to T = 300 K using the known temperature dependence of n_{io} [11]. The maximum error introduced by this temperature scaling should not exceed 2%. Fig. 2.1 is a plot of $(n_o D_n)$ as a function of hole concentration in p-type GaAs at T = 300 K. Both the transistor data listed in Table 2.2 and the previously reported diode data [5, 12] are shown in Fig. 2.1. (Recall that $(n_o D_n)$ is proportional to the electron current injected into the base of a bipolar transistor, so its value has a direct relationship to the gain of an HBT [6].) Two other curves are shown in Fig. 2.1 for comparison with the measured data. The lower curve, labeled "No Bandgap Shrinkage", was computed without considering any heavy doping effects except degeneracy of the hole gas [5], with $n_{io} = 2.25\times10^6$ cm^{-3} [11]; D_n was estimated from a fit to the measured minority-carrier mobility values [6]. The curve is dashed above 4×10^{18} cm^{-3} because that is the highest hole concentration at which the minority electron mobility has been measured [13]. The difference between this curve and the measured data is more than an order of magnitude above 10^{19} cm^{-3}, and underlines the importance of considering these effects. The second curve in Fig. 2.1, labeled "Theory", makes use of the theoretical work of Bennett and Lowney, who used a detailed many-body approach to calculate the ratio n_{ie}/n_{io} as a function of hole concentration in p^+-GaAs [14]. Again, $n_{io} = 2.25\times10^6$ cm^{-3}, and D_n was estimated from

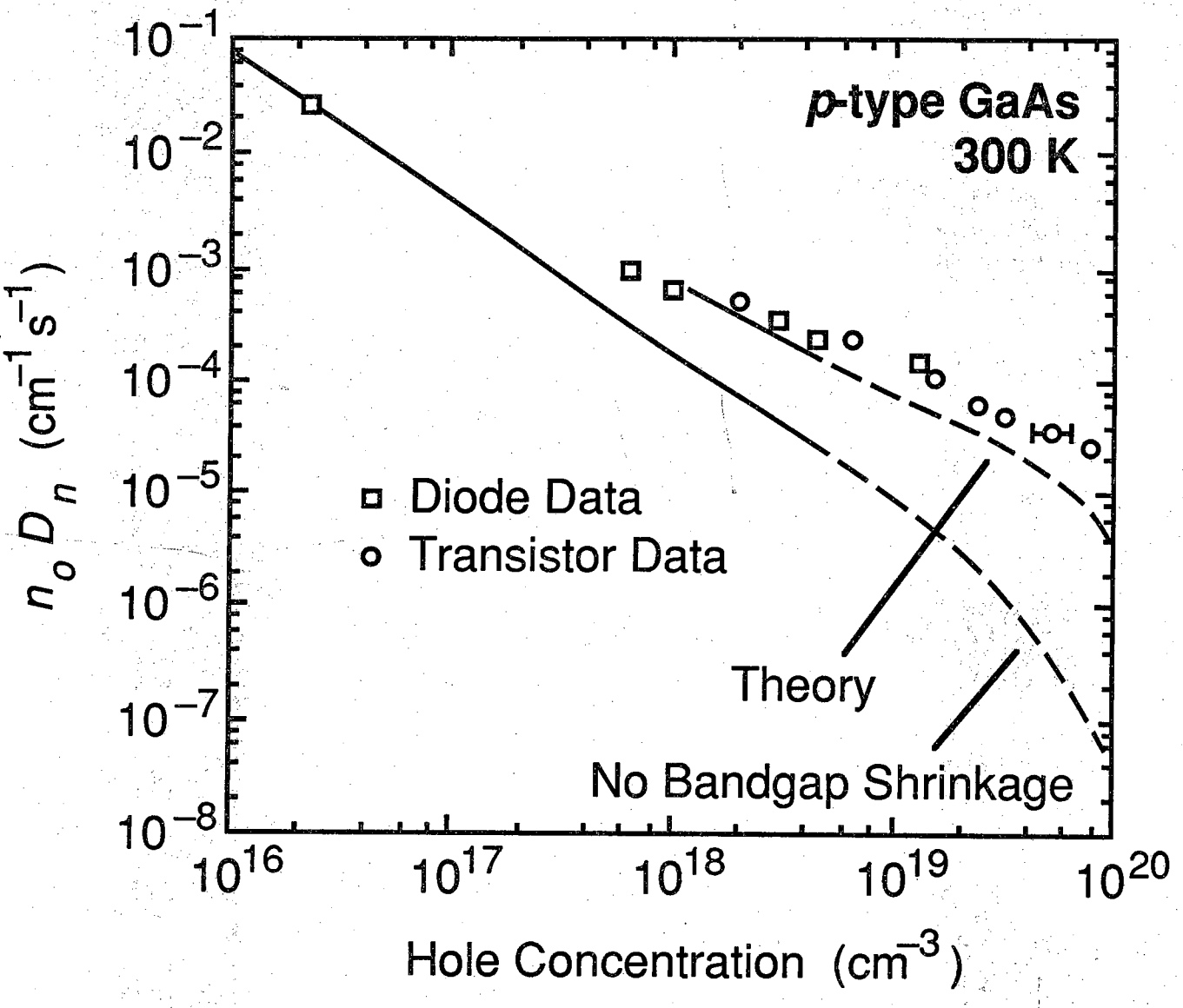

FIG. 2.1 The quantity (n_oD_n) in p-type GaAs at T = 300 K. The squares represent diode data [5, 12], and the circles represent the transistor data from Table 2.2. The error bar represents an uncertainty of ±20% in the magnitude of the Be concentration from SIMS analysis of the transistor films. The curve labelled "Theory" was constructed from calculations of n_{ie}/n_{io} [14] combined with a fit to measured minority carrier mobility data [6]. The curve labelled "No Bandgap Shrinkage" was constructed assuming no heavy doping effects except hole gas degeneracy [5].

measured values as just described. The theoretical curve agrees within a factor of two with the measured results over most of the measured range of hole concentrations.

One might expect that effective bandgap shrinkage in p^+-GaAs would be qualitatively similar to the well-characterized effects in p^+-Si. Fig. 2.2 is a plot of $(n_o D_n)$ as a function of hole concentration in p-type Si at T = 300 K. The experimental curve was constructed using fits for minority electron mobility (i.e. D_n) and effective bandgap shrinkage as functions of hole concentration, as given by Swirhun et al. [15]. The curve labeled "No Bandgap Shrinkage" was constructed in the same way as the analogous curve in Fig. 2.1, using the minority-carrier mobility fit of Swirhun et al. Both curves in Fig. 2.2 were constructed using $n_{io} = 1.18 \times 10^{10}$ cm^{-3}. A comparison of Fig. 2.1 and Fig. 2.2 reveals that the behavior of $(n_o D_n)$ as a function of hole concentration in p^+-GaAs and p^+-Si displays a similar trend. (The large difference in the vertical scale factor is accounted for by the large difference in n_{io} for GaAs and Si.) While caution is necessary in extrapolating the p^+-GaAs minority-carrier mobility data, it appears that the effective bandgap shrinkage is somewhat stronger in p^+-Si for dopant concentrations above 10^{19} cm^{-3}.

For the purpose of device modeling, a non-physical effective bandgap shrinkage parameter is often introduced to describe the measured relationship between n_{ie} and n_{io}, where $n_{ie}^2 \equiv n_o N_A$. A commonly used definition is [3, 6]:

$$\Delta E_G^o \equiv k_B T \ln(n_{ie}^2 / n_{io}^2)$$

We do not quote apparent bandgap shrinkage values in this letter because extraction from the measured $(n_o D_n)$ values depends on knowledge of the minority-carrier mobility (or D_n). A previously presented expression for ΔE_G^o as a function of hole concentration which was based on measurements of $(n_o D_n)$ at lower dopant concentrations [6] appears to overestimate the effective bandgap shrinkage for dopant concentrations > 10^{19} cm^{-3}.

2.3 SUMMARY

In summary, measurements of electron current injected into the base of n-p^+-n GaAs homojunction transistors were presented. The large magnitude of the measured currents was attributed to heavy doping effects in p^+-GaAs. These effects are analogous to the so-called bandgap shrinkage effects observed in p^+-Si. As was found to be the case for Si, heavy doping effects must be treated to correctly model GaAs-based bipolar transistors and solar cells [6, 16]. However, further work is necessary to measure the minority electron mobility for hole concentration greater than 10^{19} cm^{-3}, and to examine the effects of heavy doping in n-type GaAs.

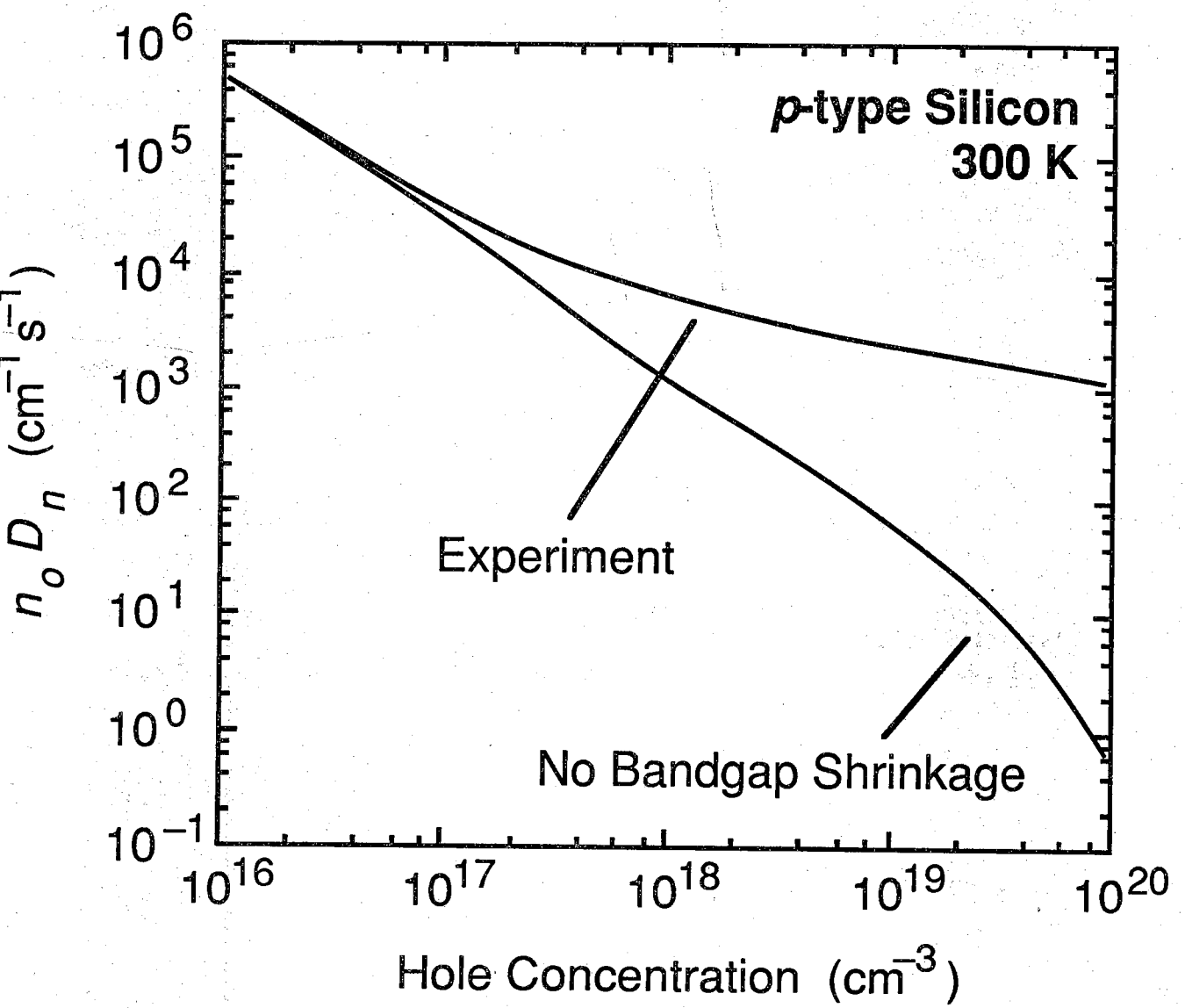

FIG. 2.2 The quantity ($n_o D_n$) in p-type Si at T = 300 K. The curve labelled "Experiment" was constructed using fits for minority electron mobility (i.e. D_n) and effective bandgap shrinkage as functions of hole concentration, as given by Swirhun et al. [15]. The curve labelled "No Bandgap Shrinkage" was constructed assuming no heavy doping effects except hole gas degeneracy.

References

[1] J. W. Slotboom and H. C. de Graaff, *Solid-State Electron. 19*, 857 (1976).

[2] J. R. Lowney and H. S. Bennett, *J. Appl. Phys. 53*, 433 (1981).

[3] J. A. del Alamo and R. M. Swanson, *Solid-State Electron. 30*, 1127 (1987).

[4] H. C. Casey, Jr. and F. Stern, *J. Appl. Phys. 47*, 631 (1976).

[5] M. E. Klausmeier-Brown, M. S. Lundstrom, M. R. Melloch and S. P. Tobin, *Appl. Phys. Lett. 52*, 2255 (1988).

[6] M. E. Klausmeier-Brown, M. S. Lundstrom and M. R. Melloch, *IEEE Trans. Electron Devices* (in press).

[7] M. E. Klausmeier-Brown, M. R. Melloch and M. S. Lundstrom, *J. Electron. Mater.* (in press).

[8] J. D. Wiley, in *Semiconductors and Semimetals*, edited by R. K. Willardson and A. C. Beer (Academic, New York, 1975) p. 91, Vol. 10.

[9] D. C. Look, *Electrical Characterization of GaAs Materials and Devices* (Wiley, New York, 1989) p. 59.

[10] J. L. Lievin, C. Dubon-Chevallier, F. Alexandre, G. Leroux, J. Dangla and D. Ankri, *IEEE Electron Device Lett. EDL-7*, 129 (1986).

[11] J. S. Blakemore, *J. Appl. Phys. 53*, R123 (1982).

[12] H. L. Chuang, P. D. DeMoulin, M. E. Klausmeier-Brown, M. R. Melloch, and M. S. Lundstrom, *J. Appl. Phys. 64*, 6361 (1988).

[13] M. I. Nathan, W. P. Dumke, K. Wrenner, S. Tiwari, S. L. Wright and K. A. Jenkins, *Appl. Phys. Lett. 52*, 654 (1988).

[14] H. S. Bennett and J. R. Lowney, *J. Appl. Phys. 62*, 521 (1987).

[15] S. E. Swirhun, D. E. Kane, and R. M. Swanson, *IEDM Tech. Dig.*, 298 (1988).

[16] M. E. Klausmeier-Brown, P. D. DeMoulin, M. S. Lundstrom, and M. R. Melloch, *Conf. Rec. 20th IEEE Photovoltaic Specialists Conference*, 503 (1988).

CHAPTER 3

HIGH-EFFICIENCY MBE-GROWN GaAs SOLAR CELLS

3.1 INTRODUCTION

Molecular beam epitaxy (MBE) has proven to be an important film growth technique for most advanced device research due to the relative ease with which complex compositional and doping profiles can be grown. However, solar cells fabricated from MBE-grown material have been inferior in performance to those fabricated from metal organic chemical vapor deposited (MOCVD) material. Solar cells are large area minority carrier devices and typically range in area from 0.25 cm^2 to 4 $cm.^2$ Table 3.1 is a summary of solar cell results for MOCVD [1-4] and MBE [5-8] films clearly illustrating that previous to this work solar cells fabricated from MOCVD material were superior to solar cells fabricated from MBE material. The previously best reported MBE-cell had a 1-sun AM1.5 efficiency of 15.7% without an antireflection coating [8] while MOCVD-cells have achieved efficiencies of 24.8% [4].

We have recently fabricated solar cells on an MBE-grown film whose material quality and cell performance are comparable to MOCVD-grown solar cells. Details of the MBE system preparation and MBE film growth procedure along with a detailed evaluation of the solar cells will be presented.

3.2 PREPARATION OF THE MBE SYSTEM

The MBE system used was a modular Varian GEN II. The furnaces were originally outgassed one at a time in a 35 cm-long, 6 cm-diameter nipple which was attached to a port on the entry chamber of the MBE. The nipple was mounted vertically via a 90° elbow. The nipple was water cooled with a copper tube which was wrapped around and brazed to the nipple. (The furnace sizes used for each source are listed in Table 3.2 along with the maximum temperatures used for outgassing.) The furnaces without pyrolytic born nitride (PBN) crucibles were outgassed for approximately 3 hrs at the maximum temperatures listed in Table 3.2. The furnaces were than ramped from room temperature to their maximum operating temperatures several times to have maximum current flowing through the heater windings and hence maximum heating and outgassing. A PBN crucible was then loaded into the furnace and outgassed for 1-2 hours at the temperature listed in Table 3.2. The furnace was then loaded into the growth chamber.

When all the furnaces were loaded in the growth chamber, a thermal cleaning of the growth chamber was conducted. With dry nitrogen flowing through the radial vane and cryoshrouds,

Table 3.1 Summary of MOCVD- and MBE-grown solar cell performance.

Growth Technique	Spectrum	Eff (%)	V_{oc} (V)	J_{sc} (mA/cm^7)	FF (%)	Area (cm^2)	Group	Ref
MOCVD	AM1.5	24.5	1.033	27.28	86.8	1.0	Spire	1
MOCVD	AM1.5	24.0	1.046	27.12	84.5	4.0	Varian	2
MOCVD	AM1.5	23.7	1.019	27.35	84.9	1.0	Kopin	3
MOCVD	AM1.5	24.8	1.029	27.89	86.43	0.25	Spire	4
MBE	AM1.5	23.8	1.018	27.56	84.65	0.25	Purdue	This Work
MBE	AM1	16.0	0.92	23.0	76.0	0.095	Lincoln Labs	5
MBE	AM1	17.5	0.867	29.2	69.3	0.25	Rockwell	6
MBE	AM1.5	17.1	0.94	23.9	76.3	-	NTT	7
MBE	AM1.5	15.8*	0.939	22.07	76.5	0.05	CNRS	8

*Cells did not have an anti-reflection coating.

Table 3.2 Source furnace outgas temperatures

Source	Varian oven size	Maximum Outgas temperature without PBN crucible	Maximum Outgas temperature with PBN crucible
As_4	120 cc	800°C	1050°C
Ga	60 cc	1000°C	1100°C
Al	60 cc	1000°C	1100°C
Si	5 cc	1500°C	1600°C
Be	5 cc	1500°C	1600°C

the furnaces were heated to 600°C along with the substrate heater. The purpose of the dry nitrogen was to avoid any excessively hot spots. The substrate heater was pointed for 45 min at the top, bottom, and load positions to heat the chamber walls. After the growth chamber walls were thermally cleaned, with liquid nitrogen now flowing through the radial vane and cryoshrouds, the furnaces were outgassed at the maximum temperatures listed in Table 3.2 for 3 hours.

The vendors and purities of the source material used are listed in Table 3.3. Since the Be and Si furnaces were placed in downward looking ports, the dopant sources had to be melted in the crucibles so they would adhere to the walls of the crucible. This melting was performed in the outgas nipple which was mounted vertically on the entry chamber and hence results in a symmetrical distribution of the dopant in the crucible. One gram of Be and 1/3 cc of Si chips were used in the dopant furnaces. The Ga crucible was filled with 75 gm of material. Seven Al pellets of 3 mm x 4-8 mm diameter were placed in the 60 cc crucible. This small amount of Al in the 60 cc crucible allows refreezing of the Al everyday without cracking of the PBN crucible. After loading the source material, the MBE system was baked for 72 hrs at 180°C. All furnaces were set at 200°C during the bake-out except for the As_4 furnace which was not heated. As a final note on the MBE system, all furnaces are set at 200°C except for the As_4 furnace which is set to 100°C and liquid nitrogen is not circulated through the radial vane or cryoshroud when the system is not in use.

3.3 MBE FILM GROWTH

The film was grown on a two-inch n^+ GaAs liquid-encapsulated-Czochralski wafer. It was the 33rd film grown in the MBE system after the initial loading of source material. (It should be noted that the 25th film grown in this system was a modulation doped heterojunction which had a mobility of $2x10^6 cm^2/Vs$ at 4.2 K indicating extremely high material quality [9].) The wafer was degreased, etched in a 60°C solution of 5:1:1 H_2SO_4:H_2O_2:H_2O for one minute, and placed in a non-indium wafer mount. The sample was then loaded on a carrying trolley and placed into the entry chamber of the MBE. The sample and trolley was outgassed at 200°C for two hours in the entry chamber. The trolley was then moved into the buffer chamber of the MBE. The sample was outgassed at 300°C for one hour on a heater station in the buffer chamber immediately before being loaded in the growth chamber. Liquid nitrogen was circulated through the radial vane and cryoshrouds starting two hours before initiating growth.

The MBE layers were grown at a substrate temperature of 600°C (580°C is the oxide desorption temperature) and the wafers were rotated at five revolutions per minute during most of the film growth. The film growth rates were determined from monitoring the intensity of the specular spot of the reflection high energy electron diffraction pattern [10].

The cross-section of the film is shown in Fig. 3.1. All layers were grown at a rate of 1.0 μm/hr except for part of the superlattice back surface field (BSF) layer. At a GaAs growth rate of 1

Table 3.3 Source Material

Source	Vendor	Form	Purity
As	Furakawa	120 cc slug	7N
Ga	Alcan Electronic Materials	100 gm bottle	8N
Al	Morton Thiokal Incorporated	3mm thick X 4-8mm diameter pellets	6N
Be	Atomergic Chemetals Corp.	0.33 gm chunks	5N
Si	Wacker-Chemitronic GMBH	crystalline wafer	carrier concentration $< 10^{14}$ cm^{-3}

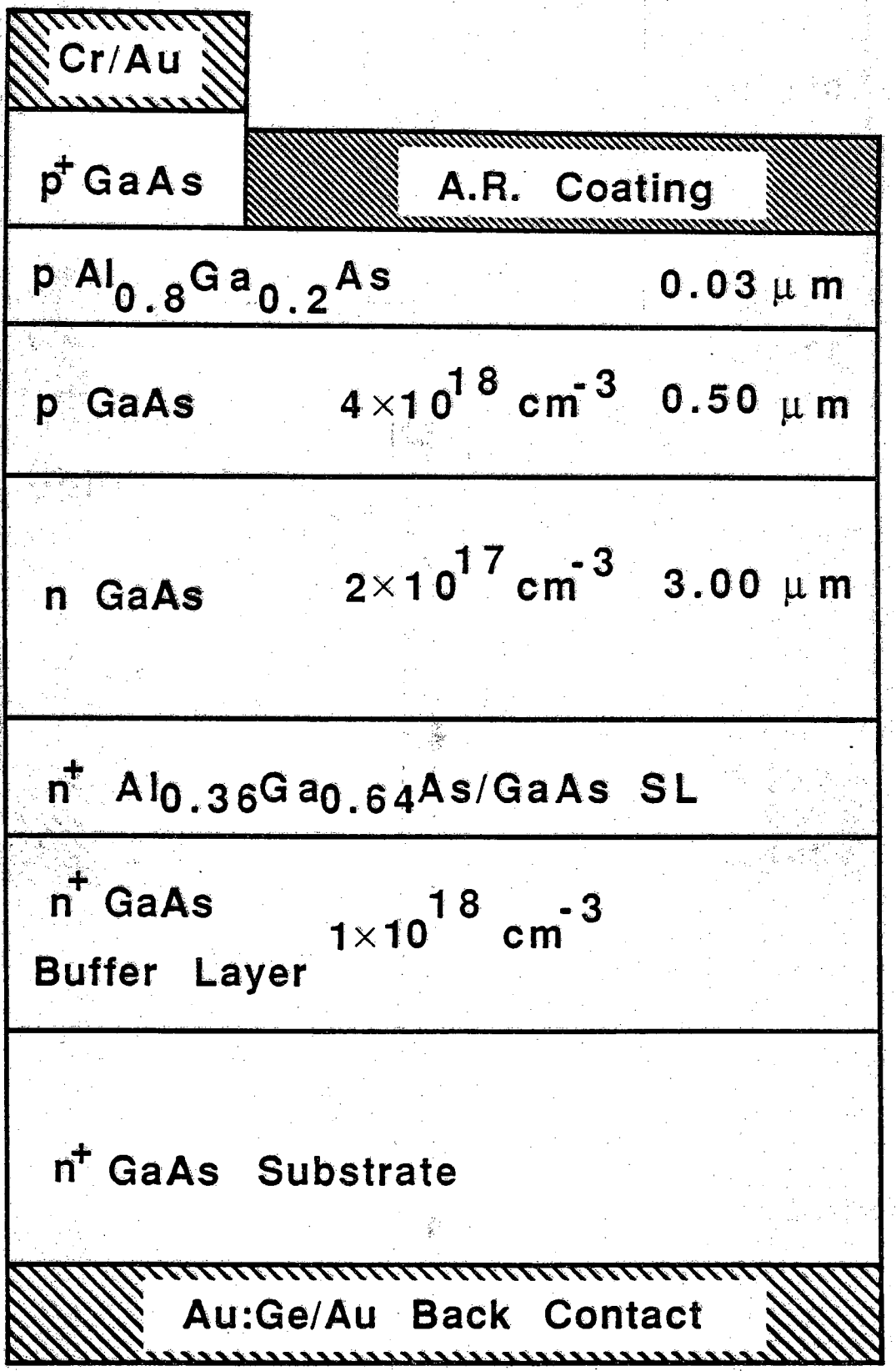

Fig. 3.1 Cross-section of the GaAs solar cell.

μm/hr, the As_4 to Ga beam equivalent pressure was 20 as determined by an ion gauge placed in the substrate growth position. The superlattice BSF layer consisted of a 20 period superlattice of 28Å $Al_{0.36}Ga_{0.64}As$ barriers and 27Å wells. (The $Al_{0.36}Ga_{0.64}As$ barriers were grown at a rate of 1.0 μm/hr and the GaAs wells at 0.64 μm/hr.) The superlattice BSF layer acts as a barrier to minority carrier holes in the n-GaAs region which increases the probability of their collection across the pn junction. A superlattice was used for this purpose rather than just a thick AlGaAs region since, in MBE, a GaAs region grown on a superlattice exhibits a better electrical interface than when a GaAs region is grown on a thick AlGaAs region [11,12].

After film growth the wafer was cleaved in half and solar cells were fabricated on one half. Test devices were fabricated and film characterizations (electrochemical profiling) were performed on the other half. The post-growth solar cell processing sequence was performed at Spire Corporation and has been described previously [13] and is briefly as follows. First, the wafer front was coated with SiO_2. Next a thin AuGe back ohmic contact layer was evaporated and alloyed, followed by an evaporated Au back metallization. Image-reversal photolithography was used to form a pattern for front grid metallization[14]. After etching SiO_2 in the grid openings, Cr and Au were evaporated for front contacts. The photoresist was dissolved to lift off excess metal, then the contacts were sintered. Photolithography was used to define a pattern for the mesa etch (0.5cm by 0.5 cm junctions), then a phosphoric acid-based etchant was used to form the mesa. All remaining SiO_2 was removed just prior to a selective cap removal etch (ammonium hydroxide-hydrogen peroxide system). The etch removed the GaAs cap layer everywhere except under the grid lines and exposed the AlGaAs window layer. Finally, a double-layer antireflection coating of ZnS and MgF_2 was thermally evaporated.

3.4 EXPERIMENTAL RESULTS

The half of the wafer which was processed into solar cells contained 15 solar cells of dimension 0.5 cm by 0.5 cm. The solar cells were measured under 1-sun AM1.5 conditions at Spire Corporation and the Solar Energy Research Institute. A yield of 100% was obtained with the best cell demonstrating an efficiency of 23.8%. Excellent uniformity was also obtained with an average efficiency of 23.1% and a standard deviation of 0.4%. The measured solar cell parameters for our most efficient MBE-grown cell are listed as the first MBE entry in Table 3.1.

As can be seen from the Table 3.1 comparison of MOCVD- and MBE-grown solar cells, ours is the first MBE-grown solar cell of comparable performance to MOCVD-grown solar cells. In comparing our MBE-grown solar cell to the best reported MOCVD-grown cell [4], the major difference in the cells is the fill factor (FF). FF relates the maximum power (P_m) obtainable from the cell to the product of the open-circuit voltage (V_{oc}) and short-circuit current (I_{sc}) of the cell, $FF=P_m/I_{sc}V_{oc}$. The more nearly square the diode's current-voltage (IV) characteristic, the higher the FF. The lower FF for our MBE-grown cells is due to non-ideal leakage currents at low current levels. These leakage currents will be discussed below.

The current of a mesa-isolated GaAs pn junction is comprised of components due to recombination in the bulk space-charge region, recombination within the space-charge region exposed at the perimeter of the mesa, and recombination in the bulk neutral regions. Therefore, the current-voltage characteristic of a GaAs pn junction is expected to have the form,

$$I=J_{O2B}A(e^{qV/2kT}-1)+J_{O2P}P(e^{qV/2kT}-1)+J_{O1}A(e^{qV/kT}-1) \quad (3.1)$$

where J_{O2B} is the bulk saturation current component (A/cm^2), J_{O2P} is the perimeter component (A/cm), J_{O1} is the diffusion saturation current component (A/cm^2), A is the area of the diode and P is the perimeter. A non-ideal leakage current manifests itself as a region of the lnI vs V plot whose slope is less than q/2kT. Such a leakage current will result in a decrease in the FF of a solar cell.

To investigate leakage currents in our films, a series of mesa-isolated diodes were fabricated on the other half of our two-inch wafer and also on a second wafer whose film structure was similar to that shown in Fig. 3.1. These mesa-isolated diodes ranged in area from $2.5x10^{-5}$ cm^2 to 0.25 $cm.^2$ Shown in Fig. 3.2 is the IV characteristic for one of the 0.25 cm^2 diodes which exhibits a non-ideal leakage current. All 15 of the solar cells and all 5 of the 0.25 cm^2 diodes exhibit this non-ideal leakage current. (Note a solar cell has a grid metallization on the top surface while a diode is completely metalized.) Also shown in Fig. 3.2 is the IV characteristic for two different 0.01 cm^2 diodes. The IV characteristic of one of these 0.01 cm^2 diodes is ideal without any leakage current while the other 0.01 cm^2 diode has a leakage current. The correlation between leakage current and diode area is more fully displayed in Table 3.4 and indicates that the source of the leakage current is isolated defects. The oval defect density in our two films was 500 cm^{-2} and also displayed in Table 3.4 is the average number of oval defects for that given area diode. Because the top surface of the diode was metallized, the actual number of oval defects a diode had could not be determined. However the correlation between the oval defect density and the leakage currents suggest that the oval defects are a likely source of leakage currents.

The q/2kT current of a mesa-isolated GaAs diode is comprised of components due to recombination in the bulk space-charge region and within the space-charge region exposed at the perimeter of the mesa. From equation (1) we see that we can write the q/2kT saturation current as,

$$I_{O2}=J_{O2B}A+J_{O2P}P \quad (3.2)$$

By plotting I_{O2}/A versus perimeter-to-area (P/A) ratio, the bulk and perimeter components can be extracted from the slope and intercepts of the plot. The series of mesa-isolated diodes described previously had P/A ratios varying form 40 to 800 $cm.^{-1}$ From the measured IV characteristics of these test diodes, the q/2kT current was extracted by curve fitting to (1) and plotted as shown in Fig. 3.3. From the slope of Fig. 3.3 one obtains $J_{O2P}=1.58x10^{-13}$ A/m. Because the intercept is small an accurate value for J_{O2B} cannot be obtained but we can say that $J_{O2B}<2.5x10^{-11}$ $A/cm.^2$ So even for the large 0.25 cm^2 solar cells the q/2kT current is due to perimeter recombination as has been observed before for high quality MOCVD GaAs diodes

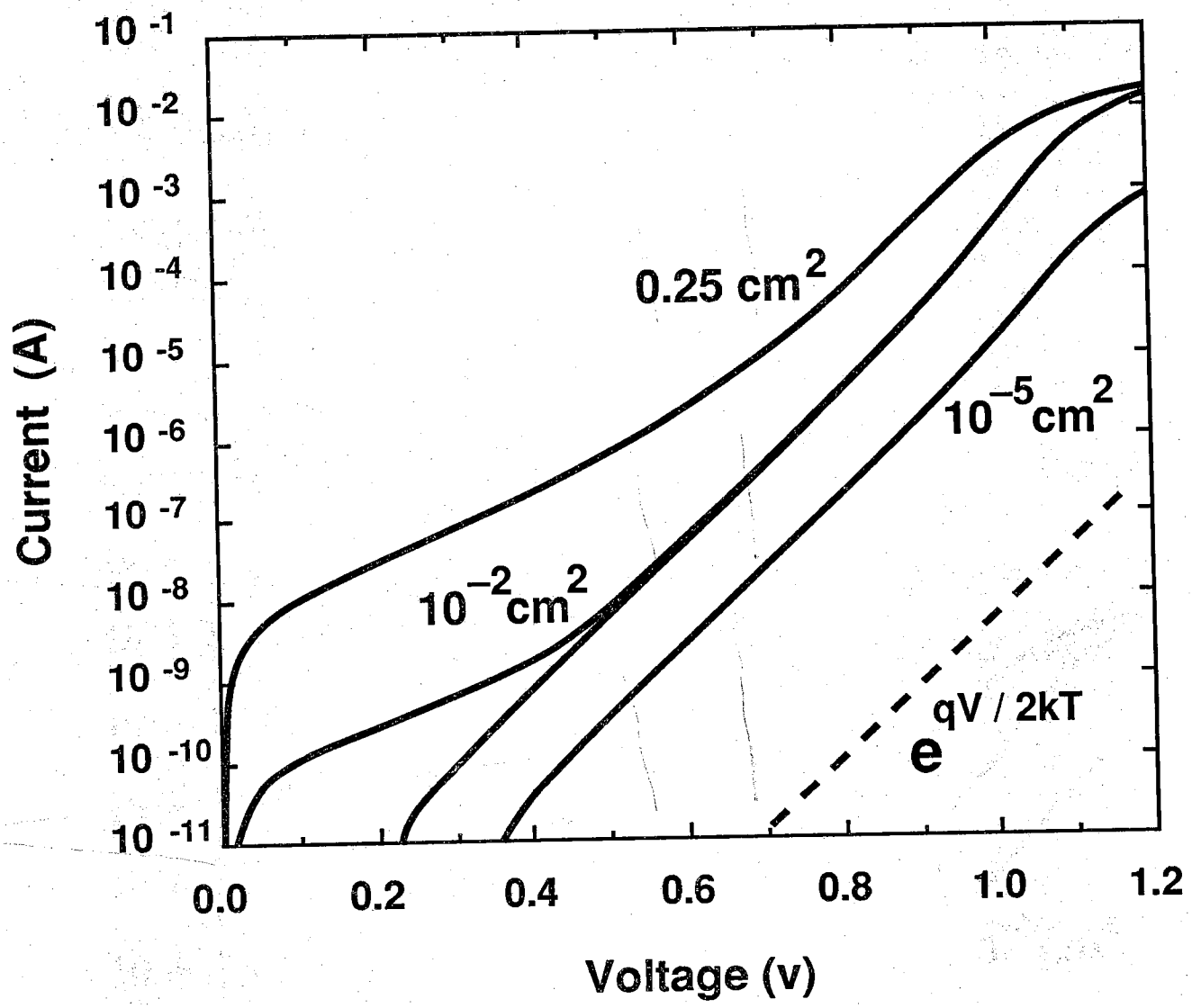

Fig. 3.2 Comparison of current-voltage characteristics for different area GaAs diodes.

Table 3.4 Correlation between diode area and leakage currents.

diode area (cm^2)	number of diodes tested	number of diodes exhibiting leakage currents	average number of oval defects
0.25	20	20	125
0.01	24	12	5
2.5×10^{-3}	24	6	1.25
1×10^{-4}	24	2	0.05

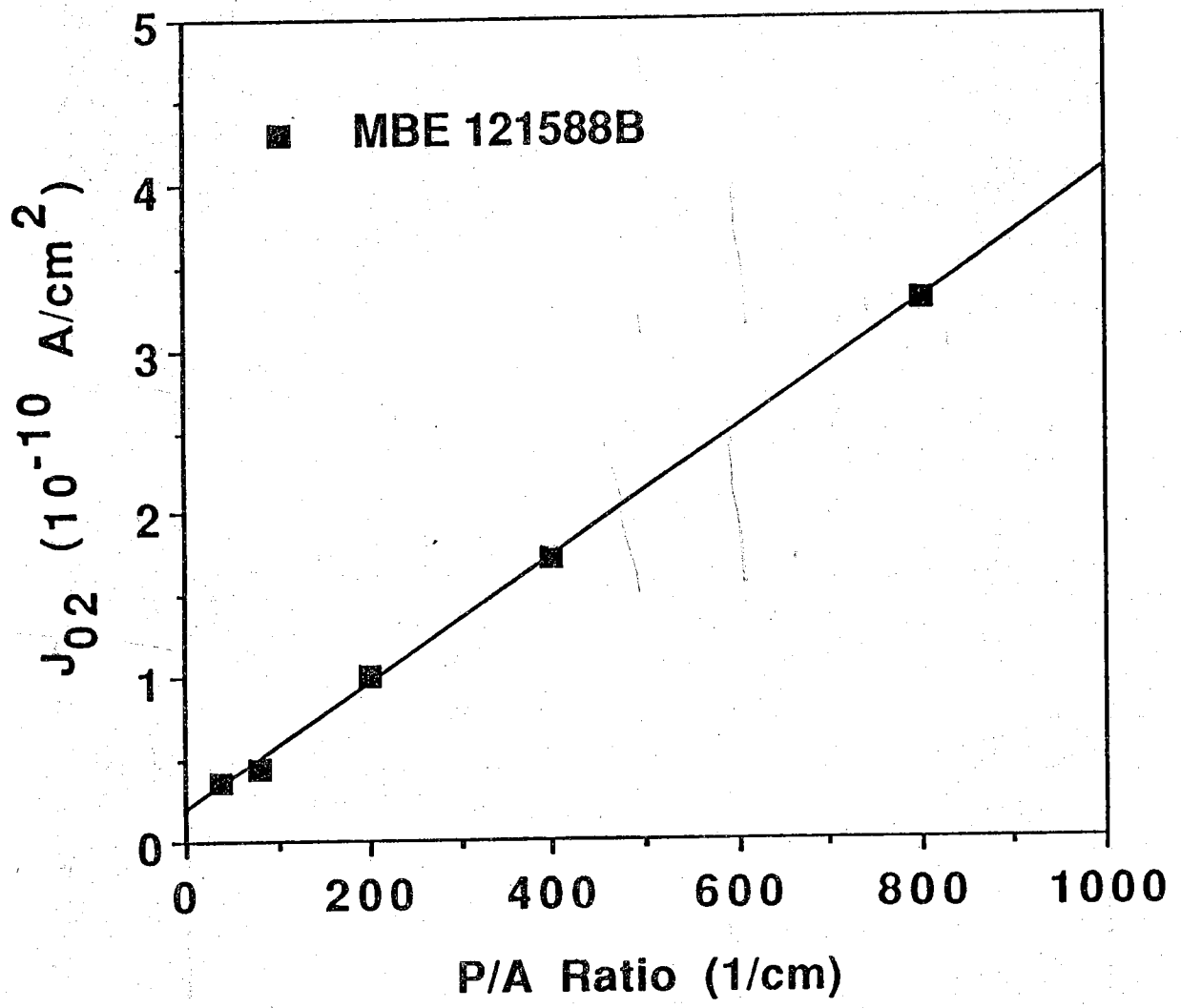

Fig. 3.3 Plot of extracted J_{o2} versus perimeter-to-area ratio for MBE-grown GaAs diodes.

[15]. The fact that the bulk q/2kT component is so small for our MBE-grown diodes indicates high space-charge-recombination lifetimes.

3.5 SUMMARY

We have obtained 1-sun AM1.5 efficiencies of 23.8% for 0.25 cm^2 GaAs solar cells fabricated on MBE-grown material. This is the first solar cell fabricated on MBE-material which is of comparable performance to solar cells fabricated on MOCVD-grown material. The major efficiency limiting mechanism of our MBE solar cells are leakage currents at low current levels which reduce the fill factors (FF) of the cells. These leakage currents are due to isolated defects and appear to correlate with the oval defects in the film. The oval defect density of the film was 500 cm^{-2} which can be reduced significantly in the future [16-17] and should result in even higher MBE-grown solar cell efficiencies.

CHAPTER 3 REFERENCES

[1] S.P. Tobin and S.M. Vernon, *Technical Digest of the 4th International Photovoltaic Science and Engineering Conference*, Sydney, Australia, February 14-17, 1989.

[2] K. Burkess, M. Ladle, and H.C. Hamaker, *Conference Record of the 20th IEEE Photovoltaic Specialists Conference*, Las Vegas, Nevada, September 1988.

[3] R.P. Gale, R.W. McClelland, B.D. King, and J.V. Gormley, *Conference Record of the 20th IEEE Photovoltaic Specialists Conference,* Las Vegas, Nevada, September 1988.

[4] S.P. Tobin, S.M. Vernon, C. Bajgar, S.J. Wojtczuk, M.R. Melloch, A. Keshavarzi, T.B. Stellwag, S. Venkatensan, M.S. Lundstrom, and K.A. Emery, to appear in *IEEE Transactions on Electron Devices*, February 1990.

[5] John C.C. Fan, A.R. Calawa, Ralph L. Chapman, and George W. Turner, *Appl. Phys. Lett.* **35**, 804(1979).

[6] D.L. Miller and J.S. Harris, Jr., *Appl. Phys. Lett.*, **33**, 1104(1981).

[7] Chikara Amano, Masafumi Yamaguchi and Atsushi Shibukawa, *Technical Digest of the International PVSEC-1*, Kobe Japan, 845(1984).

[8] A. Saletes, J.P. Contour, M. Leroux, J. Massies, N. Defranould, and G. Pelous, *Solar Cells*, **17**, 373(1986).

[9] M.R. Melloch, D.C. Miller, and B. Das, *Appl. Phys. Lett.*, **54**, 943(1989).

[10] J.H. Neave, B.A. Joyce, P.J. Dobson, and N. Norton, *Appl. Phys. A*, **31**, 1(1983).

[11] T.J. Drummond, J. Klem, D. Arnold, R. Fischer, R.E. Thorne, W.G. Lyons, and H. Morkoc, *Appl. Phys. Lett.*, **42**, 615(1983).

[12] K.L. Tan, M.S. Lundstrom, and M.R. Melloch, *Appl. Phys. Lett.*, **48**, 428(1986).

[13] S.P. Tobin, S.M. Vernon, C. Bajgar, L.M. Geoffroy, C.J. Keavney, M.M. Sanfacon, and V.E. Haven, *Solar Cells*, **24**, 103(1988).

[14] S. P. Tobin, M.B. Spitzer, C. Bajgar, L. Geoffroy, and C.J. Keavney, *Conference Record of the 19th IEEE Photovoltaics Specialists Conference*, pp. 70-75, 1987.

[15] P.D. DeMoulin, S.P. Tobin, M.S. Lundstrom, M.S. Carpenter, and M.R. Melloch, *IEEE Elec. Dev. Lett.*, **EDL-9**, 368(1988).

[16] S-L. Weng, C. Webb, Y.G. Chai, and S.G. Bandy, *Appl. Phys. Lett.*, **47**, 391(1985).

[17] A. Salokatve, J. Varrio, J. Lammasniemi, H. Asonen, and M. Pessa, *Appl. Phys. Lett.*, **51**, 1340(1987).

CHAPTER 4

PHOTOVOLTAIC CHARACTERIZATION OF $Al_{0.2}Ga_{0.8}As$ SOLAR CELLS

4.1 INTRODUCTION

The ternary semiconductor $Al_xGa_{1-x}As$ is being widely-studied as a material for the top cell in tandem cell applications [1-5]. To optimize $Al_xGa_{1-x}As$ cell efficiency, a detailed understanding of recombination losses and their relation to material quality and cell design is required. In this chapter we compare the material properties of two $Al_{0.2}Ga_{0.8}As$ films, one grown by molecular beam epitaxy (MBE), the other by metalorganic chemical vapor deposition (MOCVD). The objective is to quantify recombination losses, relate them to material parameters, project cell performance achievable with present-day material, and, finally, to prioritize the research problems that need to be addressed in order to maximize $Al_xGa_{1-x}As$ cell performance.

4.2 FILM GROWTH AND DEVICE PROCESSING

The MBE AlGaAs layers were grown on a two inch n^+ liquid encapsulated Czochralski (LEC) substrate in a Varian GEN II MBE system at Purdue University. The source materials consisted of elemental Ga, As, Al, Si, and Be. AlGaAs layers were grown at an elevated temperature of $\simeq 675°C$ to reduce the nonradiative mid-gap trap, ME6, [6], while the GaAs buffer and cap layers where grown at 600°C (the oxide desorption temperature was 580°C). Reflection high energy electron diffraction patterns were used to determine the growth rates and monitor the growth conditions. The measured growth rates were one micrometer per hour for both the AlGaAs and the GaAs layers. To retain high bandgap and doping uniformity, the wafer was rotated at five revolutions per minute.

The MOCVD film was grown on an n^+ horizontal Bridgman substrate in a SPI-MO CVD™ 450 epitaxial reactor at the Spire Corporation. The reactor is a vertical-geometry, barrel-type operating at atmospheric pressure. Trimethylgallium, trimethylaluminum, and arsine were the source gases, with silane and dimethylzinc diluted in hydrogen used for n- and p-type dopants. The active layers were grown at 800°C with a 20:1 group V-III flow ratio. The temperature was lowered to 700°C during the growth of the cap layer to assure a high p^+ doping for low-resistance, non-alloyed p-type contacts.

Because the objective of this work was the diagnostic evaluation of material quality and identification of recombination losses, no attempt to fabricate high-efficiency cells was undertaken. Rather, a variety of test structures was fabricated. By processing the MBE- and MOCVD-grown films together, the effects of processing variations were minimized. Two different processing runs with two different mask sets were completed. The first run produced diodes with areas ranging from 2.5×10^{-5} cm^2 to 0.01 cm^2 and perimeter to area ratios from 40 to 600 cm^{-1}. Solar cells for internal quantum efficiency measurements were produced in the second fabrication run. Both diodes and solar cells were processed using standard photolithography, lift-off, and mesa etching techniques. For the solar cells, a selective etch was used to remove the GaAs cap, and SiO_2 was deposited to passivate the exposed window surface and act an a non-optimized antireflection coating. (Later, it was found that the etch attacked the high Al content window, so all cells suffered from a high front surface recombination velocity.)

4.3 DEVICE CHARACTERIZATION

A variety of measurements was undertaken in order to characterize the AlGaAs material and to quantify recombination losses. Although the MBE and MOCVD films were targeted to be identical, differences invariably occurred in the Al content and layer dopings. The doping profile of the MBE-grown film was measured by electrochemical and junction C-V profiling, and the results are displayed in Fig. 4.1a. Electrochemical profiling was unsuccessful for the MOCVD-grown film, but the measured slope of the reverse-biased $1/C^2$ vs. voltage characteristic was consistent with the targeted dopings displayed in Fig. 4.1b.

Room temperature photoluminescence (PL) was used to determine the Al content of the films. The PL intensity was measured using a 514.5 nm Ar^+ laser with a power density of 1.0 W/cm^2. To avoid intensity shifts due to different doping levels and dopant types, the cells were etched to expose the AlGaAs base. The results shown in Fig. 4.2, therefore, represent the n-type AlGaAs. The Al content was determined from the peak in the PL intensity using the room temperature band gap versus mole fraction formulae as given by Casey and Panish [8]. A mole fraction of 0.18 was deduced for the MOCVD-grown material and 0.22 for the MBE-grown film. Previous work on PL wafer mapping showed that a mole fraction variation of about 0.02 across a wafer is typical for these MOCVD-grown films [5]. It was also noted that the intensity of the PL emission was more than a factor of two lower for the MBE-grown film, which suggests that its minority carrier lifetime was somewhat lower than that of the MOCVD-grown film.

The forward-biased dark current-density versus voltage characteristics were measured using a HP 4145 semiconductor parameter analyzer. Fig. 4.3 displays the measured characteristics for small (1.0×10^{-4} cm^2) and large (0.25 cm^2) area diodes. The smaller cells display a linear slope of q/2kT which indicates that their dark current in this range is dominated by recombination in space-charge regions. The larger MOCVD cells behave much like the small MOCVD cells, but

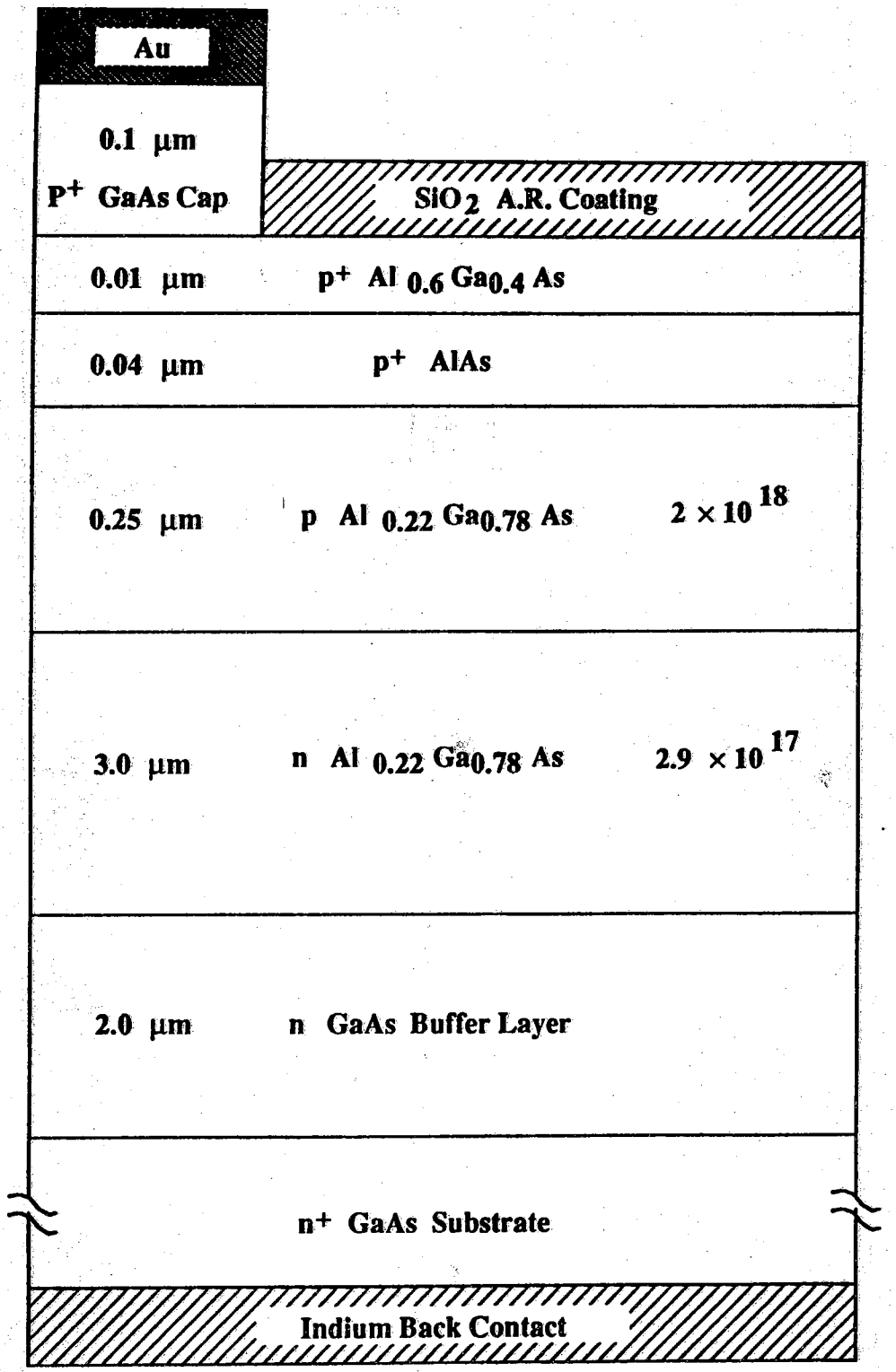

Fig. 4.1a Device structure for diodes fabricated on MBE-grown films.

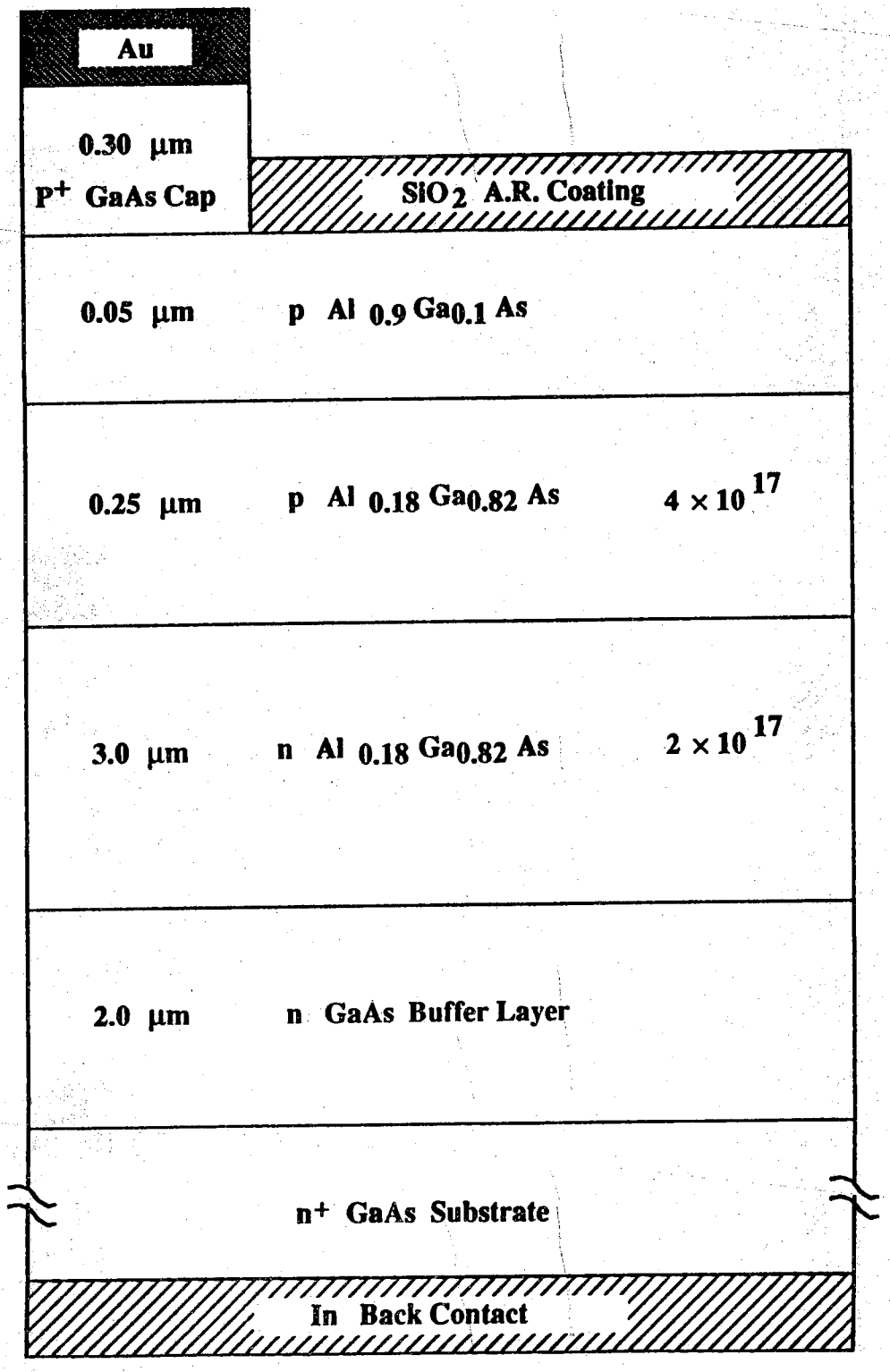

Fig. 4.1b Device structure for diodes fabricated in MOCVD-grown films.

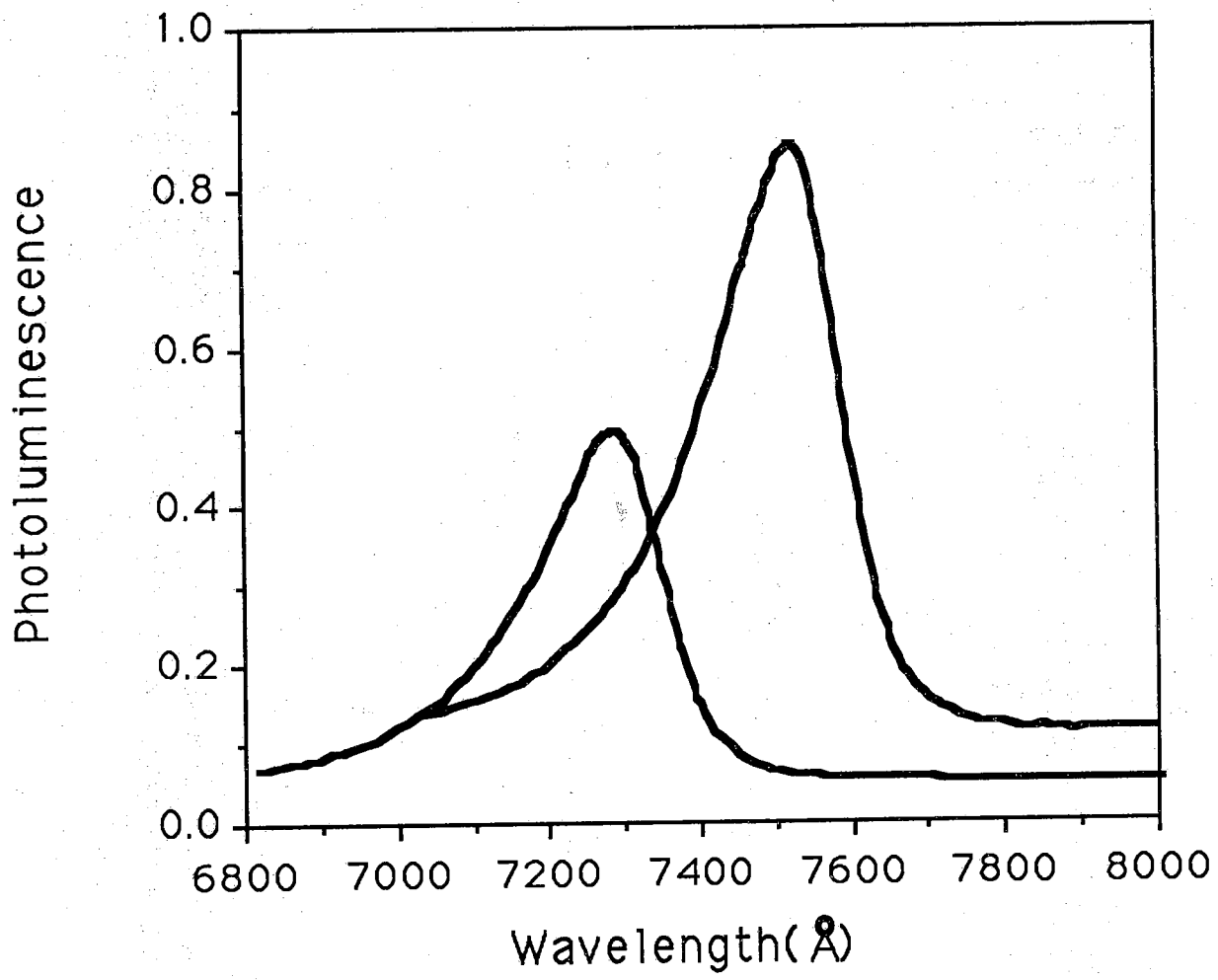

Fig. 4.2 Comparison of room temperature photoluminescence spectra of MBE-grown and MOCVD-grown n-type $Al_{0.2}Ga_{0.8}As$ films. The peak PL emission intensity is more than a factor of 2 lower for MBE-grown film.

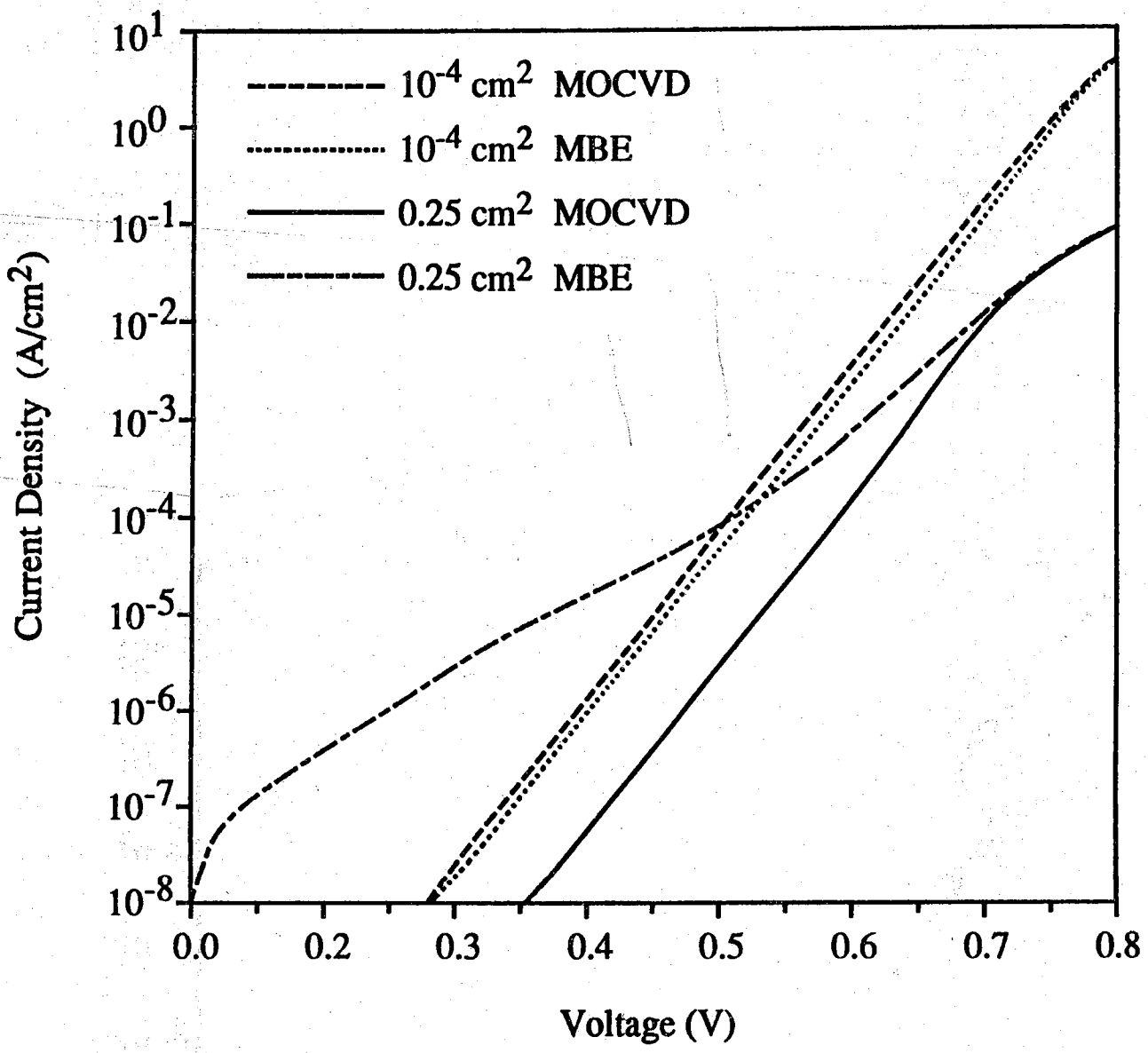

Fig. 4.3 Dark I-V characteristic at 25°C for small and large area diodes. Small diodes have an area of 1.0×10^{-4} cm^2; the large ones have an area of 0.25 cm^2. For the MOCVD diodes, the results displayed are the lowest measured currents of 15 diodes, and for the MBE film they are the lowest currents from 13 diodes. (The highest currents were about 25% greater on the MOCVD diodes and about 30% higher on the MBE diodes.) Note the higher current density of smaller diodes due to perimeter recombination current.

a sizeable shunt leakage is observed in large area, MBE cells. The shunt leakage is thought to be related to bulk defects because it was observed with increasing frequency as the diode area increased.

A careful study of the MBE films reveals the existence of oval defects with density of 300 to 400 per cm^2. Such defects are not present on the MOCVD-grown films. Their size ranges from 1 to 20 μm. Oval defects can have their origins in particulates and other contaminants on the surface of the starting substrate prior to the growth and/or defects introduced during the growth by the MBE system [15]. The presence of oval defects has been shown to increase p-n junction leakage currents [11, 16]. Common sources of leakage current include edges (junction perimeter), metal spiking through the p/n junction, and defects, which can produce defect-assisted tunneling or shunt conduction paths. Both MBE and MOCVD films had the same structure and were processed simultaneously, so edge leakage and metal spiking, which are sensitive to device fabrication, are unlikely to be the source of the leakage. This suggests that the $n > 2$ shunt leakage current is caused by oval defects or some other inherent defects in MBE-grown AlGaAs. Similar effects have also been observed in MBE-grown GaAs solar cells, but the leakage is typically small at the operating voltage [11]. (Although the leakage did reduce the fill factor somewhat, 1-sun AM1.5 conversion efficiencies of 23.8% for 0.5 cm by 0.5 cm GaAs solar cells were still achieved [11].) To maximize cell efficiency for MBE-grown films, however, the cause of the leakage current will need to be identified and its magnitude reduced because the shunt $n > 2$ leakage current will limit the fill factor and will cause a small open circuit voltage loss.

The time at which oval defects are formed during film growth can also be crucial in determining the magnitude of the leakage current [16]. Poor quality and leakage may be observed for solar cells and diodes where a defect is formed before p/n junction formation, whereas, oval defects formed near the surface do not seriously affect diode properties. The logorithmic plot of the dark current versus voltage measured at 26.5°C of various 0.01 cm^2 solar cells containing different number of oval defects is shown in Fig. 4.4. There are four dark I-V curves representing cells containing zero, one, two, and three particulate type oval defects from bottom to top. This figure demonstrates that there is no one-to-one correlation between the number of oval defects present on a device and the magnitude of the observed leakage current. But the data do suggest that the leakage increases as the number of oval defects increases. Electrically inactive oval defects and their time of formation may be the cause of this phenomena. The dark I-V of a relatively low leakage 0.01 cm^2 solar cell without any oval defects is shown in the bottom curve of Fig. 4.4. The small magnitude of the shunt leakage in this cell as compared to the much larger leakage current of the cells containing oval defects suggests that although other defects are present in AlGaAs material, they don't seem to contribute significantly to the observed leakage in the MBE films. It is still necessary to investigate the electrically active defects present in our films using an infra-red microscope or electron induced beam current in an SEM. Such measurements should enable us to relate the the magnitude of the shunt leakage to the number of electrically active oval defects.

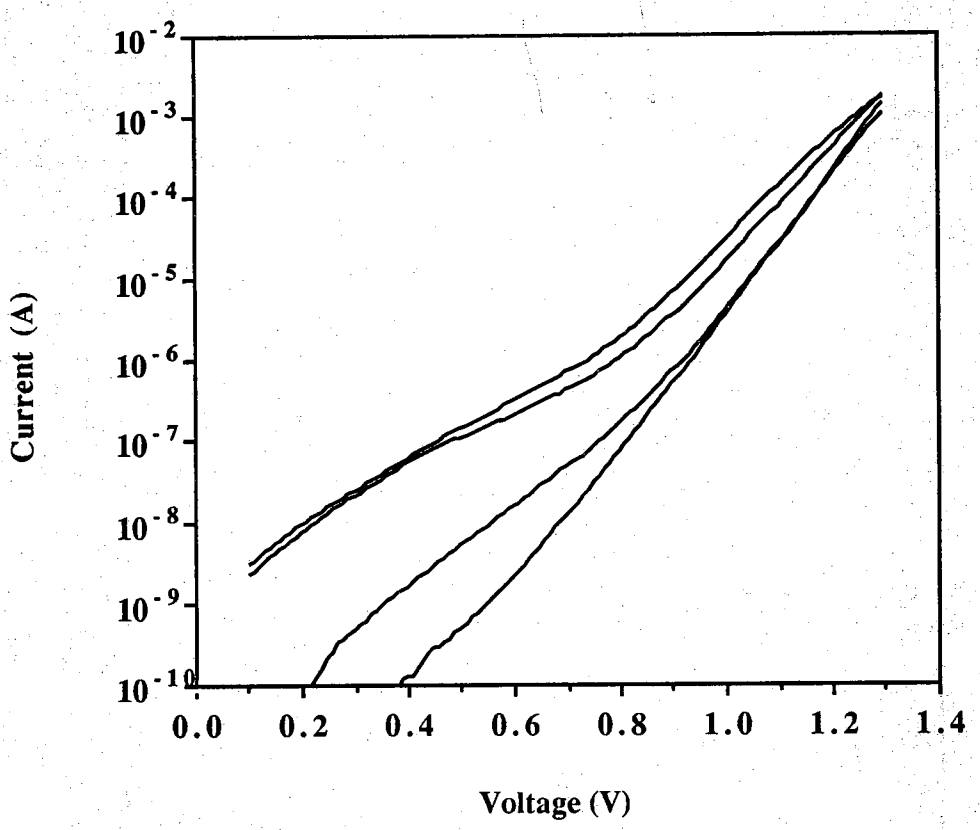

Fig. 4.4 Dark I-V characteristic at 26.5°C of 0.01 cm^2 MBE-grown $Al_{0.2}Ga_{0.8}As$ solar cells used for oval defects study. The oval defects counted are mainly the type due to particulate contaminants prior to the growth having density of 300 to 400 per cm^2. The leakage current increases as the number of oval defects increases. Four plots represent dark I-V of 0.01 cm^2 cells containing zero, one, two, and three oval defects in order from bottom to top. The region of interest is at low voltage bias and the magnitude of shunt leakage does not vary linearly with the number of oval defects. Current axis is logarithmic and the only conclusion is that the leakage current will increase as the frequency of defects increases. Note that the cell without any oval defects is still a little bit leaky.

At Purdue, the oval defects are mainly attributed to the substrate cleanliness and preparation. The wafers are cleaned in a different building than the one containing the MBE system. Although as much care as possible is taken to maintain a clean substrate, particulates have a good chance of being present on the starting substrate. Oval defect densities should be greatly reduced in the near future when class 100 cleanroom conditions are employed for preparing the substrates.

It is also interesting to note that the small area diodes display a higher current density (defined simply as the measured current divided by the diode area) than do the larger diodes as displayed in Fig. 4.3. This result suggests that the n = 2 current component is comprised of components from both the bulk and perimeter space-charge regions. The n = 2 saturation current density can be written as

$$J_{o2} = J_{o2p}\frac{P}{A} + J_{o2b} \tag{4.1}$$

where J_{o2b} (units= A/cm^2) is the bulk component and J_{o2p} (A/cm) is the perimeter component. The saturation current density, J_{o2}, was extracted from the measured J-V characteristic by least squares curve fitting. When the extracted J_{o2} is plotted versus P/A as displayed in Fig. 4.5, both the perimeter and bulk current components can be determined. When the results of Fig. 4.5 are scaled to a 0.5 cm × 0.5 cm cell, we find that bulk and perimeter recombination contribute about equally to the n = 2 current component. By contrast, similar sized GaAs cells were observed to be dominated by perimeter recombination [12]. These observations suggest that the bulk lifetimes in AlGaAs films are somewhat lower than they are in high-quality GaAs.

Recombination losses under illuminated conditions were probed by performing internal quantum efficiency (QE) measurements on both MBE and MOCVD cells. Because emitters are typically thinner than a minority carrier diffusion length, it is generally impossible to extract the front surface recombination velocity and emitter diffusion lengths independently from such measurements. Moreover, due to the processing problems encountered during cap removal, very high front surface recombination velocities resulted. The base layers, however, were thicker than a diffusion length, so it was possible to extract the base diffusion length with confidence. For the MOCVD-grown film, a base diffusion length of $L_p = 1.5$ μm was obtained, and for the MBE-grown film we found $L_p = 0.8$ μm. Assuming similar diffusion coefficients for the two films, these results suggest that the minority carrier hole lifetime in the n-AlGaAs films grown by MOCVD is roughly 3-4 times higher than the lifetime in the MBE-grown film. The internal QE measurements are consistent with the PL measurements which showed a factor of 2.4 larger signal for the MOCVD-grown film.

To relate the photoluminescence and internal quantum efficiency measurements to material quality, deep level transient spectroscopy (DLTS) measurements were made on 2.22×10^{-3} cm^2

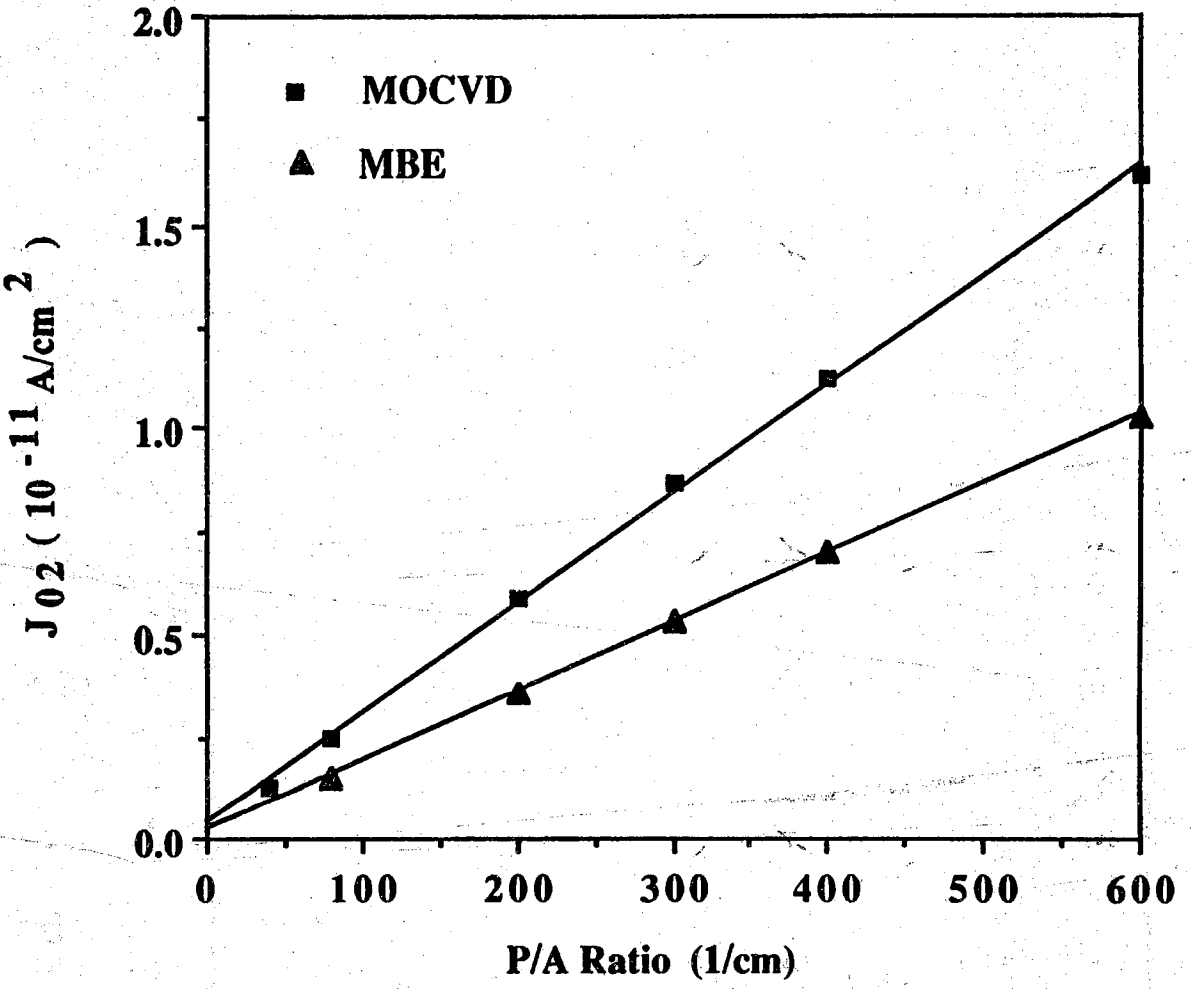

Fig. 4.5 Plot of J_{o2} versus perimeter to area ratio, P/A. The slope and intercept are perimeter and bulk components respectively of n=2 current. These measurements are from the same die used for the J-V measurements displayed in Fig. 4.3.

diodes from each film. Deep levels were observed in both films as show in Fig. 4.6. The trap parameters are summarized in Tables 4.1 and 4.2. The trap at 0.45 ± 0.01 eV below the conduction band edge, observed in both the MOCVD- and the MBE-grown films is identified as the donor-vacancy complex (DX) [6]. The concentration of DX centers in the MBE film is approximately eight times the concentration in the MOCVD material, which is consistent with its higher Al content.

A trap associated with a DLTS peak at approximately 370°K was also detected in both the MBE and the MOCVD films. This trap is characterized by an activation energy of 0.66 eV; its capture cross-section, σ_n, and concentration, N_T, are detailed in Tables 4.1 and 4.2. Previous investigations of AlGaAs films (grown by both MBE and MOCVD techniques) have detected the presence of a similar trap [6,9]. Comprehensive studies of electron traps in MBE AlGaAs [6] have shown that the trap (identified as ME6 in the MBE literature) is highly sensitive to the growth conditions. Its presence in MBE films has been attributed to arsenic oxide originating from the arsenic source [6]. The origin of the trap in MOCVD films has not been conclusively identified, although investigators have suggested that it may be tied to an Al-O or an O-vacancy complex [9]. For MBE films, the concentration of ME6 increases with Al content and decreases as the substrate temperature increases. For our MBE-grown films, the concentration of ME6 was about 2.7 times higher than in the MOCVD-grown films.

Finally, the trap at $E_C - 0.79$ eV was observed only in the MOCVD material. This trap has been associated with native defects in the AlGaAs films and is commonly identified as EL2 [10]. Both EL2 and ME6 traps have been shown to function as non-radiative recombination centers [6,12]. As noted previously, the ME6 concentration in the MBE-grown film was greater than the combined ME6 and EL2 concentration in the MOCVD-grown film, while the PL emission intensity was more than a factor of two lower in the MBE film. The base diffusion length extracted from the internal QE measurements was likewise shorter in the MBE solar cell than in the MOCVD solar cell. Both the PL and internal QE measurements are, therefore, consistent with the higher trap concentrations observed in the MBE-grown films.

4.4 DISCUSSION

In order to assess the quality of these films for high-efficiency solar cell applications, it is of interest to project achievable efficiencies using the measured and estimated material parameters. For these projections, we assumed that the minority carrier electron lifetime in the p^+-emitter (which was not measured) was equal to the hole lifetimes observed in the n-base. Because high-quality AlGaAs/GaAs window layers with interface recombination velocities of less than 10^4 cm/sec are now regularly achieved [13], a front surface recombination velocity of 10^4 cm/sec was assumed. The n = 2 dark current was then evaluated assuming 0.5 cm × 0.5 cm cells along with the measured bulk and perimeter saturation current densities. Using well-known

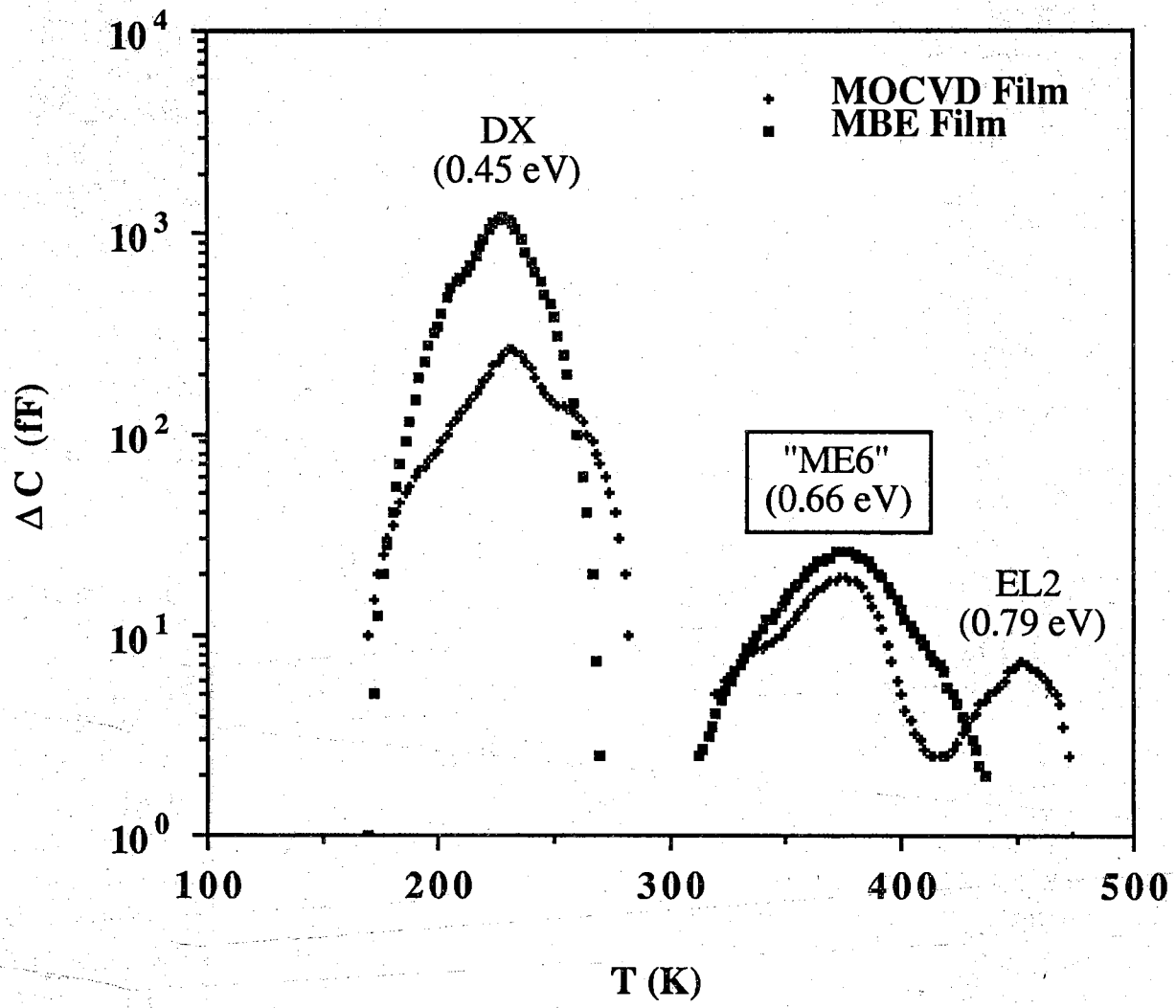

Fig. 4.6 Comparison of DLTS spectra of MBE-grown and MOCVD-grown n-type $Al_{0.2}Ga_{0.8}As$. All scans were performed at the window rate of 200 sec^{-1}.

Table 4.1

Summary of DLTS measurements on the MBE-grown film

Trap Parameters for MBE Film			
Trap	$\sigma_n(cm^2)$	$N_T(cm^{-3})$	$E_C - E_T(eV)$
DX	4.7×10^{-13}	2.9×10^{15}	0.45 ± 0.01
ME6	8.9×10^{-15}	7.2×10^{13}	0.66

Table 4.2

Summary of DLTS measurements on the MOCVD-grown film

Trap Parameters for MOCVD Film			
Trap	$\sigma_n(cm^2)$	$N_T(cm^{-3})$	$E_C - E_T(eV)$
DX	1.8×10^{-13}	3.7×10^{14}	0.45±0.01
ME6	9.1×10^{-15}	2.7×10^{13}	0.66
EL2	5.3×10^{-15}	6.0×10^{12}	0.79

solutions to the minority carrier diffusion equation, the n = 1 current component was projected from the cell structure, measured hole lifetime, and from the assumed electron lifetime and front surface recombination velocity. The internal QE versus wavelength was similarly projected using well-known expressions along with the measured and assumed material properties. The short-circuit current was obtained by multiplying the resulting internal QE versus wavelength by the incident flux of a standard AM1.5 global spectrum normalized to 100 mW/cm^2. Shadowing and reflection losses were not modeled. Finally, the light and dark currents were superimposed and the projected solar cell parameters computed.

Projections of solar cell performance are summarized in Tables 4.3 and 4.4. Projections for the MBE cell are somewhat lower than for the MOCVD cell primarily as a result of the lower bulk lifetimes observed in the MBE-grown films. (The shunt leakage observed in the large area MBE cells was not modeled for these projections.) These projections should be realistic estimates of

the efficiencies achievable for $Al_{0.2}Ga_{0.8}As$ cells with present-day material quality. Films from the same MOCVD growth run were, in fact, previously fabricated into cells with optimized grid patterns and AR coatings [5]. Those cells displayed 1-sun conversion efficiencies of $\simeq 17\%$. The primary reason for the lower than expected conversion efficiency is thought to be due to high recombination velocity at the hetero-interface. Techniques now used for producing high-quality windows for GaAs cells [13], should be directly applicable to AlGaAs and should permit the achievement of the efficiencies projected in Table 4.4.

Table 4.3
Projected saturation current densities for MBE- and MOCVD-grown films

Saturation Current Densities			
Film	J_{o2p}(A/cm)	J_{o2b}(A/cm^2)	J_{o1}(A/cm^2)
MBE	1.7×10^{-14}	2.14×10^{-13}	4.1×10^{-24}
MOCVD	2.7×10^{-14}	4.2×10^{-13}	1.6×10^{-23}

Table 4.4
Projected solar cell performance for MBE- and MOCVD-grown films

Projected Solar Cell Output Parameters (1-sun, AM1.5)				
Film	V_{oc}(V)	J_{sc}(mA/cm$^{2)}$	FF	Eff.(%)
MBE	1.25	18.7	0.85	19.8
MOCVD	1.18	20.5	0.86	21.0

In order to improve solar cell performance, it is also necessary to identify the source(s) of the recombination losses under both short-circuit and open-circuit conditions. Table 4.5 shows how recombination in the bulk and perimeter space-charge regions contribute to the n = 2 losses and how recombination in the quasi-neutral emitter and base layers contribute to losses associated with the n = 1 current. As deduced from Table 4.5, recombination in the bulk and perimeter space-charge regions is a sizeable loss component for $Al_{0.2}Ga_{0.8}As$ cells under 1-sun conditions. For concentrator applications, V_{oc} would be limited by recombination in the quasi-neutral base.

Table 4.5
Distribution of recombination losses under open-circuit conditions

Dark Current Losses at $V=V_{oc}$ (1-sun, AM1.5)				
Film	J_{o2p}(%)	J_{o2b}(%)	J_{o1e}(%)	J_{o1b}(%)
MBE	27.0	42.7	1.9	28.3
MOCVD	10.6	20.9	1.4	67.1

The losses at J_{sc} represent the collection efficiency of each region of the device and these can be found using Hovel's equations [7] and the AM1.5 spectrum. Table 4.6 shows the recombination losses at short circuit in each region for both cells. Nearly 85% of the collection losses of each cell occur in the base, while little recombination occurs in the emitters. Although the thin emitter aids collection in that region, it also means more carriers are generated in the base region where the short diffusion length prevents efficient collection.

Table 4.6
Distribution of recombination losses under short-circuit conditions

Recombination Losses at $J=J_{sc}$ (1 sun, AM1.5)			
Film	Window	Emitter	Base
MBE	12%	2%	86%
MOCVD	14%	2%	84%

4.5 CONCLUSIONS AND FUTURE DIRECTIONS

We have measured, analyzed, and characterized $Al_{0.2}Ga_{0.8}As$ solar cells fabricated on films grown by MBE and MOCVD. DLTS measurements show that both MBE- and MOCVD-grown films possess DX centers and a trap labeled as ME6. In addition, the EL2 defect was observed in the MOCVD-grown film. The concentrations of ME6 in the two films, the PL intensities, and the long wavelength internal quantum efficiencies all display the same trend. The performance

of both MBE and MOCVD cells is adversely affected by low bulk lifetimes which increase the bulk component of J_{o2} and lower the internal quantum efficiency.

Further improvements in $Al_{0.2}Ga_{0.8}As$ cell efficiency will require improvements in both material quality and cell design. The concentration of ME6, a known recombination center, can be reduced by proper growth conditions [14]. The source of leakage in large area, MBE diodes must also be identified and suppressed. Finally, device design can also enhance cell performance. The use of n on p cells rather than the p on n cells considered here may prove beneficial for enhancing base diffusion lengths, and the application of doping or compositional variations may prove useful for improving collection efficiency.

Acknowledgement- The authors thank David Mathine for performing the photoluminescence measurements.

CHAPTER 4 REFERENCES

[1] G. F. Virshup, C. W. Ford, and J. G. Werthen, *Appl. Phys. Lett.*, 47 (1985) p. 1319.

[2] R. P. Gale, J. C. C. Fan, G. W. Turner, R. L. Chapman, and J. V. Pantano, *Appl. Phys. Lett.*, 44 (1984), p. 632.

[3] C. Amano, A. Shibukawa, and M. Yamaguchi, *J. Appl. Phys.*, 58 (1985), p. 2780.

[4] R. Zerdoum, L. Mayet, M. Gavand, and A. Laugier, *7th Eur. Com. Conf. on Photovoltaic Solar Energy,* Sevilla, 1986, Reidel, London, 1987, p. 938.

[5] S. M. Vernon, S. P. Tobin, and R. G. Wolfson, Final Subcontract Report, April 1984 - April 1986, (July 1987), Spire Corporation, SERI, U.S. Department of Energy, P. 2-15.

[6] K. Yamanaka, S. Naritsuka, K. Kanamoto, M. Mihara, and M. Ishii, *J. Appl. Phys.*, 61(11), (1987), pp. 5062-5068.

[7] H.J. Hovel and J.M. Woodall, *Proc. 10th IEEE Photovoltaic Spec. Conf.*, Palo Alto, CA, New York, (1973), p. 327.

[8] H. C. Casey, Jr. and M. B. Panish, *Heterostructure Lasers,* Academic Press, New York, 197, p. 193.

[9] P.K. Bhattacharya and S. Subramian, *J. Appl. Phys.*, 55(10), (1984), pp. 3664-3668.

[10] T. Matsumoto and P.K. Bhattacharya, *Appl. Phys. Lett.*, 41(7), (1982), pp. 662-664.

[11] S.P. Tobin, S.M. Vernon, C. Bajgar, S.J. Wojczuk, M.R. Melloch, A. Keshavarzi, T.B. Stellwag, S. Venkatesan, M.S. Lundstrom, and K.A. Emery, submitted for publication, (1989).

[12] P.D. DeMoulin, S.P. Tobin, M.S. Lundstrom, M.S. Carpenter, and M.R. Melloch, *IEEE Electron Dev. Lett.*, (9), (1988), pp. 368-370.

[13] S.P. Tobin, S.M. Vernon, C. Bajgar, L.M. Geoffroy, C.J. Keavney, M.M. Sanfacon, and V.E. Haven, *Solar Cells,* (24), (1988), pp. 103-115.

[14] K. Yamanaka, S. Naritsuka, M. Mannoh, T. Yuasa, Y. Nomura, M. Mihara, and M. Ishii, *J. Vac. Sci. Technolo. B,* (2), (1988), p. 229.

[15] A. Salokatve, J. Varrio, J. Lammasniemi, H. Asonen, and M. Pessa, *Appl. Phys. Lett.*, 51 (1987) p. 1340.

[16] N. Susa and H. Okamoto *Japanese J. Appl. Phys.*, 23 (1984), p. 317.

CHAPTER 5

ORIENTATION-DEPENDENT EDGE EFFECTS IN GaAs DIODES

5.1 INTRODUCTION

The performance of GaAs-based devices which contain pn junctions such as solar cells, heterojunction bipolar transistors (HBTs), and injection lasers can be significantly influenced by the mesa-etched edges which define the device geometry. The current of a mesa-isolated GaAs pn junction is comprised of components due to recombination in the bulk space-charge region, recombination within the space-charge region exposed at the perimeter of the mesa, and recombination in the bulk neutral regions. Therefore, the current-voltage characteristic of a GaAs pn junction is expected to have the form,

$$I = J_{O2B}A(e^{qV/2kT}-1) + J_{O2P}P(e^{qV/2kT}-1) + J_{O1}A(e^{qV/kT}-1) \qquad (5.1)$$

where J_{O2B} is the bulk saturation current component (A/cm^2), J_{O2P} is the perimeter component (A/cm), J_{O1} is the diffusion saturation current component (A/cm^2), A is the area of the diode and P is the perimeter. Henry et al. [1-4] found that the 2kT current was completely due to recombination at the exposssed perimeter of the mesa for double-heterostructure AlGaAs pn junctions with composition and doping levels similar to those used in injection lasers. Henry et al.'s [2,3] largest device was 125 μm x 500μm, however DeMoulin et al. [5] have shown that even in high efficiency GaAs solar cells as large as 2cm x 2cm the 2kT current is due to edge recombination. The influence of edge recombination on HBT performance was dramatically demonstrated by Sandroff et al. [6]; by passivating the periphery of an HBT with $Na_2S{\cdot}9H_2O$, Sandroff et al.[6] were able to get a 60-fold increase in the current gain of their devices. We have recently discovered an interesting aspect of the edge recombination current seen in GaAs pn junctions; there is a strong orientation-dependence to the edge recombination current. The results suggest that with proper device design, perimeter recombination losses might be substantially reduced. In this chapter we describe preliminary experiments which demonstrate this orientation-dependence.

5.2 DEVICE FABRICATION

The structure of Fig. 5.1 was grown in a Varian GEN II molecular beam epitaxy (MBE) system. This MBE system has recently produced record efficiency MBE-grown GaAs pn heteroface solar cells with a structure similar to Fig. 5.1 [7]. A two-inch liquid-encapsulated-Czochralski *<1 0 0>-oriented* substrate was used. The layers were grown at a substrate temperature of 600°C. Two gallium furnaces were used with each producing a flux corresponding to a growth rate of 0.5 μm/hr. The As_4 to total Ga beam equivalent pressures was 27 as measured with an ion-gauge in the substrate growth position. The superlattice (SL) layer consisted of 20 periods of 28

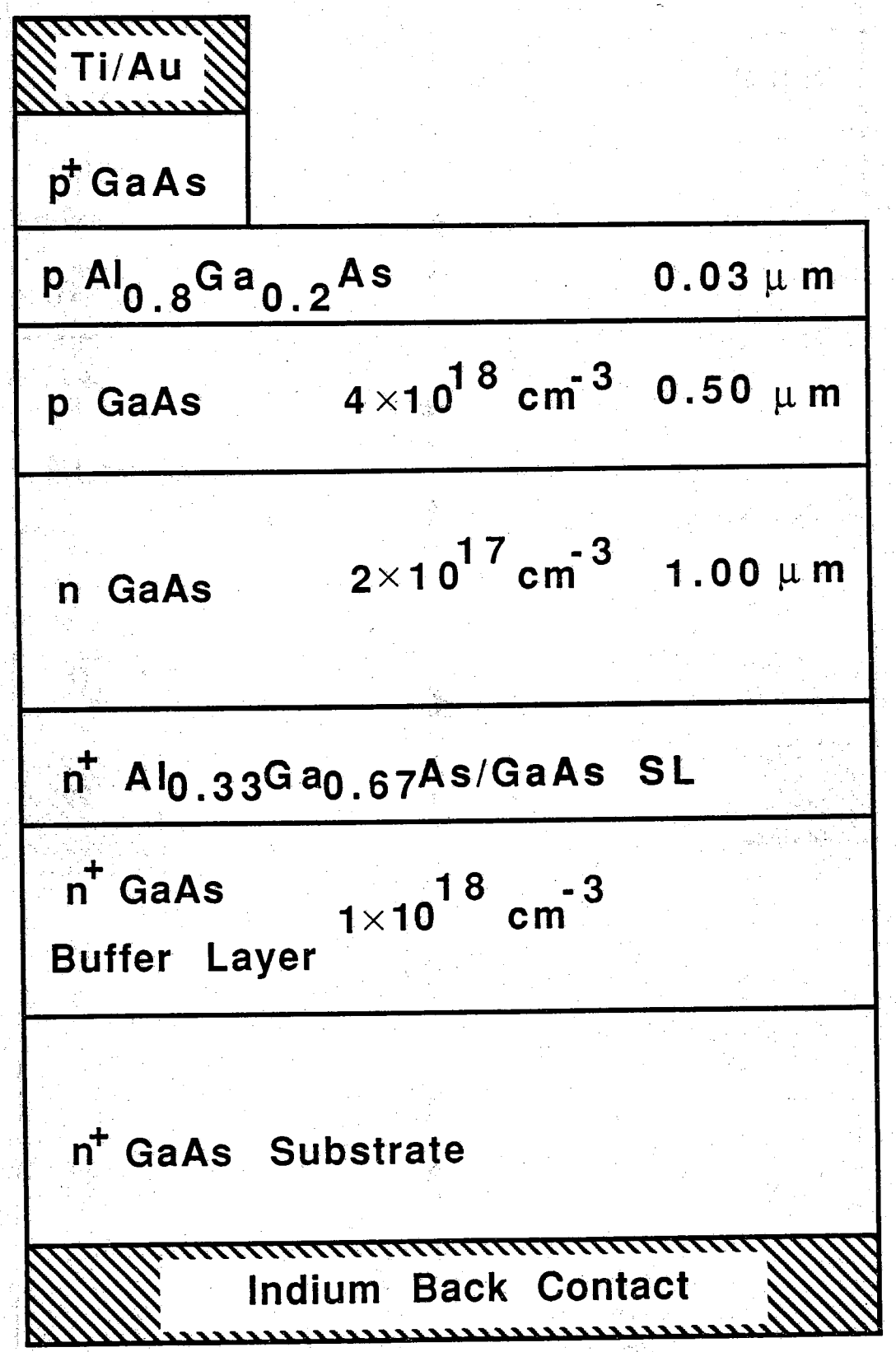

Fig. 5.1 Cross-section of MBE-grown diodes.

Å $Al_{0.33}Ga_{0.67}As$ barriers and 31 Å GaAs wells. (The SL was incorporated in the film structure to reduce any diffusion of impurities from the substrate into the growing film [8].)

A non-bonded wafer mount was used during the MBE growth, so following film growth a back ohmic contact was formed by alloying indium at 350°C for 1 min. Front metallization lift-off patterns were then defined, Ti/Au was Ebeam evaporated to form non-alloyed ohmic contacts, and the photoresist was disolved in acetone to remove excess metal. The mesas were then defined using conventional photolithography and etched in a 25° C methanol:H_2O_2:H_2O:H_3PO_4 3:1:1:1 solution for 1 min 15 sec. The etch rate was approximately two microns per minute, making this a suitable etch for mesa isolation.

The finished devices consisted of rectangular diodes with perimeter to area ratios varying from 60 to 480. In order to study the effects of orientation on the 2kT perimeter recombination current, this set of mesa-isolated diodes was rotated every forty-five degrees on the mask set with subsets rotated at fifteen degree increments.

5.3 EXPERIMENTAL RESULTS

The dark current versus voltage characteristics were measured as a function of orientation. We will define zero degrees as the orientation where the sides of length a of the rectangular diodes are along the $<0\,1\,\bar{1}>$–direction. Shown in Fig. 5.2 is the 2kT saturation current plotted versus angle of orientation for 70 µm x 500 µm rectangular diodes. This figure shows that the 2kT current is strongly dependent on the device orientation. Since the current due to the bulk space-charge region is independent of orientation, angle of rotation therefore affects the recombination at the perimeter. By properly orienting a device, this surface recombination current can be minimized.

Equation 5.1 assumed a constant J_{O2P} independent of orientation. For a rectangular diode of side lengths a and b, a more accurate description of the current voltage characteristic of a mesa-isolated GaAs pn junction is therefore,

$$I = J_{O2B}A(e^{qv/2kT}-1) + J_{O2Pa}2a(e^{qv/2kT}-1) + J_{O2Pb}2b(e^{qv/2kT}-1) + J_{O1}A(e^{qv/2kT}-1) \quad (5.2)$$

where J_{O2Pa} is the perimeter component along the sides of length a and J_{O2Pb} is the perimeter component along the sides of length b in A/cm.

From equation 5.2 we can write the q/2kT saturation current as

$$I_{O2} = J_{O2B}ab + J_{O2Pa}2a + J_{O2Pb}2b \quad (5.3)$$

where the area A was replaced by the product of the sides of the rectangular diode, ab. By plotting I_{O2}/ab versus P/A ratio for a series of diodes where a is held constant but b is allowed to vary, the perimeter component along the side of length a, J_{O2Pa}, can be determined from the

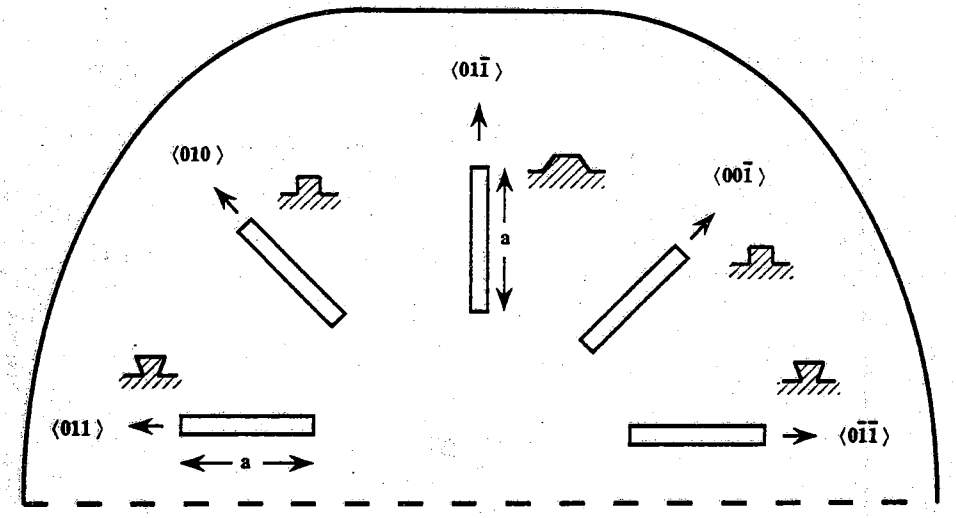

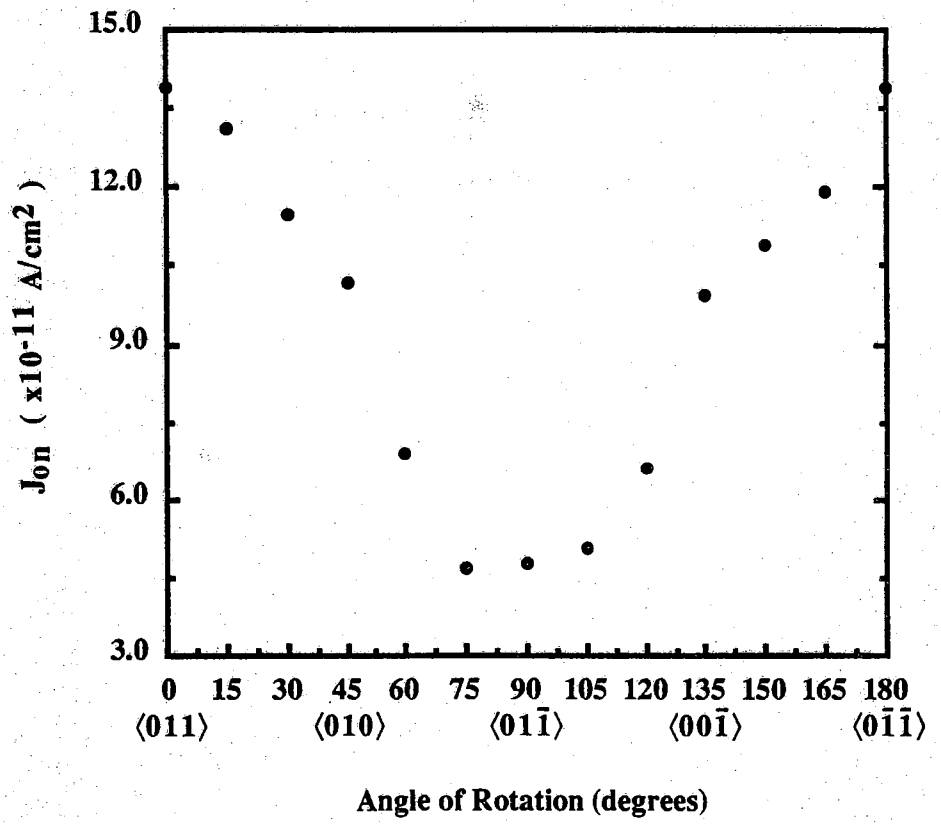

Fig. 5.2 Extracted J_{O2} as a function of diode orientation.

slope of the plot. In Figs. 5.3 and 5.4, plots of I_{O2}/ab versus P/A are shown for sets of diodes at 0, 45, 90, and 135 degrees. The plots for 45 and 135 degrees show that J_{O2Pa} is the same for edges along the <0 1 0>- or <0 0 1>-directions whereas the plot for 0 and 90 degrees exhibit a factor of four larger J_{O2Pa} for edges along the <0 1 $\bar{1}$>–direction as opposed to edges along the <0 1 1>-direction. Shown in Fig. 5.5a and 5.5b are scanning electron micrographs of the mesa edges along the <0 1 $\bar{1}$>– and <0 1 1>-directions respectively. The orientation dependent profiles seen in Fig. 5.5a and 5.5b are similar to those previously observed for GaAs mesas [9].

Following Henry et al. [4], the perimeter recombination current, J_{O2Pa} can be written as,

$$J_{O2Pa}=qn_iS_{SCR}L_s \tag{5.4}$$

where n_i is the intrinsic carrier concentration, S_{SCR} is the surface recombination velocity, and L_s is an effective surface diffusion length. We find that the $S_{SCR}L_s$ product ranges from 1.51 cm^2/s at 0 degrees to 0.3 cm^2/s at 90 degrees. This result suggests that the surface recombination velocity varies with orientation by a factor of 5. Though the J_{O2Pa} currents at 75 and 105 degrees are slightly less than at 90 degrees, the SL product for these orientations cannot be extracted due to the limited number of devices on the mask at these orientations.

5.4 SUMMARY

We have experimentally shown that the recombination current at the exposed edges of a GaAs pn junction has a strong orientation-dependence. There is also an orientation dependence to the profile of the etched mesa which is a function of the etch used [9]. Future work will involve an investigation of the effects of other mesa-isolation etches on the orientation dependence of edge recombination.

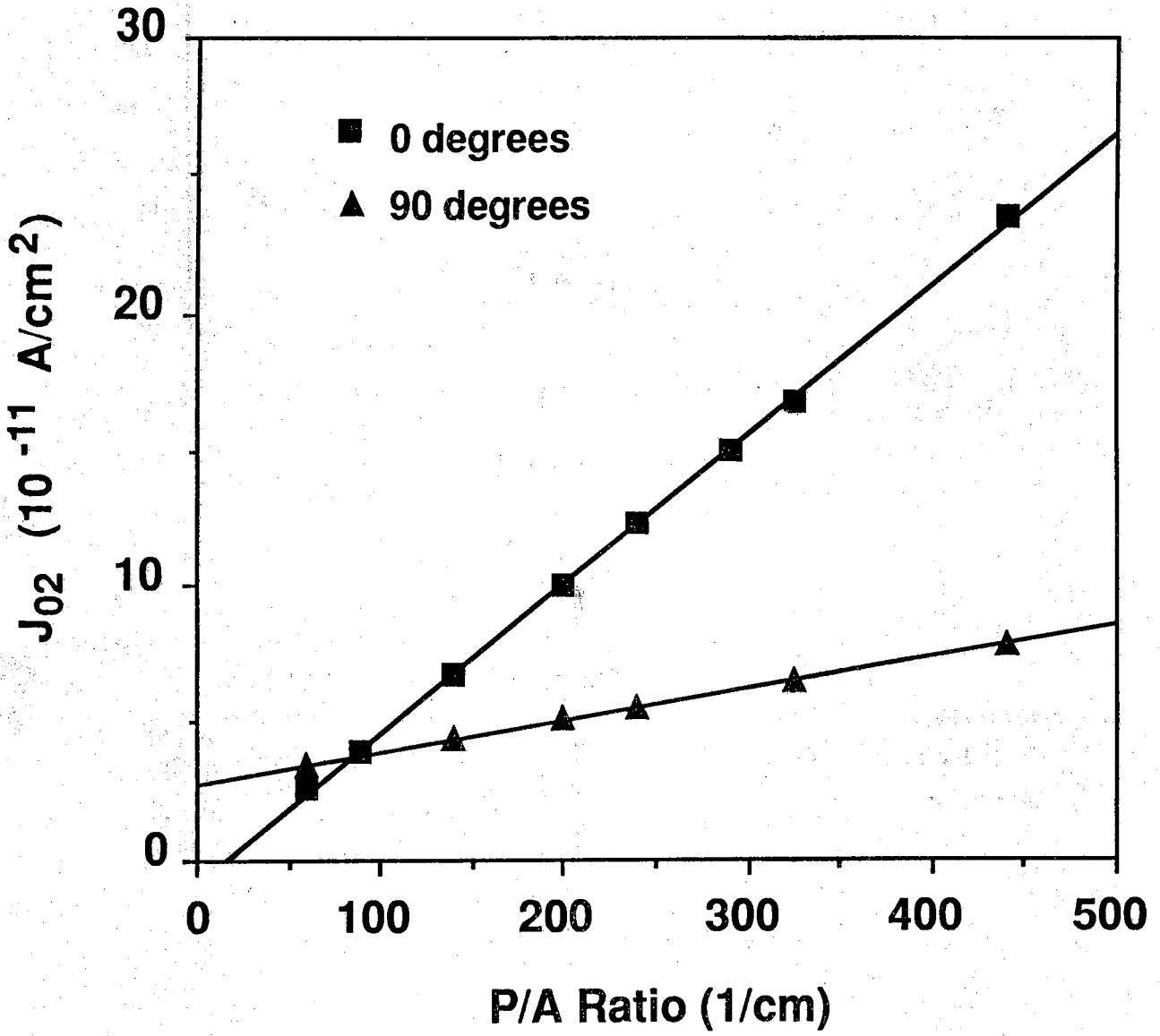

Fig. 5.3 Plot of extracted I_{O2}/ab versus perimeter-to-area ratio for a series of diodes where the side of length a is held constant while the side of length b is varied. 0 degrees signifies diodes where side a is along the <0 1 $\bar{1}$>-direction while 90 degrees signifies diodes where side a is along the <0 1 1>-direction.

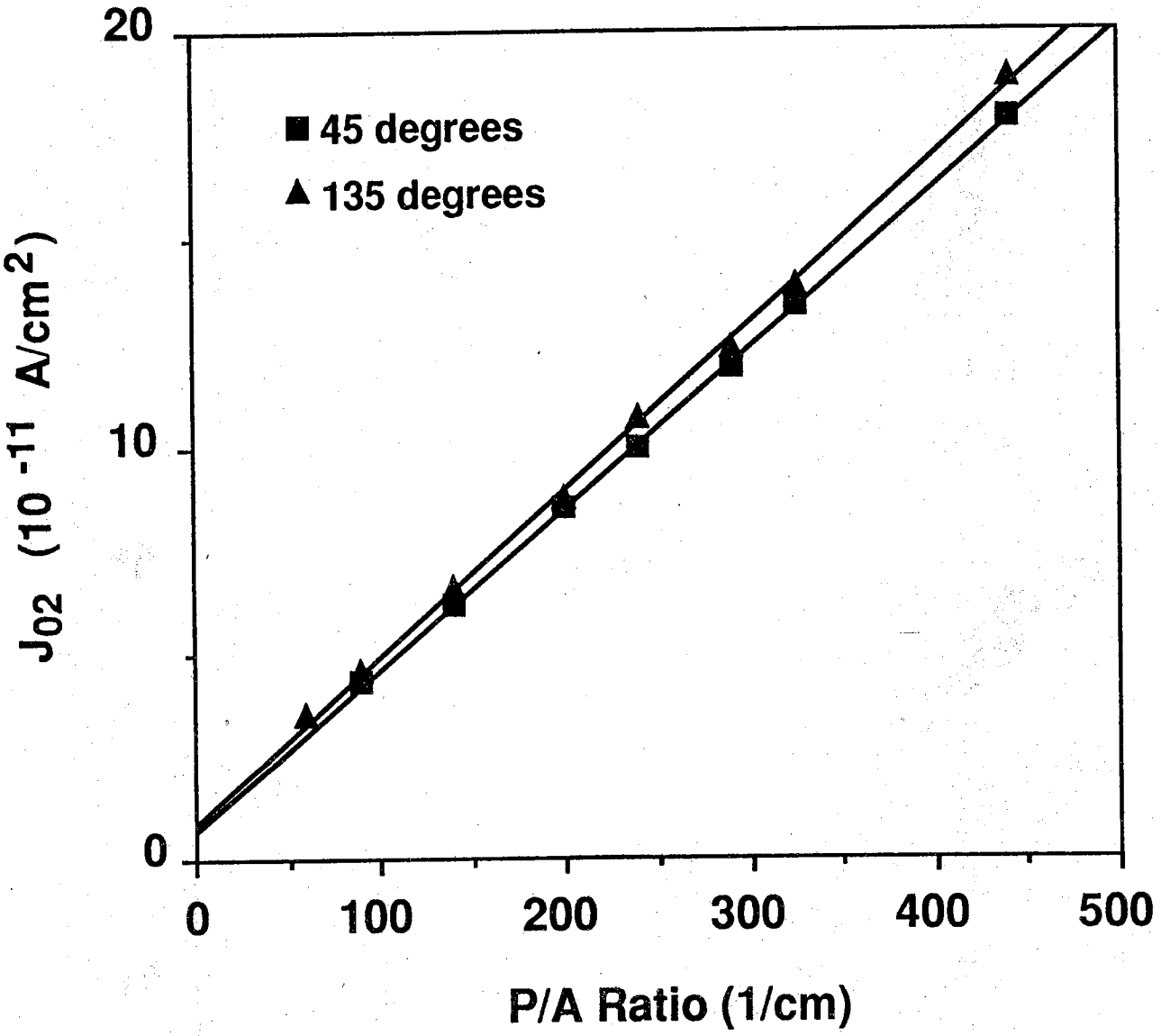

Fig. 5.4 Plot of extracted I_{02}/ab versus perimeter-to-area ratio for a series of diodes where the since of length a is held constant while the side of length b is varied. 45 degrees signifies diodes where side a is along the <0 1 0>-direction while 135 degrees signifies diodes where side a is along the <0 0 1>-direction.

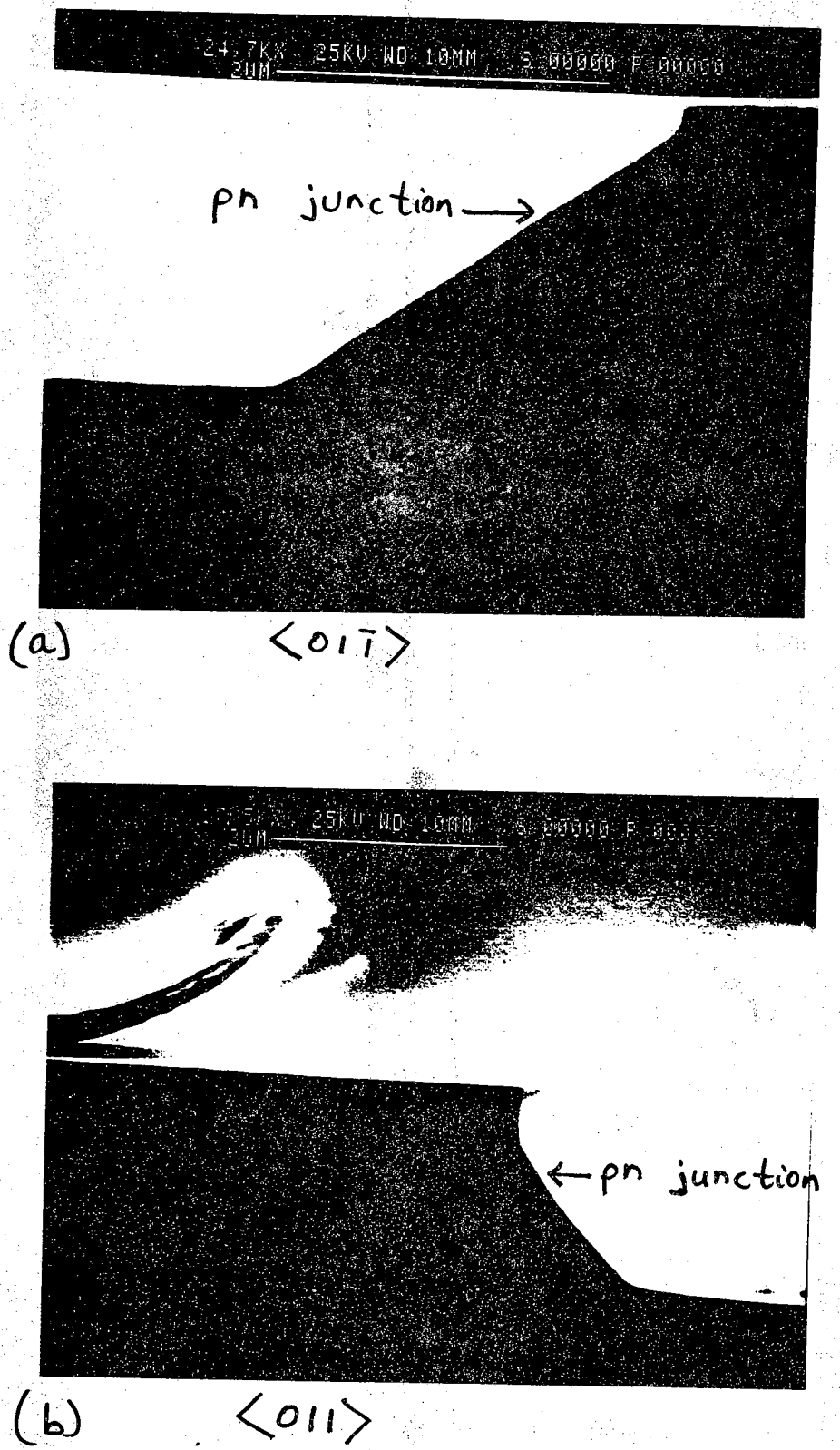

Fig. 5.5 Scanning electron micrographs of the mesa edges along the (a) <0 1 $\bar{1}$>- and (b) <0 1 1>-directions.

CHAPTER 5 REFERENCES

[1] C.H. Henry and R.A. Logan, J. Appl. Phys. 48, 3962(1977).

[2] C.H. Henry, R.A. Logan, and F.R. Merritt, Appl. Phys. Lett. 31, 454(1977).

[3] C.H. Henry, R.A. Logan, and F.R. Merritt, J. Appl. Phys. 49, 3530(1978).

[4] C.H. Henry and R.A. Logan, J. Vac. Sci. Technol. 15, 1471(1978).

[5] Paul D. DeMoulin, Stephen P. Tobin, Mark S. Lundstrom, M.S. Carpenter, and Michael R. Melloch, IEEE Elec. Dev. Lett. 9, 368(1988).

[6] C.J. Sandroff, R.N. Nottenburg, J.-C. Bischoff, and R. Bhat, Appl. Phys. Lett. 51, 33(1987).

[7] M.R. Melloch, S.P. Tobin, T.B. Stellwag, C. Bajgar, A. Keshavarzi, M.S. Lundstrom, and K. Emery, presented at the Tenth Molecular Beam Epitaxy Workshop, Raleigh, NC, September 13-15,1989, and submitted to the J. Vac. Sci. and Tech. B.

[8] K.L. Tan, M.S. Lundstrom, and M.R. Melloch, Appl. Phys. Lett. 48, 428(1986).

[9] S. Iida and K Ito, J. Electrochem. Soc. 119, 768(1971).

CHAPTER 6

CHEMICAL PASSIVATION OF GaAs SURFACES

6.1 INTRODUCTION

The oxides which form on GaAs result in a large density of surface states which can dominate the electrical behavior of devices. Even a brief exposure of a clean GaAs surface to oxygen can result in a pinning of the Fermi level at the surface. Recent sulfide chemical treatments of the GaAs surface have resulted in dramatic improvements in device performance [1-8]. Heterojunction bipolar transistor gains have been shown to increase 60-fold by treating the edges of the emitter base junction with $Na_2S \cdot 9H_2O$ [1,2]. Reduction in edge recombination currents have been observed by $Na_2S \cdot 9H_2O$ or ammonium sulfide treatment of GaAs pn homojunction solar cells [3]. A wider range of Schottky barrier heights has been observed in metal-GaAs Schottky barriers where the GaAs was treated with ammonium sulfide prior to thermal evaporation of the metal [4-6]. It has also been shown that the surface recombination velocity of sulfide treated GaAs approaches that of the nearly ideal AlGaAs/GaAs heterojunction [7,8]. It is therefore of great technical importance to determine the exact nature of the sulfide-treated GaAs surface. In last year's annual report we presented preliminary X-ray Photoelectron Spectroscopy (XPS) studies indicating that the ammonium sulfide treatment removes the oxides on the surface of GaAs, leaving behind a monolayer or less of sulfur which inhibits oxidation of the surface [9]. Sandroff et al. [19] have made similar observations. In this chapter we will present a more complete XPS study of the ammonium sulfide treated GaAs surface. The XPS measurements are being performed by Dr. B.A. Cowans and Dr. W.N. Delgass in the School of Chemical Engineering at Purdue University. Also, reflection high energy electron diffraction (RHEED) data on the ammonium sulfide treated GaAs surface will be presented. Finally, the effect of the ammonium sulfide treatment on the formation of gold and aluminum Schottky barriers on GaAs will be presented.

6.2 X-RAY PHOTOELECTRON SPECTROSCOPY

We previously examined the effects of oxidation on ammonium sulfide treated GaAs surfaces using XPS [10]. We found that the ammonium sulfide treatment produces a slightly Ga rich surface which is covered by less than one monolayer of sulfide. This surface condition is sufficient to severly restrict initial oxidation of the GaAs surface. The chemical state of the sulfur in the layer does not change with exposure to air although we do observe growth of a layer of oxidized gallium and arsenic over the sulfur. We have now used XPS to examine the effects of sulfide concentration on GaAs (100) surfaces using either saturated or unsaturated ammonium sulfide solutions. Ion sputtered and ammonium hydroxide etched GaAs surfaces were examined for comparison.

Samples were cut from undoped or Si-doped MaCom (100) GaAs wafers to roughly 16 mm x 20 mm and etched in 1:100 H_2SO_4:H_2O for 30 seconds followed by a 30 second deionized water rinse. Samples were then immediately etched with 1:1 NH_4OH:H_2O (pH >10) for 30 seconds or with saturated (pH >10) or unsaturated (pH >8) ammonium sulfide solutions for 20 minutes. Following either procedure, samples were rinsed with deionized water, dried and mounted under a stream of UHP argon, and loaded into the spectrometer. Prior to removing samples from a sulfide etch, the solution was diluted with an excess of deionized water. In a separate experiment, a "clean" surface was prepared in the spectrometer vacuum chamber by sputtering an acid etched wafer with 3kV Ar^+ ions for 5 minutes at a current density of approximately 230 $\mu A/cm.^2$ This procedure removes all carbon and oxygen impurities from the surface. Operating conditions of the Perkin-Elmer PHI 5300 spectrometer were described previously [10].

Photoelectron spectra of the As and Ga $2p_{3/2}$ core levels are shown in Fig. 6.1. The spectra shown are for (A) sputter cleaned, (B) unsaturated ammonium sulfide etched, (C) saturated ammonium sulfide etched, and (D) ammonium hydroxide etched surfaces taken at an electron take-off angle of 15 degrees from the surface plane. The presence of As(sulfide) is clearly observed for spectra (B) and (C) from the asymmetry of the line to higher binding energy. At an electron take off angle of 45 degrees, chosen to minimize effects of electron channeling [11], the relative As(sulfide)/As(GaAs) ratios are 0.169 for the saturated sulfide etch and 0.164 for the unsaturated etch. The binding energy shifts for Ga are less than those for As, but the presence of Ga(sulfide) on the sulfide treated samples is observed from the shift of the Ga $2p_{3/2}$ level to slightly higher binding energy. Clearly, there are no oxidized arsenic or gallium species on the surface following either sulfide procedure. A large As oxide peak at 1325.7 eV is observed for the hydroxide etched surface, indicating that the preceding acid etch may have been insufficient to remove the native oxide [11].

The As $2p_{3/2}$ (Al anode) and the S 2s (Mg anode) core levels following a saturated sulfide etch are shown at high and low electron take-off angle in Fig. 6.2. Although the S 2p core levels cannot be easily separated from the Ga 3s level, the S 2s core level is clearly visible at 226.0 eV. We also observe a S Auger signal at 2114.4 eV, which is similar to that reported by Sandroff et al. [9]. An increase in the As(sulfide) and the S 2s relative intensities at low angle indicates that the sulfided species form the uppermost atomic layer.

The arsenic to gallium and the sulfur to total metal intensity ratios for both sulfide etching procedures are listed in Table 6.1. The As 3d/Ga 3d ratios clearly show that an ammonium sulfide etch results in an As-depleted surface. Furthermore, the ratio at 45 degrees is significantly less following a saturated ammonium sulfide etch than following an unsaturated etch, suggesting that the saturated solution enhances As depletion of the surface. Since the relative As(sulfide)/As(GaAs) ratios are identical for the $2p_{3/2}$ electrons, which have smaller mean-free paths, we must assume that not all of the As depletion occurs in the upper most surface layer. These results may be important to the differences in surface reconstruction observed by RHEED

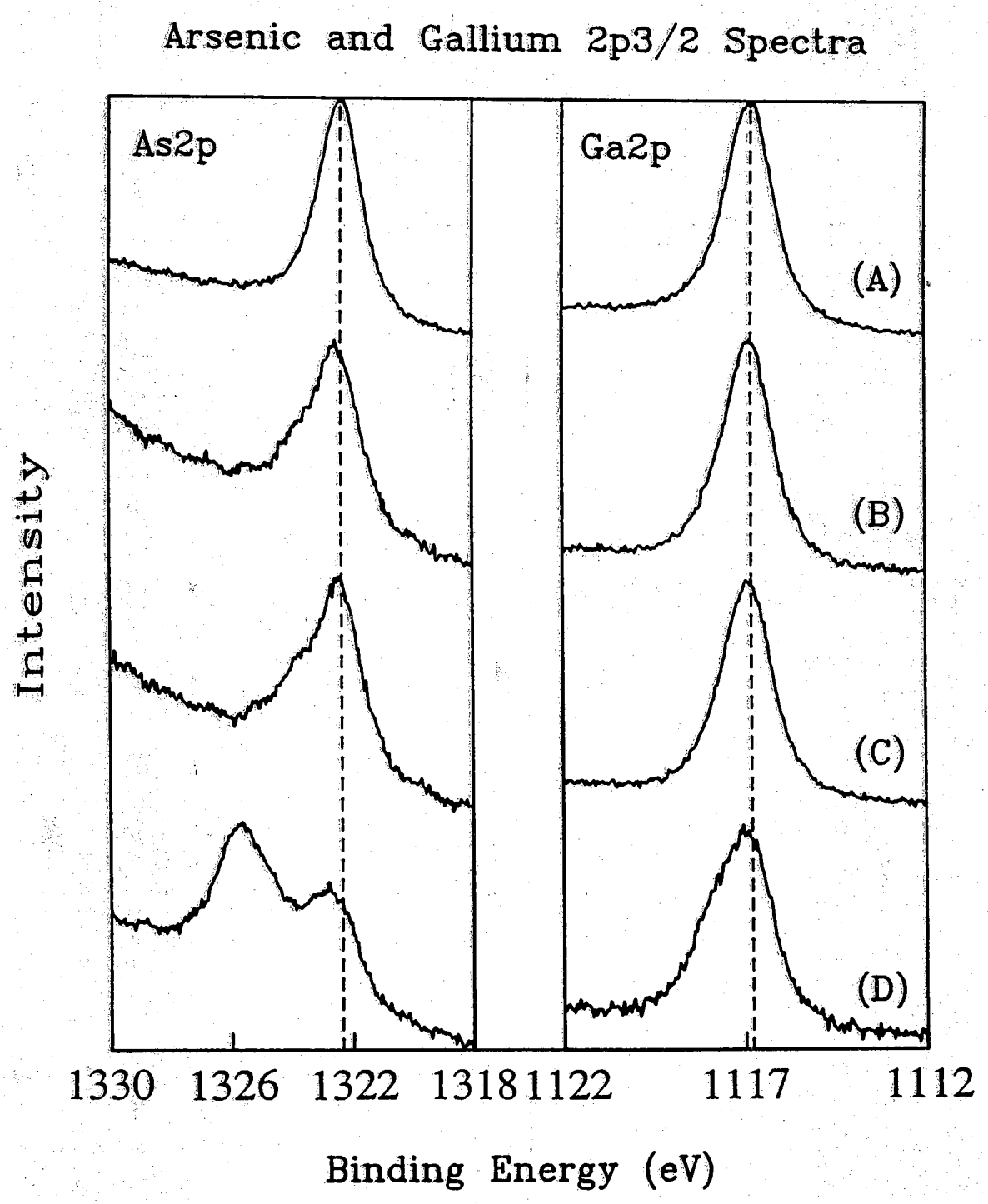

Fig. 6.1 Arsenic and gallium $2p_{3/2}$ core level spectra for (A) Ar^+ ion sputtered, (B) unsaturated ammonium sulfide etched, (C) saturated ammonium sulfide etched, and (D) ammonium hydroxide etched surfaces taken at an electron take-off angle of 15 degrees.

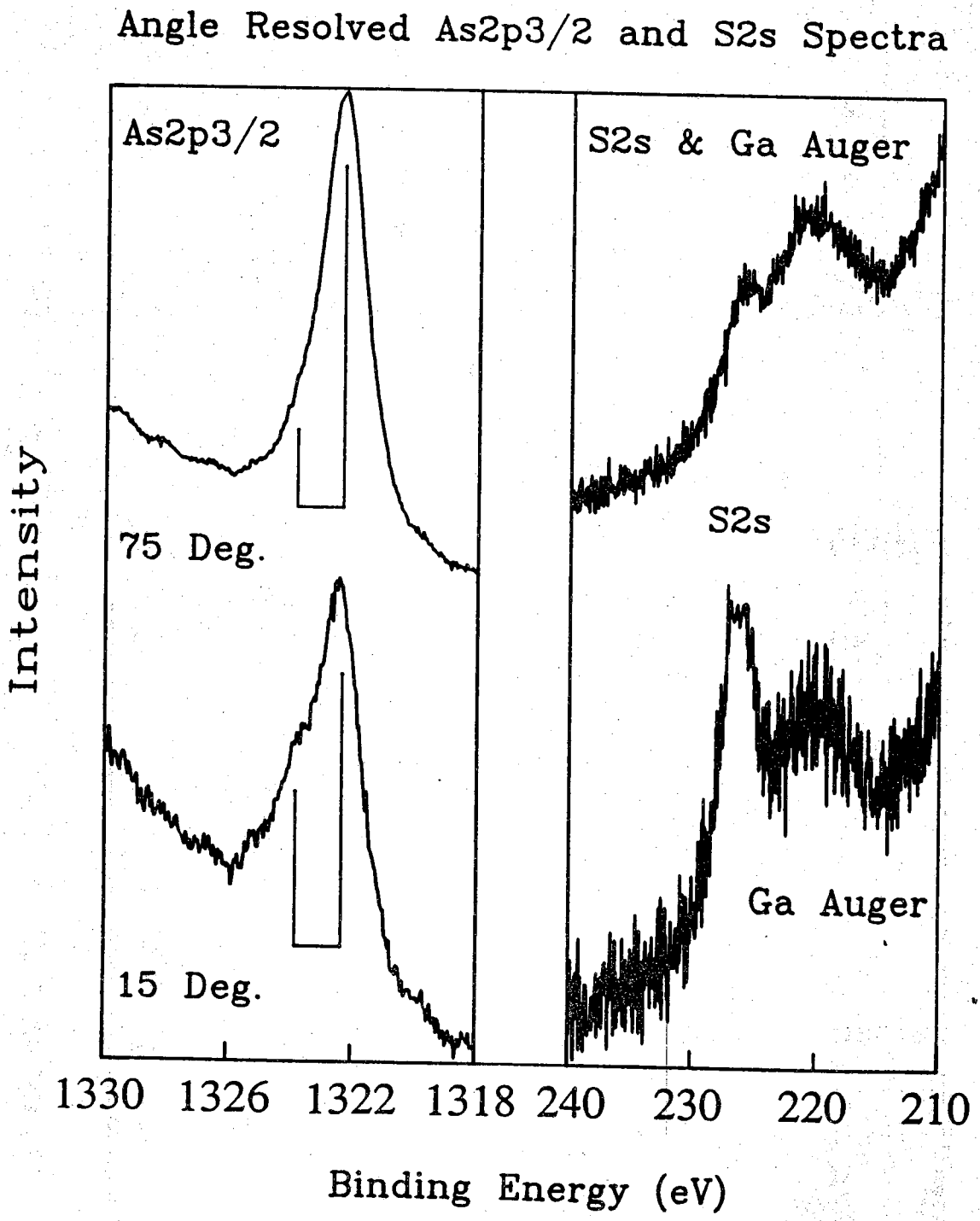

Fig. 6.2 High and low angle arsenic $2p_{3/2}$ (Al anode) and sulfur 2s (Mg anode) core level phootoelectron spectra for a GaAs surface etched with a saturated ammonium sulfide solution.

Table 6.1 Experimental photoelectron intensity ratios for As3d/Ga3d and S2s/(Ga3d + As3d) normalized by Scofield's differential photoelectron cross section (Mg radiation).

Sample	Saturated Sulfide		Unsaturated Sulfide	
Angle	As/Ga	S/(Ga + As)	As/Ga	S/(Ga + As)
15	0.67	0.16	0.78	0.16
30	0.66	0.11	0.83	0.11
45	0.65	0.09	0.82	0.09
60	1.08	0.06	0.60	0.06
75	0.71	0.05	0.92	0.06

and discussed in Section III. The sulfur to total (Ga3d + As3d) metal ratios are exactly the same for both saturated and unsaturated treatments at all angles. This is consistent with the relative ratios observed for the $2p_{3/2}$ levels and indicates that the sulfur coverage, as discussed below, is the same for both treatments.

The GaAs crystal is composed of alternating layers of Ga and As atoms which are parallel to the (100) plane. The fractional coverage of sulfur is calculated assuming the Ga and As layers are complete up to the surface [12,13], which is terminated with a uniform but not necessarily complete sulfur layer. If we assume that the mean free paths for As 3d and Ga 3d are equal and that the separated atomic layer densities for Ga and As are also equal, then the normalized ratio of sulfur to Ga + As intensities is given by,

$$\frac{J_S}{J_{Ga}+J_{As}} = \frac{a_o}{4\lambda\sin\Theta}\exp\left(\frac{d}{\lambda\sin\Theta}\right)\frac{\eta_S}{\eta_{GaAs}} \qquad (6.1)$$

where J is the intensity normalized by Scofield's photoelectron cross section [14], η_S is the density of the sulfur layer (atoms/cm^2), η_{GaAs} is the density of one complete Ga or As (100) layer (atoms/cm^2), a_o is the GaAs crystal lattice constant, λ is the photoelectron mean free path [15], d is the thickness of the sulfide layer, and Θ is the electron take-off angle, i.e. the angle between the sample surface and the electron path to the entrance slit to the analyzer. The inelastic mean free path values for Ga and As are assumed to be 23.5 Å [15]. The fractional sulfur coverage is η_S/η_{GaAs} by definition. For a sulfide layer thickness of 3.68 Å , the diameter of a sulfide ion, the sulfur coverage is calculated to be 0.86 monolayers for both saturated and unsaturated sulfide treatments. For a sulfide layer thickness of 2.25 Å , the As-S bond length in As_2S_3 [9,16], the sulfur coverage is calculated to be 0.94 monolayers. For reasons stated above [11], these coverages were calculated using intensity ratios measured at 45 degrees.

6.3 REFLECTION HIGH ENERGY ELECTRON DIFFRACTION

The samples to be treated were prepared by growing 1.5μm of undoped GaAs in a Varian GEN II molecular beam epitaxy (MBE) system. The samples were 2-inch round (100) undoped wafers which were prepared with a standard MBE cleaning procedure before placement in a non-indium wafer mount. The non-indium wafer mounting facilitated easy removal and reinsertion of the sample in the MBE and also eliminates any need for heating the sample when remounting.

After growth of the 1.5μm GaAs film, the sample was removed from the MBE and placed in a laminar-flow clean bench. The sample was left for one hour to insure a pinned surface. The sample was then placed in deionized water while an etch of 1:1:250 H_2SO_4:H_2O_2:H_2O was prepared. The sample was then etched for 30 seconds followed by a de-ionized water rinse for 30 seconds. The sample was then placed in either a saturated or unsaturated ammonium sulfide solution for 20 minutes. The ammonium sulfide solution was removed by adding deionized water and decanting. This step is critical to keep excess sulfur from depositing on the GaAs

surface. The sample was then blown dry with nitrogen and reloaded into the MBE system. It was approximately 13 minutes from the end of the ammonium sulfide soak to placement of the sample in the MBE entry chamber.

Since our XPS measurements indicated less than a monolayer of sulfur coverage and no other contaminants, we were not concerned about contamination of our MBE growth chamber. However, we outgassed the sample at 350°C for one hour in a high vacuum buffer chamber before insertion in the growth chamber which contains the RHEED analysis apparatus.

The RHEED images for the saturated and unsaturated ammonium sulfide treated GaAs samples were observed as the substrate was heated and are displayed in Fig. 6.3 and 6.4. (The sample was under an arsenic flux during the RHEED observations.) Initially for the saturated ammonium sulfide treated sample, the RHEED pattern was somewhat spotty with only a hint of surface reconstruction. At 540°C there was a dramatic change in the RHEED pattern. The main RHEED lines become streaks followed by an appearance of a 2-fold surface reconstruction in the [110] azimuth. It is possible the sub-monolayer of sulfur is starting to evaporate at this temperature, allowing the GaAs surface to reconstruct. (This interpretation is consistent with the observations of Oigawa et al. [17] who determined that the sulfur atoms are removed by heat treatments above 530°C using low-energy electron energy loss spectroscopy (LEELS).) Above 580°C the 4-fold reconstruction lines in the [$\bar{1}$10] azimuth became clearly visible, with the 2-fold reconstruction lines in the [110] azimuth dimming somewhat in comparison to the main lines. This RHEED behavior was observed on three separate wafers which were treated with the saturated ammonium sulfide solution.

The RHEED behavior of the GaAs surface treated with the unsaturated ammonium sulfide solution was considerably different from that described above for the saturated ammonium sulfide treatment. The initial RHEED pattern exhibited a (2x2) surface reconstruction. At 500°C the surface reconstruction started to change to a (4x2) structure, although all the 4-fold reconstruction lines in the [$\bar{1}$10] azimuth were not visible. At 540°C the 4-fold reconstruction lines in the [$\bar{1}$10] azimuth are clearly visible.

Upon initializing growth on the ammonium sulfide treated samples at a substrate temperature of 600°C, the reconstruction lines in the [110] azimuth brightened, but the pattern was not unlike the pattern of the saturated ammonium sulfide treated surface at a substrate temperature near or slightly higher than 540°C as shown in Fig. 6.5. The use of the ammonium sulfide treatment may be a promising approach for MBE regrowth applications.

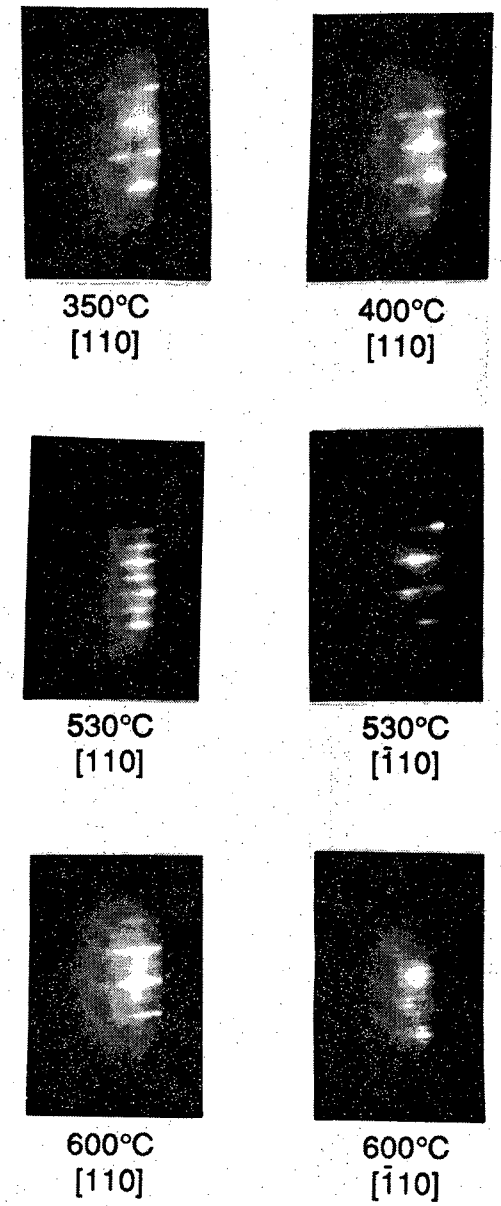

Fig. 6.3 Reflection high energy electron diffration pattern of a GaAs surface treated with a saturated ammonium sulfide solution.

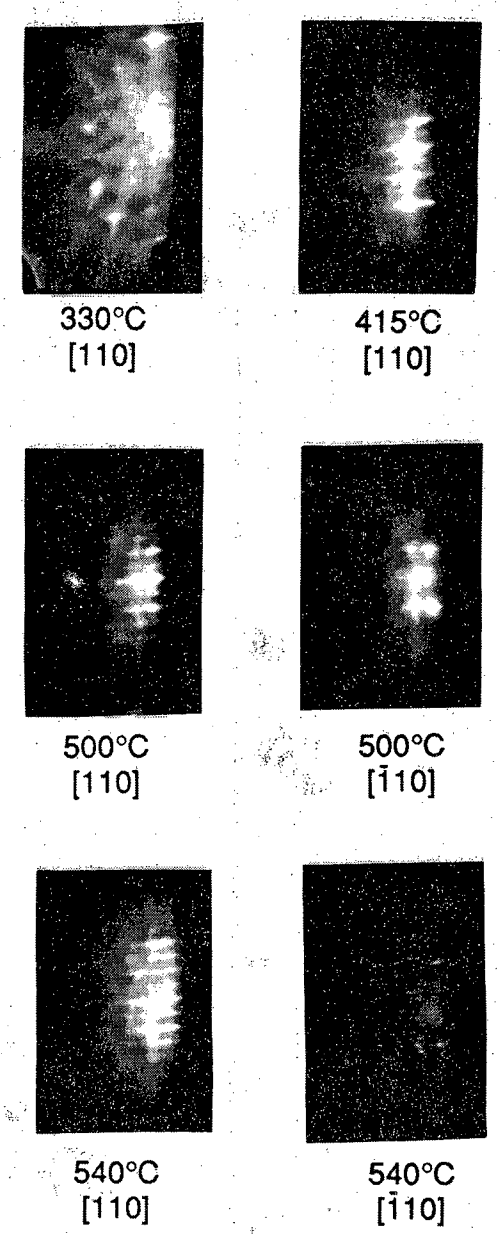

Fig. 6.4 Reflection high energy electron diffraction pattern of a GaAs surface treated with an unsaturated ammonium sulfide solution.

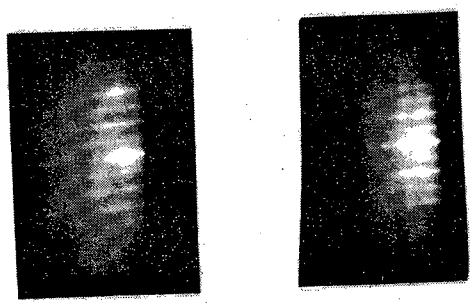

Fig. 6.5 Reflection high energy electron diffraction pattern of a growing film on a GaAs surface which was treated with (a) a saturated solution and (b) an unsaturated ammonium sulfide solution.

6.4 SCHOTTKY BARRIER FORMATION

The devices used in this study were fabricated from two (100) GaAs wafers. The first wafer was an n-type molecular beam epitaxially grown 1.25μm thick epilayer on an n^+ substrate. The second was similar except it was p-type. The doping of the epilayers was approximately $1x10^{17}$ cm^{-3}. The wafers were then cleaved into small samples and soldered on stainless steel mounts with indium. On each mount both n and p-type samples were placed side by side. Each mount was then prepared for evaporation. The ammonium sulfide treated mounts were prepared as previously described for the RHEED measurements. The control devices were etched in the same batch of etchant as the treated samples and just before loading into the deposition system they were soaked in 1:1 $NH_4OH:H_2O$. Three mounts were loaded into the deposition system for each evaporation, two treated and one control. One treated sample was placed beside the control sample and the other on a cooling stage which was cooled to 77 K during the metal evaporation. Metals were then thermally evaporated on all three mounts simultaneously. The devices were then fabricated using normal photolithographic processes and wet chemical etching.

The forward bias current-voltage (I-V) characteristics of the devices are shown in Fig. 6.6a,b and 6.7a,b. Fig. 6.6a shows the drastic change induced by the ammonium sulfide treatment on gold Schottky barriers to n-type GaAs. The upper curve is for the control or NH_4OH treated devices. The middle curve is for the ammonium sulfide treated devices and the lower curve is again a treated device but with the metal deposition done at a substrate temperature of 77 K. As can readily be seen there is over a three order of magnitude change in the current density. Shown in Fig. 6.6b is the same family of curves for gold Schottky barriers to p-type GaAs. Again the chemical treatment changes the I-V characteristics however, this time there is more current in the treated devices, with additional current in the cooled treated sample. The I-V characteristics in Fig. 6.6 indicate that the gold Schottky barrier has been raised on the n-type treated sample and lowered on the p-type treated sample. Shown in Fig. 6.7a and 6.7b are similar curves for aluminum. For aluminum the trend is reversed, more current is observed for the treated n-type samples and less for the p-type, indicating the barrier height is lowered for the n-type and raised for the p-type.

To determine barrier heights, the I-V characteristics were analyzed in terms of a thermionic emission model of current transport: [18]

$$J=J_s\exp\left[\frac{qV}{nkT}\right]\left[1-\exp\left[\frac{-qV}{kT}\right]\right] \qquad (2)$$

where J_s is the saturation current density and n is the ideality factor. The saturation current density was calculated by a least squares fit to equation 2. The effective barrier heights were determined from the following relation for saturation current density:

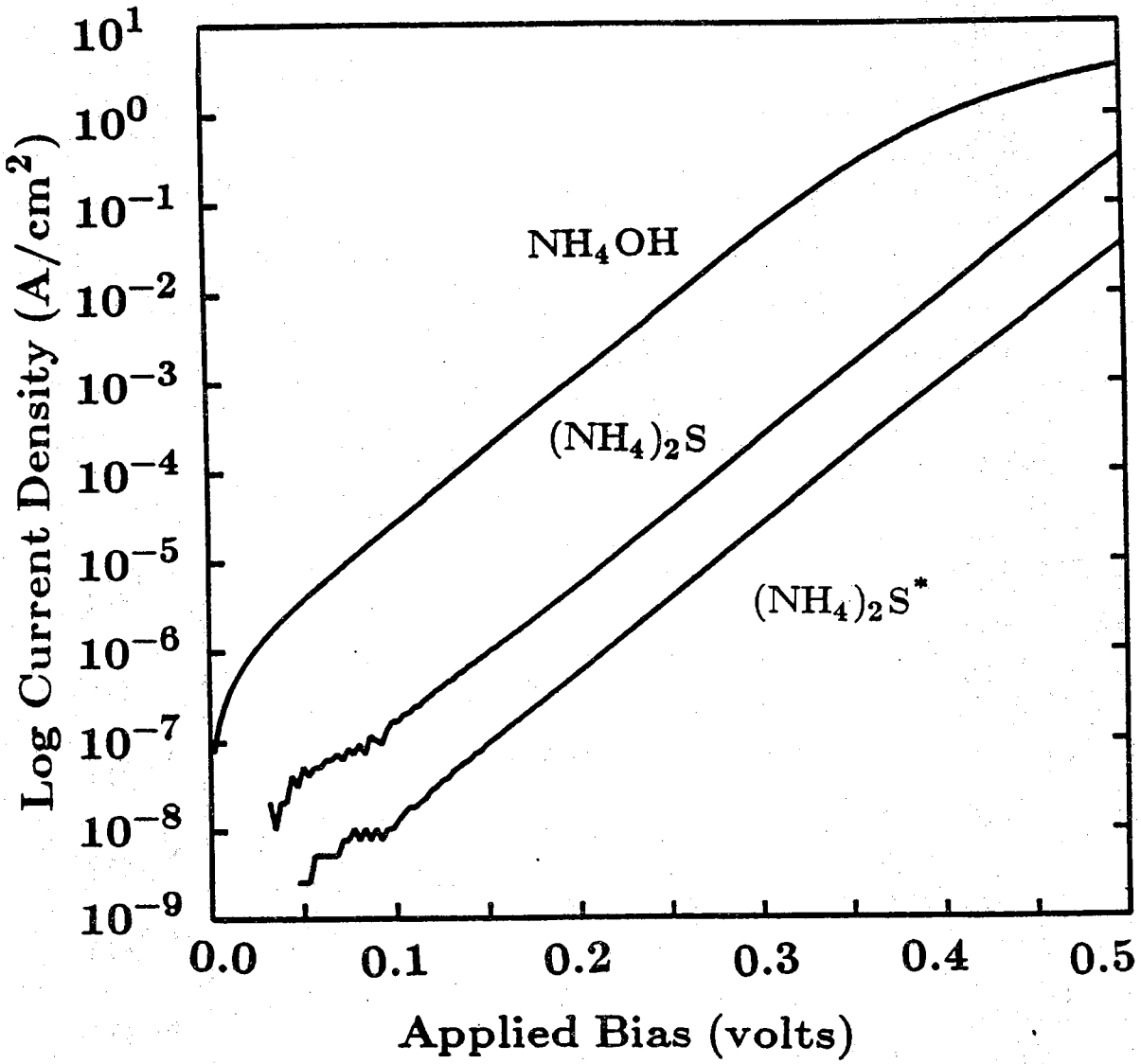

Fig. 6.6a Forward bias current-voltage characteristics measured at 300 K for gold Schottky barriers on n-type GaAs. The $(NH_4)_2S^*$ curve represents samples which were cooled to 77 K during the metal deposition.

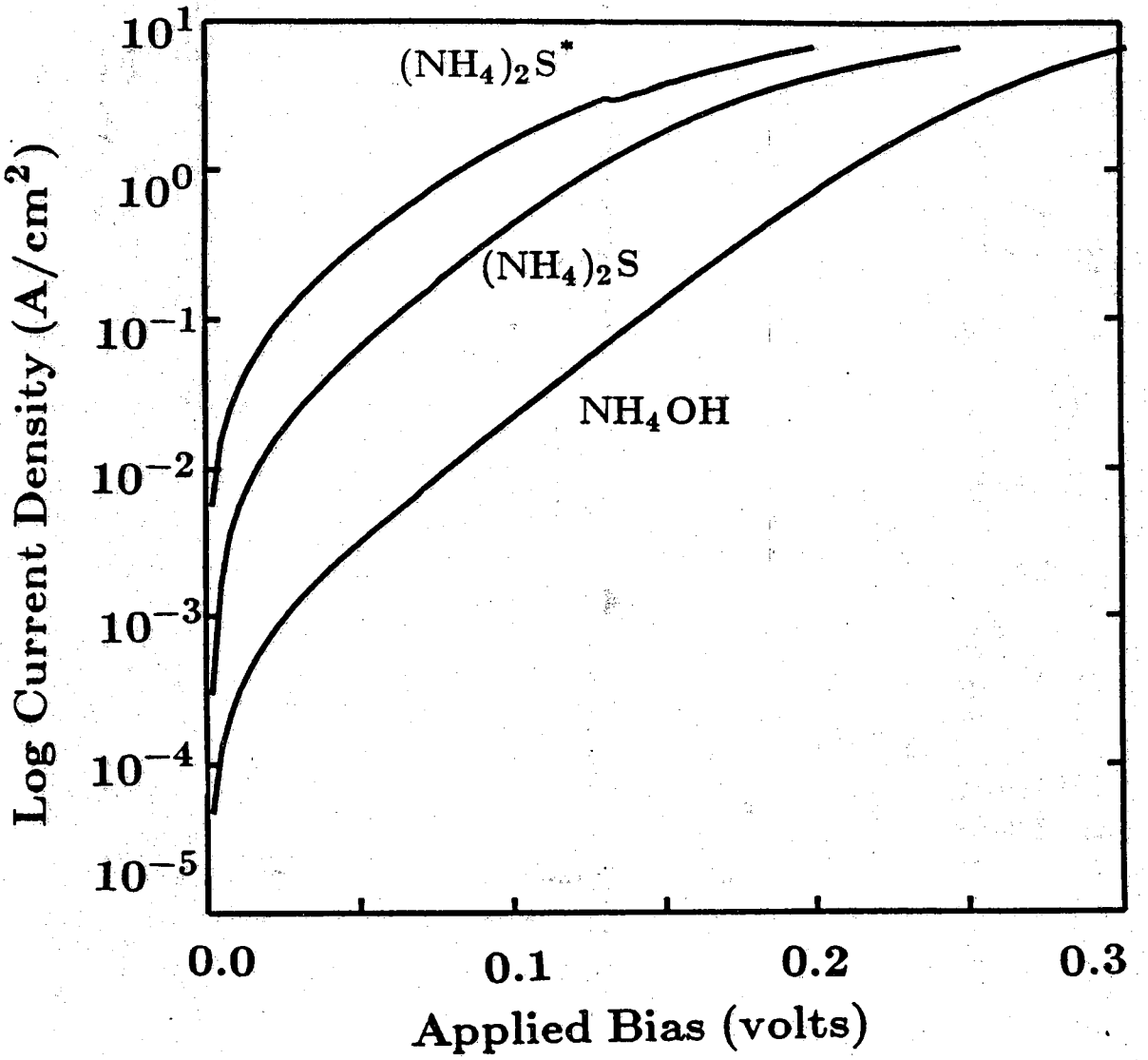

Fig. 6.6b Forward bias current-voltage characteristics measured at 300 K for gold Schottky barriers on p-type GaAs. The $(NH_4)_2S^*$ curve represents samples which were cooled to 77 K during the metal deposition.

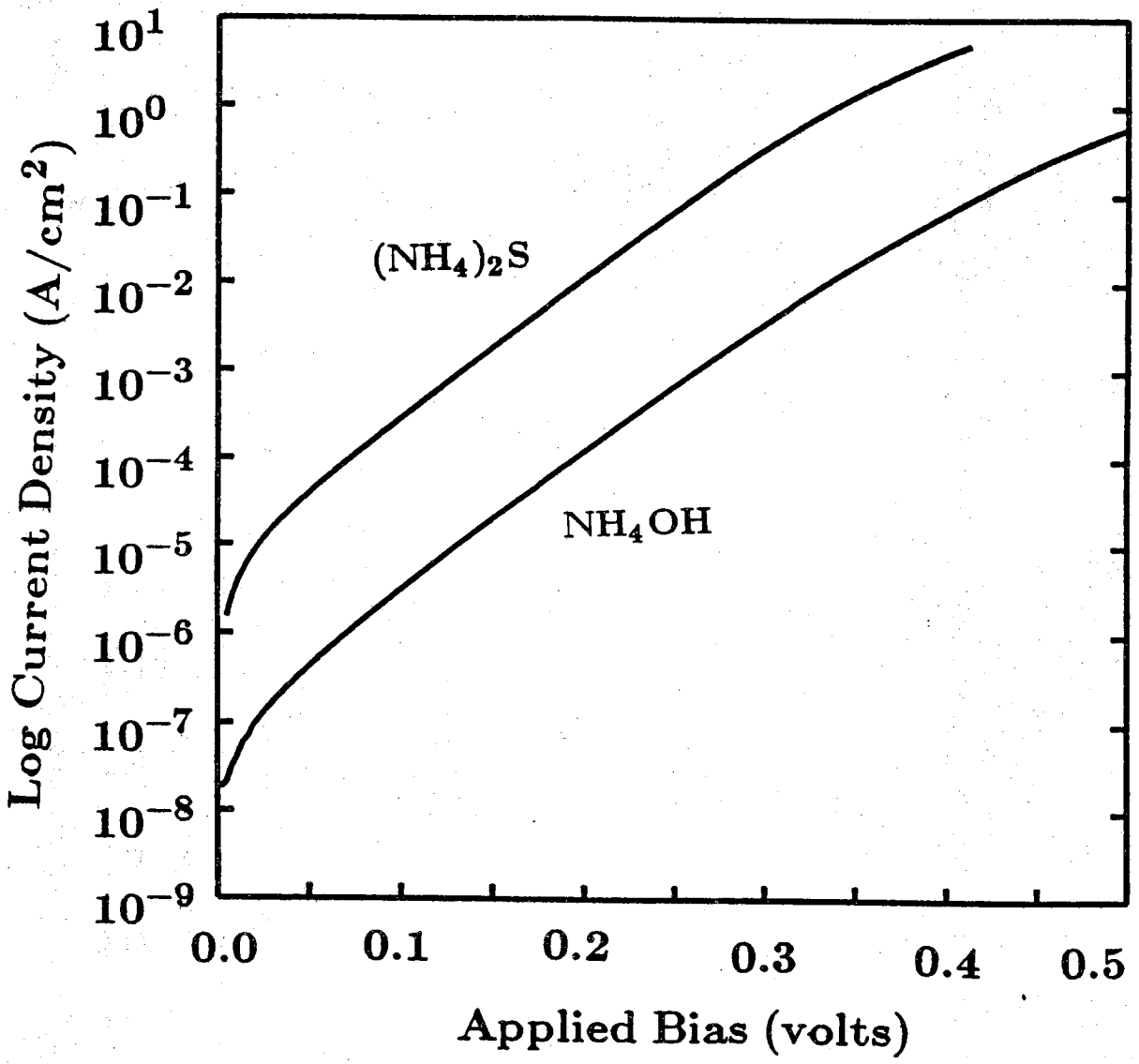

Fig. 6.7a Forward bias current-voltage characteristics measured at 300 K for aluminum Schottky barriers on n-type GaAs. The $(NH_4)_2S^*$ represents samples which were cooled to 77 K during the metal deposition.

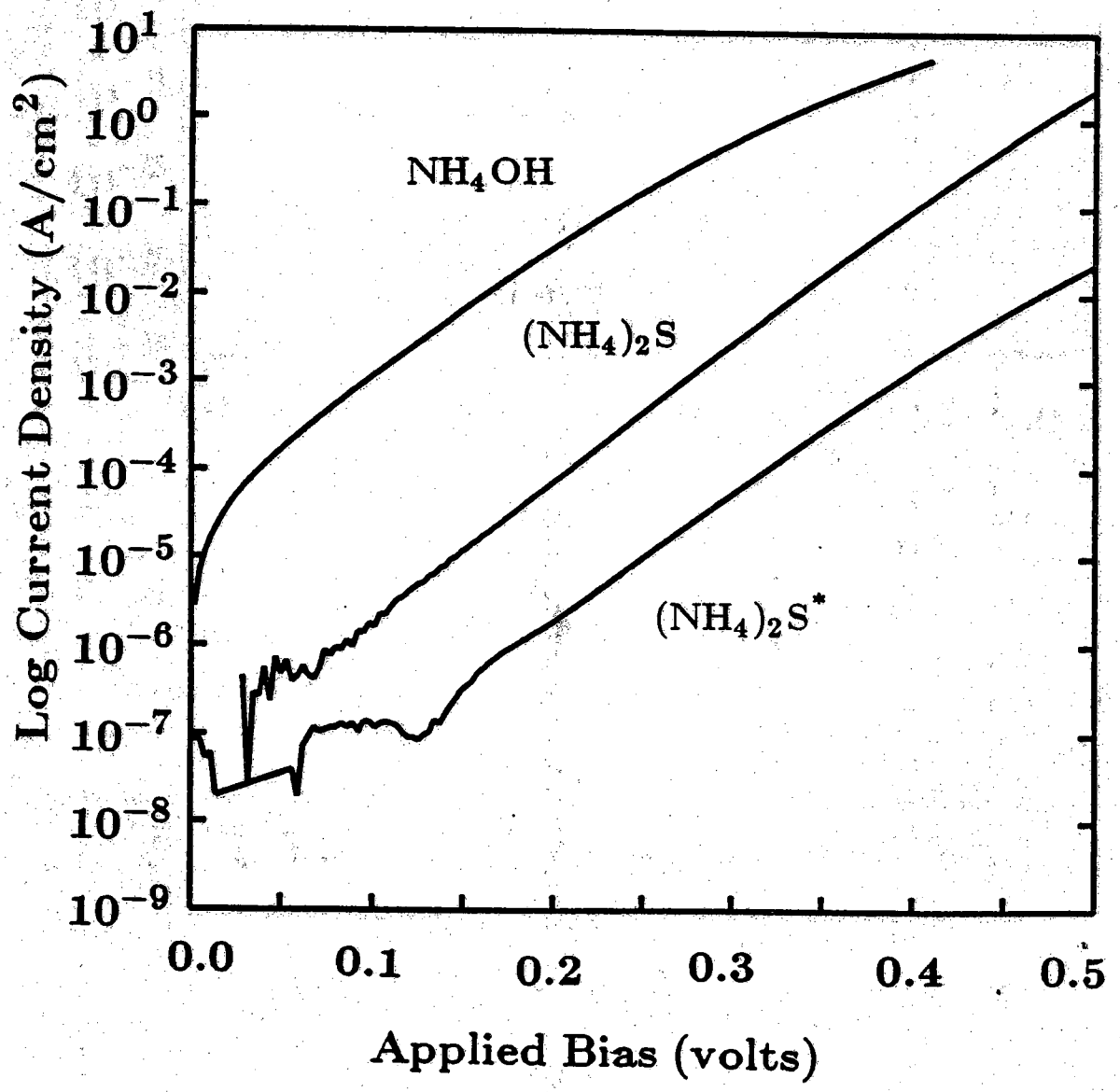

Fig. 6.7b Forward bias current-voltage characteristics measured at 300 K for aluminum Schottky barriers on p-type GaAs. The $(NH_4)_2S^*$ represents samples which were cooled to 77 K during the metal deposition.

$$J_s = A^* T^2 \exp\left[\frac{-q}{kT}(\phi_{bn}-\Delta\phi)\right] \quad (3)$$

where A^* is the effective Richardson constant and ϕ_{bn} - $\Delta\phi$ is the effective barrier height, and $\Delta\phi$ is the image force correction term at zero bias. A summary of barrier heights and saturation current densities is given in Table 6.2. The data given in Figs. 6.6 and 6.7 and Table 6.2 are quite representative of the devices on each film. Not only were numerous devices measured, but numerous devices with varying area and perimeter were measured. Since the RHEED patterns for this type of treatment were spotty to begin with, it was possible there are islands of sulfur on the surface. To rule out the possibility that the observed change in barrier height was due to a change in effective device area, activation energy measurements were conducted on selected samples. The barrier heights obtained from activation energy measurements were in good agreement with those obtained from equations 2 and 3.

The barrier height we obtained for gold on ammonium sulfide treated n-type GaAs is similar to the Schottky barrier height obtained by Waldrop for gold on sulfur exposed n-type GaAs [19]. However the barrier height we obtained for aluminum on ammonium sulfide treated GaAs is much higher than that observed by Massies et al. on n-type GaAs exposed to H_2S [20]. This indicates that the full potential for the barrier shift for aluminum may not have been achieved by our method.

6.5 DISCUSSION AND CONCLUSIONS

Although various groups have suggested that the sulfide treatments result in the Fermi level being repinned at a new position [21-23], there is now considerable evidence to support the claim that the sulfide treatments reduce the GaAs surface state density and unpin the Fermi-level. The metal/insulator/GaAs work of Oigawa et al. has shown a definite measurable reduction in the surface state density with the incorporation of an ammonium sulfide treatment [17]. The surface recombination velocity has been shown to be reduced by sulfide treatments from both rf induction [8] and photoluminescence measurements [1]. The reduction in surface recombination velocity is the only explanation consistent with the results of Sandroff et al. and Carpenter et al. for sulfide treatments of etched edges of bipolar devices [1-3,7].

Recently, Brillson et al. have demonstrated that metals deposited on a pristine GaAs surface, such as an as-grown MBE surface, produce Schottky barriers which are more sensitive to the metal work function than previously demonstrated [24]. Furthermore, Viturro et al. have shown if in addition to having such a pristine GaAs surface, the metals are deposited with the substrate at low temperatures nearly ideal Schottky barriers are obtained [25]. Our aluminum and gold Schottky barriers formed on ammonium sulfide treated GaAs show similar Schottky barrier trends to those of Viturro et al. [25]. It is intriguing to speculate that our result is due to a low surface state density after deposition of aluminum and gold on the ammonium sulfide treated

Table 6.2 Summary of saturation current densities, Schottky barrier heights, and ideality factors for various surface treatments. All measurements were performed at room temperature. Note $(NH_4)_2S^*$ represents samples which were cooled to 77 K during metal deposition.

Surface treatment	metal	n-type J_s	n-type $\phi_{bn} - \Delta\phi$	n-type n	p-type J_s	p-type $\phi_{bp} - \Delta\phi$	p-type n
NH_4OH	Au	7.3×10^{-7}	.781	1.06	5.7×10^{-4}	.585	1.09
$(NH_4)_2S$	Au	2.1×10^{-9}	.841	1.08	6.1×10^{-3}	.523	1.19
$(NH_4)_2S^*$	Au	1.8×10^{-10}	.917	1.09	1.9×10^{-2}	.461	1.21
NH_4OH	Al	1.1×10^{-7}	.767	1.03	5.7×10^{-5}	.592	1.02
$(NH_4)_2S$	Al	1.7×10^{-5}	.632	1.04	6.3×10^{-8}	.794	1.09
$(NH_4)_2S^*$	Al	-	-	-	5.9×10^{-9}	.894	1.16

GaAs surface. However, Waldrop has investigated Schottky barrier formation when metals are deposited on a GaAs surface which had prior exposure to elemental sulfur [26]. Waldrop observed a large decrease in Schottky barrier heights for Al and Mn due to a contact metal-chalcogen chemical reaction. Waldrop also observed an increase in Schottky barrier heights with some nonreactive noble metal-chalcogen interfaces. In spite of the cause of the Schottky barrier variation, it appears that the ammonium sulfide treatment is a very easy processing step which can be used to obtain a wide range of Schottky barrier heights for metals deposited on GaAs.

CHAPTER 6 REFERENCES

1. C. J. Sandroff, R. N. Nottenburg, J.-C. Bishoff, and R. Bhat, Appl. Phys. Lett. 51, 33 (1987).
2. R. N. Nottenburg, C. J. Sandroff, D. A. Humphrey, T. H. Hollenbeck, and R. Bhat, Appl. Phys. Lett. 52, 218 (1988).
3. M. S. Carpenter, M. R. Melloch, M. S. Lundstrom, and S. P. Tobin, Appl. Phys. Lett. 52, 2157 (1988).
4. M. S. Carpenter, M. R. Melloch, and T. E. Dungan, Appl. Phys. Lett. 53, 66 (1988).
5. M. S. Carpenter and M. R. Melloch, 1988 International Symposium on GaAs and Related Compounds, Atlanta, Georgia, Sept. 11-14, 1988.
6. Jia-Fa Fan, Haruhiro Oigawa, and Yasuo Nannichi, Japanese J. Appl. Phys. 27, L2125 (1988).
7. E. Yablonovitch, C. J. Sandroff, R. Bhat, and T. Gmitter, Appl. Phys. Lett. 51, 439 (1987).
8. E. Yablonovitch, H. M. Cox, and T. J. Gmitter, Appl. Phys. Lett. 52, 1002 (1988).
9. C. J. Sandroff, M. S. Hegde, L. A. Farrow, C. C. Chang, and J. P. Harbison, Appl. Phys. Lett. 54, 362 (1989).
10. B. A. Cowans, Z. Dardas, W. N. Delgass, M. S. Carpenter, and M. R. Melloch, Appl. Phys. Lett. 54, 365 (1989).
11. P. Alnot, J. Olivier, F. Wyczisk, and C.S. Fadley, J. Electron Spectro. Rel. Phen. 43, 263 (1987).
12. W. Ranke and K. Jacobi, Surface Science 63, 33 (1977).
13. W. Ranke and K. Jacobi, Surface Science 47, 525 (1975).
14. J. H. Scofield, J. Electron Spectro. Rel. Phen. 8, 129 (1976).
15. C. M. Kwei and L.W. Chen, Surface and Interface Analysis 60 (1988).
16. J. Massies, F. Dezaly, and N. T. Linh, J. Vac. Sci. Tech B17, 1134 (1980).
17. H. Oigawa, J. Fan, Y. Nannichi, K. Ando, K. Saiki, and A. Koma, Extended Abstracts of the 20th (1988 International) Conference on Solid State Devices and Materials, 263 (1988).
18. E. H. Rhoderick, IEE Proc 129, Pt. I, 1 (1982).
19. J. R. Waldrop, J. Vac. Sci. Technol. B 3 1197 (1985).
20. J. Massies, J. Chaplart, M. Laviron, and N.T. Linh, Appl. Phys. Lett. 38 693 (1981).
21. R. S. Besser and C. R. Helms, Appl. Phys. Lett. 52 1707 (1988).
22. H. Hasegawa. T. Sawada, H. Ishii, S. Konishi, Y. Liu, T. Saitoh, and H. Ohno, Extended Abstracts of the 20th (1988 International) Conference on Solid State Devices and Materials, 263 (1988).
23. D. Liu, T. Zhang, R. A. LaRue, J.S. Harris, Jr., and T.W. Sigmon, Appl. Phys. Lett. 53 1059 (1988).

24. L. J. Brillson, R. E. Viturro, C. Mailhiot, J. L. Shaw, N. Tache, J. McKinley, G. Margaritondo, J. M. Woddall, P. D. Kirchner, G. D. Pettit, and S. L. Wright, J. Vac. Sci. Technol. B6, 1263 (1988).

25. R. E. Viturro, S. Chang, J. L. Shaw, C. Mailhiot, L. J. Brillson, R. Zanoi, Y. Hwu, G. Margaritondo, P. D. Kirchner, and J. M. Wooda II, Sixteenth Annual Conference on the Physics and Chemistry of Semiconductor Interfaces, Bozeman, Montana, Feb. 7-9, 1989.

26. J. R. Waldrop, Appl. Phys. Lett. 47, 1301 (1985).

APPENDIX 1: LIST OF 1988-1989 PUBLICATIONS

This appendix contains reprints of the publications which resulted from the work conducted during the past year.

[1] M. S. Carpenter, M. R. Melloch, and T. E. Dungan, "Schottky barrier formation on $(NH_2)_2S$-treated n- and p-type (100) GaAs," *Appl. Phys. Lett.* 53 (1), pp. 66-68, 4 July 1988,

[2] M. E. Klausmeier-Brown, P. D. DeMoulin, H. L. Chuang, M. S. Lundstrom, and M. R. Melloch, S. P. Tobin, "Influence of Bandgap Narrowing Effects in p^+-GaAs on Solar Cell Performance," Conf. Rec., 20th IEEE Photovoltaic Specialists Conference, Las Vegas, NV, pp. 503-507, Sept. 1988.

[3] M. S. Carpenter and M. R. Melloch, "Formation of Schottky barriers on reduced surface state gallium arsenide," Inst. Phys. Conf. Ser. No. 96: Chapter 6, paper presented at Int. Symp. GaAs and Related Compounds, Atlanta, GA, 1988, pp. 381-386.

[4] H. L. Chuang, P. D. DeMoulin, M. E. Klausmeier-Brown, M. R. Melloch, and M. S. Lundstrom, "Evidence for band-gap narrowing effects in Be-doped, p-p^+ GaAs homojunction barriers," *J. Appl. Phys.* 64 (11), pp. 6361-6364, 1 December 1988.

[5] B. A. Cowans, Z. Dardas, W. N. Delgass, M. S. Carpenter and M. R. Melloch, "X-ray photoelectron spectroscopy of ammonium sulfide treated GaAs (100) surfaces," *Appl. Phys. Lett.* 54 (4), pp. 365-367, 23 January 1989.

[6] H.L. Chuang, M.E. Klausmeier-Brown, M.R. Melloch, and M.S. Lundstrom, ''Effective Minority Carrier Hole Confinement of Si-Doped, n^+–n GaAs Homojunction Barriers,'' *J. Appl. Phys.*, Vol. 66, pp. 273-277, 1989.

APPENDIX 2: BIBLIOGRAPHY OF SERI-SUPPORTED PUBLICATIONS

This appendix lists the various reports, theses, conference presentations, and journal publications that have resulted from research supported under this subcontract.

Reports:

[1] M. S. Lundstrom, M. R. Melloch, C. S. Kyono, C. P. McMahon, R. E. Noren, and D. P. Rancour, "Basic Studies of III-V High-Efficiency Cell Components," TR-EE-86-35, Aug. 1986, 163 pages.

[2] M. S. Lundstrom, M. R. Melloch, R. F. Pierret, P. D. DeMoulin, D. P. Rancour, C. S. Kyono, M. S. Carpenter, and M.E. Klausmeier-Brown, "Basic Studies of III-V, High-Efficiency Cell Components," TR-EE 87-33, Sept. 1987, 71 pages.

[3] M. S. Lundstrom, M. R. Melloch, R. F. Pierret, M. S. Carpenter, H. L. Chuang, P. D. DeMoulin, M. R. Klausmeier-Brown, G. B. Lush, D. P. Rancour, "Basic Studies of III-V High-Efficiency Cell Components," TR-EE 88-57, Dec. 1988, 109 pages.

Theses:

[1] Christian Paul McMahon, "A Quantum Efficiency Device for Solar Cells," MSEE thesis, August 1986.

[2] Robert E. Noren, "MBE Growth and Characterization of GaAs Heteroface Solar Cells," MSEE thesis, August 1986.

[3] Michael S. Carpenter, "Characterization and Passivation of Gallium Arsenide Surfaces," MSEE thesis, December 1987.

[4] David P. Rancour, "Investigation of GaAs Solar Cell Structures Using Deep Level Transient Spectroscopy," Ph.D. thesis, August 1988.

Conference Presentations:

[1] M. S. Lundstrom and M. R. Melloch, "Basic Studies of III-V High-Efficiency Cell Components," presented at the 7th SERI Photovoltaic Advanced Research and Development Project Review, Denver, CO, May 13-15, 1986.

[2] P. D. DeMoulin, C. S. Kyono, M. S. Lundstrom, and M. R. Melloch, "Dark I-V Characterization of GaAs P/N Heteroface Cells," 19th IEEE Photovoltaic Specialists Conf., New Orleans, LA, May 1987, pp. 93-97.

[3] M. E. Klausmeier-Brown, C-S. Kyono, M. S. Carpenter, M. R. Melloch, M. S. Lundstrom, and R. F. Pierret, "Experimental Characterization of Minority Carrier Mirrors for GaAs-Based Solar Cells," Proc. 19th IEEE Photovoltaic Specialist's Conf., New Orleans, May 1987, pp. 1174-1179.

[4] M. S. Lundstrom, "Device Physics of Crystalline Cells," presented at the 8th Photovoltaic Advanced Research and Development Project Review Meeting, Denver, Co, Nov. 16-18, 1987.

[5] M. E. Klausmeier-Brown, P. D. DeMoulin, M. S. Lundstrom, M. R. Melloch, and S. P. Tobin, "Measurement of Bandgap Narrowing Effects in p-GaAs and Implications for AlGaAs/GaAs HBT Performance," presented at the 46th Device Research Conference, Boulder, CO, June 20-22, 1988.

[6] M. E. Klausmeier-Brown, P. D. DeMoulin, H. L. Chuang, M. S. Lundstrom, M. R. Melloch, and S. P. Tobin, "Influence of Band Gap Narrowing Effects in p^+ GaAs on Solar Cell Performance," Conf. Rec., 20th IEEE Photovoltaic Specialists Conference, Las Vegas, NV, Sept. 26-30, 1988, pp. 503-507.

[7] M. S. Carpenter, M. R. Melloch, B. A. Cowans, and W. N. Delgass, "Investigations of $(NH_4)_2S$ Surface Treatments on GaAs," 16th Conference on Physics and Chemistry of Semiconductor Interfaces, Bozeman, Montana, February 7-9, 1989.

[8] M. S. Lundstrom, "Heavy Doping Effects in HBTs," presented at the Workshop on Compound Semiconductor Materials and Devices, WOCSEMMAD, Hilton Head, S.C., Feb. 20-22, 1989.

[9] M. E. Klausmeier-Brown, M. S. Lundstrom, and M. R. Melloch, "Electrical Measurements of Bandgap Shrinkage in Heavily Doped p-type GaAs," presented at the 1989 Electronic Materials Conference, June 21-23, 1989, Boston, MA.

[10] G. B. Lush, T. B. Stellwag, A. Keshavarzi, S. Venkatesan, M. R. Melloch, M. S. Lundstrom and R. F. Pierret, "Correlation of Material Properties and Recombination Losses in $Al_{0.2}Ga_{0.8}As$ Solar Cells," presented at the 9th Photovoltaic Advanced Research and Development Review Meeting, Lakewood, CO, May 24-26, 1989.

[11] M. R. Melloch, S. P. Tobin, C. Bajgar, T. B. Stellwag, A. Keshavarzi, M. S. Lundstrom, and K. Emery, "High-Efficiency GaAs Solar Cells Grown by Molecular Beam Epitaxy," Tenth Molecular Beam Epitaxy workshop, Raleigh, NC, September 13-15, 1989.

Journal Publications:

[1] M. R. Melloch, C. P. McMahon, M. S. Lundstrom, J. A. Cooper, Jr., Q-D. Qian, and S. Bandyopadhyay, "Bias-Dependent Photoresponse of p^+in GaAs/AlAs/GaAs Diodes," *Appl. Phys. Lett.*, Vol. 50, p. 161-163, Jan. 19, 1987.

[2] P. D. DeMoulin, M. S. Lundstrom, and R. J. Schwartz, "Back-Surface Field Design for n^+p GaAs Cells," *Solar Cells,* Vol. 20, pp. 229-236, March-April 1987.

[3] M. R. Melloch, C. P. McMahon, M. S. Lundstrom, J. A. Cooper, Jr., and Q-D. Qian, "Photocollection Efficiency of GaAs/AlAs/GaAs p^+in and n^+ip Photodiodes," *Solar Cells,* pp. 233-240, June-August 1987.

[4] D. Rancour, M. R. Melloch, R. F. Pierret, M. S. Lundstrom, M. E. Klausmeier-Brown and C. S. Kyono, "Recombination Current Suppression in GaAs P-N Junctions Grown on AlGaAs Buffer Layers by Molecular Beam Epitaxy," *J. Appl. Phys.*, Vol. 62, pp. 1539-1541, Aug. 15, 1987.

[5] M. S. Lundstrom, "Device Physics of Crystalline Solar Cells," *Solar Cells,* Vol. 24, pp. 91-102, May-June 1988.

[6] M. S. Carpenter, M. R. Melloch, M. S. Lundstrom, and S. P. Tobin, "Effects of Na_2S and $(NH_4)_2S$ Edge Passivation Treatments on the Dark Current-Voltage Characteristic of GaAs pn Diodes," *Applied Physics Letters,* Vol. 52, pp. 2157-2159, June 20, 1988.

[7] M. E. Klausmeier-Brown, M. S. Lundstrom, M. R. Melloch, and S. P. Tobin, "Effects of Heavy Impurity Doping on Electron Injection in p^+-n GaAs Diodes," *Applied Physics Letters,* Vol. 52, pp. 2255-2257, June 27, 1988.

[8] M. E. Klausmeier-Brown, C. S. Kyono, P. D. DeMoulin, S. P. Tobin, M. S. Lundstrom, and M. R. Melloch, "Sequential Etch Analysis of Electron Injection in P^+ GaAs," *IEEE Trans. Electron Devices,* Vol. ED-35, pp. 1159-1161, July 1988.

[9] M. S. Carpenter, M. R. Melloch, and T. E. Dungan, "Schottky Barrier Formation on $(NH_4)_2$ S-treated n- and p-type (100) GaAs," *Appl. Phys. Lett.* 53, pp. 66-68, July 4, 1988.

[10] P. D. DeMoulin, S. P. Tobin, M. S. Lundstrom, M. S. Carpenter, and M. R. Melloch, "Influence of Perimeter Recombination on High-Efficiency GaAs P/N Heteroface Solar Cells," *Electron Device Letters,* Vol. EDL-9, pp. 368-370, August 1988.

[11] H. L. Chuang, P. D. DeMoulin, M. E. Klausmeier-Brown, M. R. Melloch, and M. S. Lundstrom, "Evidence for Bandgap Narrowing Effects in Be-Doped, p-p^+ GaAs Homojunction Barriers," *Journal of Appl. Phys.*, Vol. 64, pp. 6361-6364, Nov. 1988.

[12] B. A. Cowans, Z. Dardas, W. N. Delgass, M. S. Carpenter, and M. R. Melloch, "X-ray Photoelectron Spectroscopy of Ammonium Sulfide Treated GaAs (100) Surfaces," *Appl. Phys. Lett.*, Vol. 54, pp. 365-367, January 23, 1989.

[13] D. P. Rancour, R. F. Pierret, M. S. Lundstrom and M. R. Melloch, "Application of Isothermal Current Deep Level Transient Spectroscopy to Solar Cells," *J. Appl. Phys.*, Vol. 65, pp. 2173-2176, March 1, 1989.

[14] P. D. DeMoulin and M. S. Lundstrom, "Projections of GaAs Solar Cell Performance Limits Based on 2-D Numerical Simulation," *IEEE Trans. Electron Devices*, Vol. 36, pp. 897-905, May 1989.

[15] H. L. Chuang, M. E. Klausmeier-Brown, M. R. Melloch, and M. S. Lundstrom, "Effective Minority Carrier Hole Confinement of Si-doped, n^+/n GaAs Homojunction Barriers," *J. Appl. Phys.*, Vol. 66, pp. 273-278, July 1989.

[16] M. S. Carpenter, M. R. Melloch, B. A. Cowans, Z. Dardas, and W. N. Delgass, "Investigations of Ammonium Sulfide Surface Treatments on GaAs," *Journal of Vacuum Science and Technology B*, Vol. 7, July-August 1989.

[17] M. S. Lundstrom, M. E. Klausmeier-Brown, and M. R. Melloch, "Effects of Heavy Impurity Doping on AlGaAs/GaAs Bipolar Transistors," *IEEE Trans. Electron Dev.*, Vol. 36, Oct. 1989.

[18] M. R. Melloch, S. P. Tobin, T. B. Stellwag, C. Bajgar, A. Keshavarzi, M. S. Lundstrom, and K. Emery, "High-Efficiency GaAs Solar Cells Grown by Molecular Beam Epitaxy," *Journal of Vacuum Science and Technology B*, Vol. 8, March-April 1990.

[19] S. P. Tobin, S. M. Vernon, C. Bajgar, S. J. Wojtczuk, M. R. Melloch, A. Keshavarzi, T. B. Stellwag, S. Venkatesan, M. S. Lundstrom, and K. A. Emery, "Assessment of MOCVD- and MBE-Grown GaAs for High-Efficiency Solar Cell Applications, submitted to *IEEE Trans. Electron Devices*.

[20] G. B. Lush, T. B. Stellwag, A. Keshavarzi, S. Venkatesan, M. R. Melloch, M. S. Lundstrom and R. F. Pierret, "Correlation of Material Properties and Recombination Losses in $Al_{0.2}Ga_{0.8}As$ Solar Cells," submitted to *Solar Cells*, Lakewood, CO, May 24-26, 1989.